Characterisation of a Position Sensitive Thermal Neutron Detector

Laura Boyd
Physics and Astronomy MSci

Submitted in fulfilment of the requirements for the
Degree of Doctor of Philosophy

School of Physics and Astronomy
College of Science and Engineering
University of Glasgow

March 2021

Abstract

New types of position sensitive thermal neutron detectors for use in neutron imaging are in high demand due to the rising cost of ^{3}He used in most existing thermal neutron counters. A novel ^{6}Li doped scintillation glass sheet (GS20) coupled to a multi-anode photomultiplier tube with a portable data acquisition system, known as the Solid State Neutron Detector (SoNDe), is one possible solution. This study focuses on the characterisation and understanding of the Solid State Neutron Detector for application at the European Spallation Source (ESS), where the Small Angle Neutron Scattering instrument requires approximately 400 of these modular detectors. Therefore, understanding the efficiency, crosstalk, gain non-uniformities, and response to radiation of the SoNDe module is crucial.

Radiation from a number of sources were used to establish the main characteristics of the detector and the results compared. Sources included a 404 nm laser, ^{241}Am producing alpha particles, AmBe producing fast and moderated neutrons as well as gamma-rays, ^{60}Co and ^{137}Cs producing gamma-rays, and a pelletron accelerator producing protons. A simulation written using the Geant4 toolkit, verified through comparison to measured data, was used to study the details of the detector construction and to predict the response of the detector to possible sources of background radiation at ESS.

The gains and gain stability of the photomultiplier pixels are important for operation at ESS. The relative pixel gains of the photomultiplier tube were provided by Hamamatsu for each individual photomultiplier. However, given the importance of these numbers to determining detector response and setting readout thresholds, they were also measured using various methods. These methods included the use of a collimated alpha source and a laser spot centred on each pixel separately, a uniform square diffuse laser beam simultaneously illuminating all pixels, and a moderated neutron source illuminating all pixels. The alpha, neutron, and diffuse laser results are similar to the Hamamatsu measurement and give potential methods of detector calibration. The laser spot data shows a slightly different gain, and is less directly comparable to the production measurement.

The gain stability of the detector system and its drift characteristics were measured using the collimated laser and alpha-particle sources. The 404 nm laser was close in wavelength to the peak in the scintillation emission spectrum of the GS20 glass. Drifts of 10^{-4} %/hr were found. This indicated a minute shift in gain in the detector over an extended period of time (34 - 67

hours). The stability studies also highlighted the importance of a sufficient warm-up period, 1 hour in duration, prior to operation.

Various sources were scanned across the detector face to provide an in-depth look at the position dependence of the pulse-height response of the detector. Fine scans over the entire detector area were performed with a collimated laser beam at single and 60 photoelectron light intensity levels. The results revealed areas of higher/lower response (dead spaces) some of which is due to the presence of photomultiplier tube structures, such as focusing electrodes between the cathode and first dynode.

The crosstalk between pixels was measured using both the collimated alpha source and the laser. The percentage of signal in the neighbouring pixels surrounding the target pixel was measured. A range of 0.0 - 3.0 % was measured for the laser data, and 2.5 - 9.8 % for the alpha data. Both data sets were greater than the Hamamatsu results of 0.0 - 2.1 %. While the laser light was highly directional the scintillation light was emitted isotropically and gave rise to the increased crosstalk percentages in the surrounding pixels. The spreading of scintillation light from its point of origin was investigated in more detail with the Geant4 simulation.

Cross-pixel scans in the horizontal, vertical, and diagonal directions were carried out with collimated alpha particle and proton beam sources. The alpha beam spot on target was $\sim$ 1 mm diameter, while the proton beam spot was $\sim$ 0.1 mm diameter permitting finer scanning steps. The measured results revealed the variation in signal amplitude as the source was scanned across the detector face with the proton data presenting an especially stringent test for the predictions of the Geant4 based model of the detector.

The computer simulation was used to model the transport of optical photons through the detector and to predict the detector response to various types of ionising radiation. The transport of optical photons was used to study various combinations of detector configurations including a pixellated scintillation glass sheet, optical couplings, and reflective coatings. From the 73 detector variations studied, the optimum setup to minimise the spread of photons from their point of origin was found to be a non-pixellated scintillator devoid of optical coupling and reflective coating. Comparison of proton scan data with the simulation revealed the importance of non-perfect surface polish on the glass surfaces and also of electronic crosstalk, which is not considered in the main Geant4 code.

The Solid State Neutron Detector's ability to successfully detect thermal neutrons is highly important. A moderated AmBe source was used to irradiate the detector. A clear neutron peak was distinguished. A Geant4 simulation was used to compare with the measured data, and simulate possible neutron/gamma backgrounds with energies ranging from 0.025 eV - 100.0 MeV.

The Solid State Neutron Detector has been thoroughly characterised in stability, relative gain, and response to various forms of radiation. The detector optimisation revealed a number of possible alternative setups, with the originally proposed setup proving the most effective.

Contents

List of Tables

List of Figures

Acknowledgements

I would like to express my sincere gratitude to all my colleagues within the Nuclear and Hadron Physics Group for their support throughout the years. I would like to acknowledge my supervisors, Dr Bjoern Seitz, Dr John Annand, and Dr Rachel Montgomery for their key support during the course of my Ph.D, without them this would not have been possible. I would also like to extend thanks to Dr Ken Livingston, Dr Bryan McKinnon, and Prof. Bill Gelletly for all their advice and assistance. I am very grateful for the help and advice I have received from my fellow SoNDe colleagues based at Lund University/ESS, Dr Ramsey (Seian) Al Jebali, Dr Kevin Fissum, Dr Hanno Perrey, Dr Emil Rofors, Ms Vendula Maulerova, and Mr Nicholai Mauritzson. The knowledge I gained from my extended period at the Source Testing Facility was invaluable, and subsequent trips enriched my understanding of the project. A huge thank you for all the technical support I have received from Mr Tony Clarkson, Mr Paul Agnew, and Mr John Marshall. I would like to express my appreciation to the sales team at Hamamatsu, Mr Dan Springer and Mr Siefried Schmid for all the information they provided me on various products. Thanks to Prof. David Sanderson for his teaching throughout the years and facilitating the calibration measurements at the Scottish Universities Environmental Research Centre. To all my fellow students, especially Dr Peter Pauli and Dr Richard Gray, thank you for your friendship and advice. I am extremely indebted to my family and friends for their love and support during my studies, namely my mum Noreen, Emma, Jerry, Dan, and of course my dogs Poppie and Petrie.

Declaration

I hereby declare that this thesis and the work contained within it are my own unless otherwise stated. Work which received input from other group members/collaborators has been referenced and attributed appropriately throughout the thesis. All experimental work was carried out within the Nuclear and Hadron Physics Group at the University of Glasgow with the exception of the alpha source calibration, neutron and gamma radiation measurements, and proton beam studies. The ^{241}Am alpha particle source calibration of Section 4.2.1 was conducted at the Scottish Universities Environmental Research Centre (SUERC) under the supervision of Professor David Sanderson and Dr John Annand. The neutron and gamma radiation measurements of Sections 5.2.1 and 5.3 were facilitated by the Lund University Source-Testing Facility (STF) under Dr Kevin Fissum and Dr Hanno Perrey. The proton beam studies of Section 6.3 were measured at the Lund Ion Beam Analysis Facility (LIBAF) under the supervision of Professor Jan Pallon, Dr John Annand, and Dr Emil Rofors. This work has not previously been submitted for any other degree to any institution.

Laura Boyd
March 2021

Chapter 1

Introduction

The motivation for this work stems from the development of thermal neutron detection instruments for the European Spallation Source (ESS). Historically ^{3}He gas proportional counters have been the industry standard due to their high detection efficiency, exceeding 75% for low energy neutrons [1]. However, as a result of the rising cost of ^{3}He an increased number of novel detection techniques, tailored to particular applications, have been developed over the last few decades. Neutrons cannot be detected directly since they are not charged and therefore rely on secondary particle interactions for detection. At the ESS a number of novel detection techniques are used to image materials using neutron scattering.

The main focus of this research is centred on a Solid State Neutron Detector (SoNDe - German for 'probe') and its suitability for use in Small-Angle Neutron Scattering (SANS) imaging. The neutron flux (φ) at the sample position is estimated to be several 10^8 n/s/cm^2, thus the detector must be able to withstand high rates of incident neutrons. Alongside high rate capability the detector must have good position resolution, high detection efficiency, low sensitivity to background radiation/good noise immunity, good time resolution, durability, and reliability [2]. The following detector criteria were proposed for the SANS instrument SKADI (Small-K Advanced Diffractometer) and the SoNDe detector technology built around them

- Count-rate capability of ~ 20 MHz over a 1×1 m^2 detector area (720 Hz per active pixel)
- Pixel resolution of 6×6 mm^2
- Thermal neutron-detection efficiency > 80% with good gamma-discrimination
- μs time resolution
- ^{3}He independence
- Composed of individual modules that can operate independently [2].

These were the original idealistic goals for the detector. This thesis probes elements of the SoNDe detector and conducts a thorough characterisation study using various types of radiation,

supported by Geant4 [3] based simulations. This research, together with studies conducted by collaborators and other researchers, shows that such a detector can operate successfully.

1.1 European Spallation Source ESS

The ESS is a joint venture facilitated by the European Research Infrastructure Consortium (ERIC) which strives to increase 'knowledge mobility' and further relevant scientific and technological research in Europe [4]. The ESS will host the world's most powerful spallation neutron source powered by a proton linear accelerator (linac) [5]. The protons generated by an ion source are directed through a Low Energy Beam Transport (LEBT) line towards the Radio Frequency Quadrupole (RFQ) where they are collected and accelerated up to 3.6 MeV. The beam characteristics are diagnosed in the Medium Energy Beam Transport (MEBT), and then optimised for acceleration in the Drift Tube Linac (DTL). Once the protons have gained enough speed they will be further accelerated by a voltage gradient of $\sim$ 9 MV/m in the superconducting Niobium cavities. The cooled cavities ($\sim$ 2 K) supply a power of 400 kW to the proton beam, and a powerful radio frequency (RF) electromagnetic wave (352.21 MHz) propels the protons through the cavities at increasing speeds. This will be the first linac to employ the use of spoke cavity technology to accelerate protons and the most powerful by a factor of five [6].These cavities are followed by Medium and High Beta Linac cavities [7] operating at 704.42 MHz, which accelerate the protons to an energy of 2 GeV. A schematic of the beam line assembly is shown in Fig. 1.1.

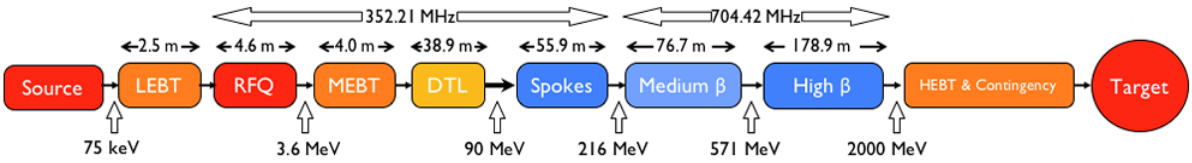

Figure 1.1: Flow chart representation of the proton linear accelerator beam line stages at the ESS. Image taken from [7].

The final proton beam has an energy of 2 GeV with a pulse length of 2.86 ms, a repetition rate of 14 Hz and a current of 62.5 mA [8]. It is directed towards a rotating monolith. The monolith encases a target wheel which is constructed of $\sim$ 4.9 tonnes of tungsten (chosen for its 'heavy' neutron rich nucleus). The high energy proton beam strikes the tungsten target and induces spallation reactions that split the nuclei into smaller (highly excited) nuclear fragments, neutrons (highest abundance), protons, pions, positrons (due to increased proton numbers in the nucleus), and gamma-rays. Energetic neutrons and other secondary particles induce further spallation events, so that approximately 25 neutrons of average energy 29 MeV are produced per 1 GeV incident proton energy on a tungsten target. By comparison a fission event at a

reactor produces $\sim$ 2.5 neutrons, of which $\sim$ 1.5 are moderated to the appropriate energy range to maintain the chain reaction [9] [10].

The fast spallation neutrons are slowed down using parahydrogen and water moderator-reflector assemblies (Fig. 1.2a) to produce spectra of cold (0.0 - 0.025 eV) or thermal neutrons (0.025 eV) respectively. Each instrument may select the energy of their neutron spectrum by guiding the beam through the appropriate moderator and monochromator crystal. A bi-spectral beam of cold and thermal neutrons may be achieved using a supermirror which reflects cold neutrons into the elliptical guide and transmits thermal neutrons into the same guide [11]. The layout of the instrument suite can be seen in (Fig. 1.2b).

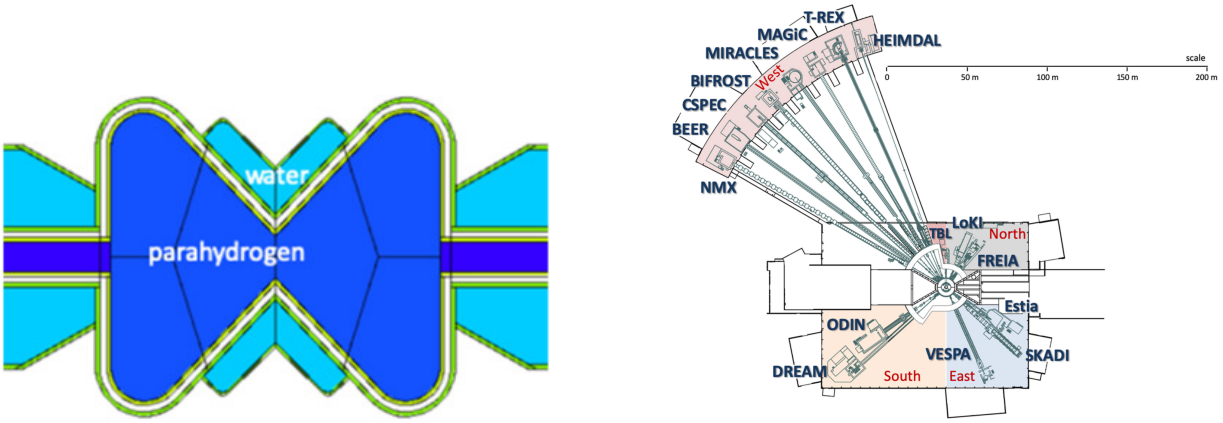

(a) (b)

Figure 1.2: (a) The butterfly moderator design with parahydrogen (dark blue $\sim$ 24 cm wide) and water (light blue) components. Each beam port is directed to its nearest water-hydrogen junction. Cold or thermal neutrons can be obtained by directing the guide system of the beam port to adjacent hydrogen or water sections respectively. (b) The proposed instrument layout at the ESS is divided across four experimental halls. The proton beam is incident from the right in both figures. Both images taken from [12].

When constructing a spallation neutron source there are a number of possible target choices. Spallation reactions can occur in all elements if a high-energy particle beam is incident. The number of neutrons released per particle interaction is proportional to the atomic number of the element, making heavier elements more suitable/efficient targets. There are a number of characteristics one must consider when choosing a target: good thermal conductivity (at operation temperature), low thermal expansion coefficient (to minimise thermal and fatigue stress), high melting point, resistance to corrosion (both under irradiation and not), low radio-toxicity, chemical stability, manufacturability, ductility, joinability etc. [13].

Tungsten is an attractive material for this purpose since it shows good resistance to radiation damage and low levels of corrosion (gas coolant). It is chemically inert, widely available and well priced, therefore it is valued as one of the best spallation neutron targets. Tungsten however is extremely hard and therefore difficult to machine. It also corrodes in the presence of water when irradiated, and as a result must be clad in high corrosion resistant materials such as

Tantalum [14].

Tantalum may also be used as a spallation target as it is more readily machined than tungsten, has a very high melting point, and a good neutron yield. Tantalum is significantly more expensive than tungsten however, has a lower neutron yield, and has a relatively high neutron absorption cross-section leading to high levels of radioactivity and afterheat in used targets [10].

Heavier (fissile) materials such as Uranium may appear more attractive as a spallation target due to their large neutron yield. However, they possess major problems such as swelling, short service lives, chemical activity, combustibility, corrosion, and delayed neutron production (contributing to an independent neutron background). Actinides cannot be used with higher powered particle beams as the material depletes too rapidly and may combust.

1.1.1 Science at ESS

Research at the ESS will initially be carried out with 15 new instruments. These instruments aim to serve research in life sciences, magnetism studies, material sciences, and other disciplines. The instruments range from:

- Backscattering spectrometers (e.g MIRACLES) which will be used to study molecular dynamics at time scales of ps to ns for degenerative diseases, organic electronic devices, and fuel cells.

- Engineering diffractometers (e.g. BEER) which will be used to further understand the fabrication, optimisation, and degradation of modern engineering materials [12]

- Liquid reflectometers (e.g. FREIA) which will uncover the nuclear and magnetic structure of thin films (with resolution of a few Å [12]), for applications to the study of soft condensed matter and life sciences.

- Small angle neutron scattering instruments (LoKI + SKADI) which will probe the nanometre to micrometre nuclear and magnetic structure of polymers and geological materials etc.

Imaging objects with neutrons reveals properties of materials that are insensitive to electromagnetic probes (e.g. X-rays). X-ray beams interact via Compton Scattering, Photoelectric absorption, and, if sufficiently energetic, pair production. X-rays interact preferentially with high-Z materials such as lead. Neutrons interact differently with matter since they are strongly interacting uncharged particles [15]. Neutrons may be scattered off hydrogen rich materials such as plastic, or captured by elements such as ^{6}Li and ^{10}B which have high capture cross-sections. A comparison of neutron and X-ray imaging of an object is shown in Fig. 1.3. As neutrons do not ionise a medium as they move through they are able to penetrate deeply within most materials (Fig. 1.4). This is an advantage in the internal imaging of objects with intricate shapes. Neutrons may be scattered or absorbed by nuclei, however the extent of this varies across the

Figure 1.3: Dual image of an analogue camera imaged using neutrons (top) and X-rays (bottom). The X-rays interact mainly with the heavier, high-Z materials of the camera, whereas the neutrons interact mainly with the light, hydrogen-rich materials such as the plastic film. Image taken from [17].

periodic table and isotope families. The wavelength of thermal neutrons is similar to the interatomic distances between the nuclei of atoms in a material, making refraction or diffraction techniques useful for constructing images. Neutrons have a magnetic moment and are therefore sensitive to magnetic fields. Magnetic imaging can be achieved using a collimated polarised monochromatic neutron beam. The magnetic field will cause the neutron spin orientation to precess, but will not affect the direction of the beam. During the scattering process, the presence of a magnetic field will modify the azimuthal scattering distribution. Polarised neutrons can also image magnetic structures as the magnetic scattering cross-section is similar to the nuclear cross-section for a number of atoms [16]. This technique can determine vector magnetisation in materials.

1.1.2 Neutron Scattering

Neutron scattering may alter both the energy and momentum of the particle and matter from which it scatters. At absolute zero where the nucleus is fixed/stationary the scattering will be elastic. However, atoms in matter are able to move (to an extent), therefore scattering events are more likely to be inelastic however elastic scattering can still occur. The energy that is lost by the scattered neutron in an inelastic collision is transferred to the scattered sample. The number of neutrons scattered within a sample is measured as a function of the change in wave vector ($\mathbf{q}$) and the change in energy (E).

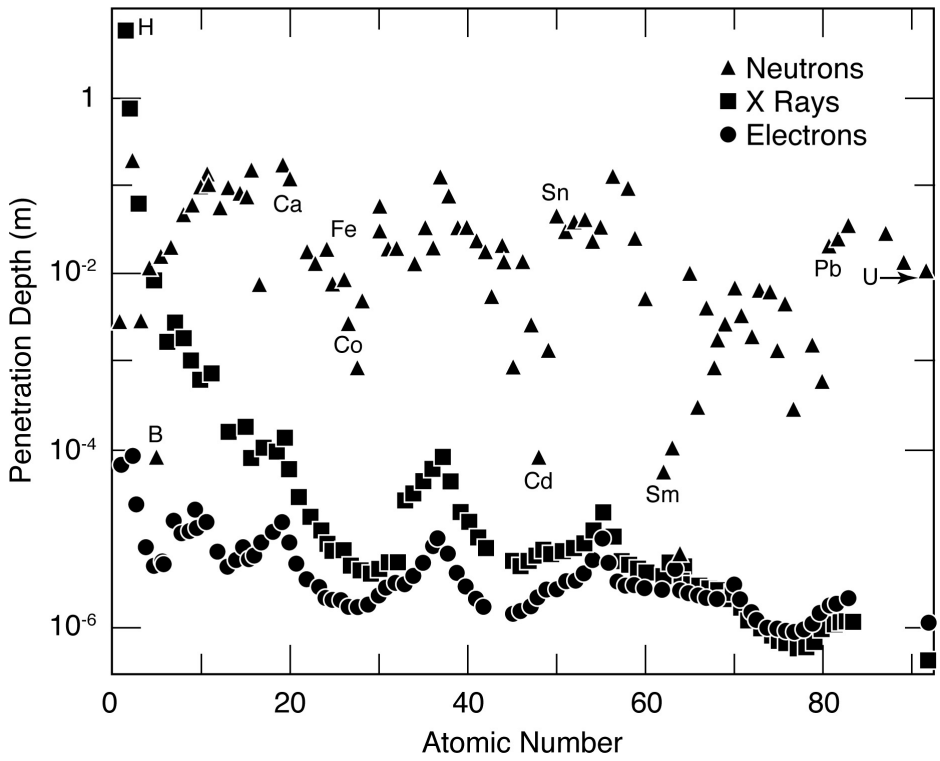

Figure 1.4: The penetration depths of low energy electrons, thermal neutrons (λ = 0.14 nm), and 8 keV X-rays for elements of increasing atomic number in solid or liquid form. Image taken from [15].

The magnitude of the neutron wave vector **k** is defined as

$$|\mathbf{k}| = \frac{2\pi mv}{h} = \frac{2\pi}{\lambda}, \tag{1.1}$$

where m is the mass of the neutron, v is the velocity, h is Planck's constant, and λ is the wavelength. The corresponding momentum transfer from the neutron to the scattering object is given by

$$\frac{h\mathbf{q}}{2\pi} = \frac{h(\mathbf{k}-\mathbf{k}')}{2\pi}, \tag{1.2}$$

where $\mathbf{q} = \mathbf{k} - \mathbf{k}'$ is the scattering vector and $\mathbf{k}'$ the wave vector for the scattered neutrons. The magnitudes of the incident and scattered wave vectors are equivalent for elastic scattering, $|\mathbf{k}| = |\mathbf{k}'|$, the scattering vector **q** is then given as

$$\mathbf{q} = \frac{4\pi sin\theta}{\lambda}, \tag{1.3}$$

where θ represents the scattering angle. This process can be represented as a scattering triangle (Fig. 1.5).

Scattering can be elastic and inelastic and it can also be both coherent (same frequency, wave form, and constant phase difference) and incoherent (out of phase etc.). The type of scattered

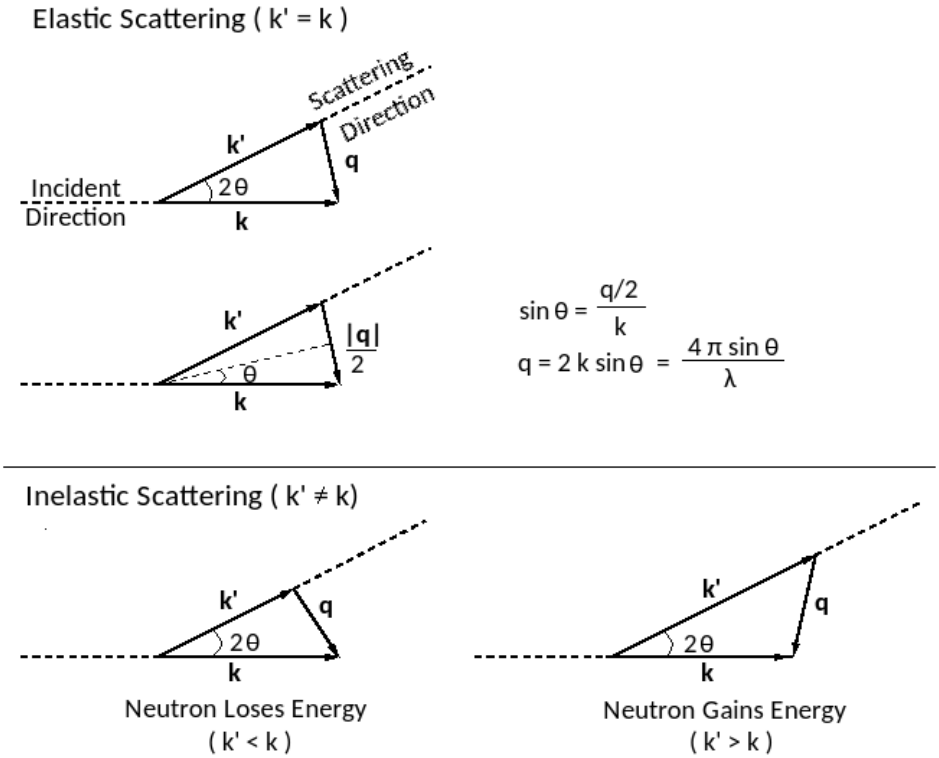

Figure 1.5: A representation of an elastic scattering interaction (top) during which the neutron loses no energy ($\mathbf{k}' = \mathbf{k}$), and an inelastic scattering depiction (bottom) in which the neutron loses energy ($\mathbf{k}' < \mathbf{k}$) or gains energy ($\mathbf{k}' > \mathbf{k}$). The neutron is scattered through an angle of 2θ and it's relationship to $\mathbf{q}$ shown in Eq. 1.3 for elastic scattering. Image derived from [15].

neutron waves detected can reveal properties of a solid material, as shown in Table 1.1.

Table 1.1: Neutron scattering types and properties uncovered in materials.

	Coherent	Incoherent
Elastic	Structural information e.g equilibrium structure	Unwanted background
Inelastic	Motions of atoms, phonons & vibrational waves	Single atom dynamics

In practice these are used for a number of applications. Neutron spectroscopy (inelastic scattering) can be used to probe the rotational modes of molecules, recoil in quantum fields, and electronic transitions. Neutron diffraction (elastic or Bragg scattering) requires the crystals within a structure to be orientated such that $\mathbf{q}$ is perpendicular to the scattering planes. It can be used to determine the atomic and/or magnetic structure of a material, the spacing between crystalline planes, and the density of atoms in those planes. This holds true for a simple crystal composed of one type of atom. For crystals made of multiple types of atoms, misaligned crystals becomes an issue. To overcome the phase problem one can use a polycrystalline powder in a technique known as neutron powder diffraction. Neutron reflectometry requires a beam of neutrons to strike the surface of an object at a shallow angle. A portion of these neutrons will be reflected at the surface (or interfaces between surfaces), or transmitted. The detected neutrons

can be used to find the thickness of layers close to the surface of a material, as well as their sequence (structure), and scattering length densities [15].

To probe larger structures (larger than interatomic distances) such as colloids, polymers, and viruses, the momentum transfer **q** must be small. To achieve this consider the relationship in Eq. 1.3. One can either increase the neutron wavelength, λ, or decrease the scattering angle θ. It is not yet possible to create large fluxes of very-long wavelength neutrons, therefore small scattering angles are required to achieve the desired results. The technique is known as small-angle neutron scattering, or SANS.

1.2 SANS Instruments and SKADI

A SANS instrument uses a monochromatic source of neutrons in the form of a pulsed or continuous beam to scatter from a sample, determining the neutron intensity as a function of scattering angle. The neutrons for such an experiment can be produced by reactors or spallation sources. The neutron flux of continuous beam sources tend to be limited to $\sim 10^{15}$ n/s/cm^2. A comparison of thermal neutron flux for continuous and pulsed beams is shown in Fig. 1.6.

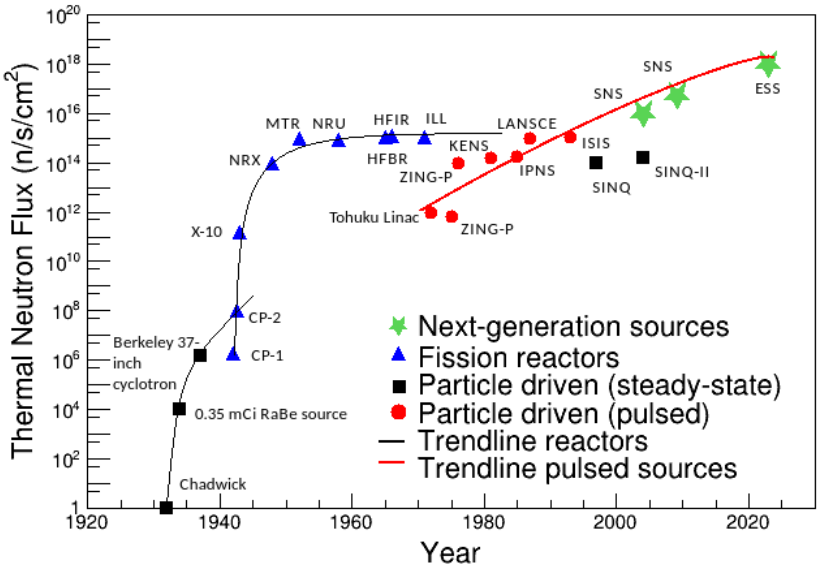

Figure 1.6: Historic progression of thermal neutron flux achievable from reactor and spallation sources. The top right shows the high flux achievable from next generation pulsed spallation sources including ESS, produced from high energy (GeV) proton beams. Image adapted from [18] [19].

One of the main design considerations of a SANS diffractometer is the sample size, it must be kept large ($\sim$ 1 cm) in order to obtain reasonable scattered neutron intensities. Traditionally SANS instruments use either a velocity selector, polycrystalline BeO filter, double-crystal monochromator, or misaligned crystals as a monochromator [20]. The benefits of each method

are discussed in detail in Aswal *et al.* [21]. SANS instruments use longer wavelength neutrons ($\lambda \geq 4$ Å) to achieve low **q** (wave vector transfer) values. The relation of the uncertainty in **q** to scattering angle (θ) and incident wavelength (λ) uncertainties is given by

$$\frac{\Delta \mathbf{q}}{\mathbf{q}} = \left[\left(\frac{\Delta \theta}{\theta} \right)^2 + \left(\frac{\Delta \lambda}{\lambda} \right)^2 \right]^{1/2}. \tag{1.4}$$

The uncertainty $\Delta\theta$ is dependent on the size of the beam entrance and exit slits [20]. The wavelength resolution $\frac{\Delta\lambda}{\lambda}$ is dependent on the length of the instrument, the pulse length at the source, and the time required for a chopper to close/open when traversing the full cross-section of the neutron guide [22].

SKADI, Small-K (momentum) Advanced DIffractometer, is a SANS instrument currently in construction at the ESS. It is designed for applications including biological and medical research, and will be capable of investigating magnetic and nanomaterials such as carbon nanotubes and fullerenes. SKADI will also have the ability to measure the polarisation of the scattered neutrons to probe the spin state of the atoms within the sample (important for magnetic material investigation) [23].

The aim of the ESS is to build a versatile SANS instrument capable of achieving a dynamic $|\mathbf{q}|$ range (10^{-4} Å$^{-1} < |\mathbf{q}| < 1$ Å^{-1}) and very high **q** resolution [24]. The spallation source will provide a pulsed beam of neutrons with 2.86 ms pulse duration, a wavelength range of 3 - 21 Å [12], and a repetition rate of 14 Hz [25], which will enable time-of-flight analysis for the detected neutrons. To maintain high scattering intensities the sample size will remain large (1×1 cm^2), in line with the traditional method as mentioned previously.

The neutron beam energy and bandwidth can be modified using the choppers, polariser and blinds shown in Fig. 1.7. These are used to restrict the neutrons transferred to only those useful in the experiment. The instrument will have the ability to vary the wavelength band (suppress higher order wavelengths, increase wavelength resolution) of the incoming neutrons by using a set of three choppers. The bandwidth choppers are made of two co-rotating discs capable of supplying a range of opening times, required for wide wavelength band modes [24]. Detailed information on the chopper configuration can be found in Ref. [22]. The area which will house the scattering sample under investigation will have an adjustable temperature, pressure, and gas environment to fulfill the users needs.

The task of the detector (housed in the tube at the end of the instrument) will be to measure the trajectory of scattered neutrons. The position resolution is one of the main aims when selecting an appropriate detector for the instrument. The high flux of scattered neutrons dictates that the detector be radiation hard, and have a relatively short dead time. A number of neutron detection techniques are discussed below and their applicability to SKADI assessed.

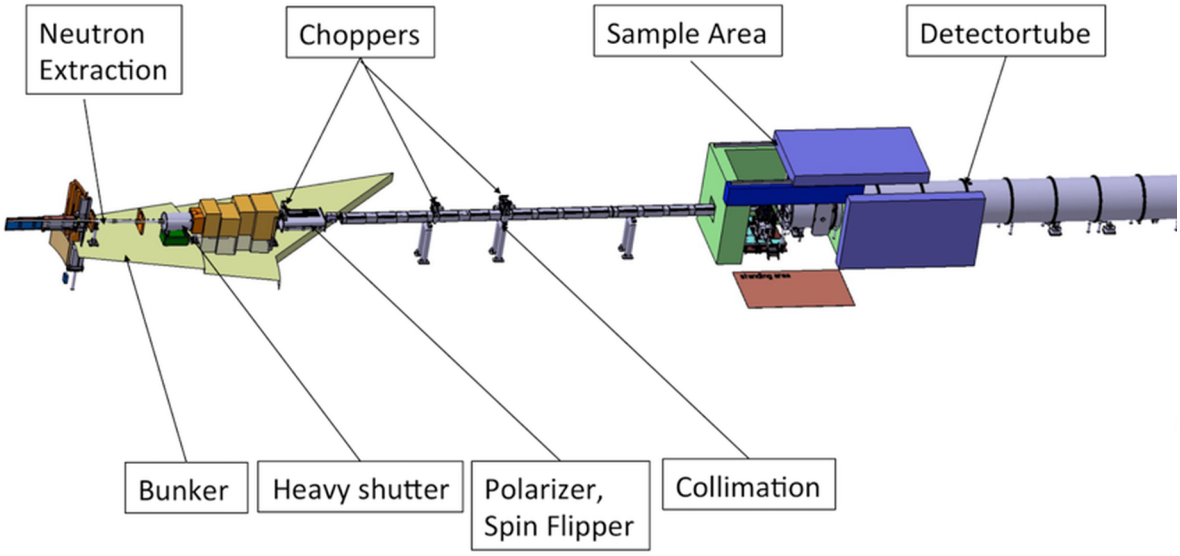

Figure 1.7: A schematic outline of the SKADI instrument measuring $\sim$ 55 m in length from neutron extraction to detection. The neutron beam travels from left to right. The neutrons are extracted from the source line and are transported through the bunker (radiation shielding). They are then passed through the choppers and collimation system in which the resolution of the experiment is designated, the polarisation of the incoming neutrons may also be selected. The sample area is customisable to accommodate the users needs, and the detectors are housed in the tube at the end of the instrument. Image taken from [26].

1.3 Neutron Detection Techniques

Experiments involving neutrons require detectors that are able to operate with great stability in harsh conditions, e.g. high fields of radiation, and various temperature environments. They must maintain a high level of efficiency whilst discriminating neutrons from background radiation. A number of detection techniques exist in neutron scattering research, all of which rely on secondary particle detection.

1.3.1 Helium-3 Tubes

^{3}He gas filled proportional counters (Fig. 1.8) are among the most common neutron detectors. The detector consists of a gas filled tube with a high voltage applied between the axial anode wire and the outer cylindrical cathode. When neutrons irradiate the tube they interact with the ^{3}He atoms (which have a cross-section σ = 5330 b at a neutron energy of 0.025 eV, where 1 barn = 10^{-24}cm^2) to produce ^{3}H (tritium) and a proton in the reaction

$$^3_2\mathrm{He} + ^1_0\mathrm{n} \rightarrow ^1_1\mathrm{H} + ^3_1\mathrm{H} + 764\mathrm{keV}. \tag{1.5}$$

The proton and triton ionise the surrounding gas. Electrons and ions are accelerated by the electric field causing further ionisation. The mean number of electron-ion pairs created is

Figure 1.8: A customisable ^{3}He filled proportional counter produced by GE Reuter Stokes. This model can withstand pressures up to 30 atmospheres. Image taken from [27].

directly proportional to the energy deposited in the counter [28]. The electrons are accelerated towards the anode and the ions towards the cathode creating a pulse of current at the anode. This sensing device is capable of detection efficiencies of above 70% for a ^{3}He pressure of 4-atm or greater [29]. The helium proportional counter is ideal as it has such a high sensitivity to neutrons and insensitivity to gamma radiation, however it cannot be used in high intensity neutron fields as its 'dead-time' is of the order of several microseconds [30], rendering it inefficient for the SKADI instrument. Dead-time is the finite period of time required by a detector to process an event in which it may be insensitive to further incoming radiation, or if sensitive, cause a pile-up of events resulting in a distorted signal. The availability of ^{3}He is decreasing (a large percentage of it is held by the US military) and its production is dependent on the decay of ^{3}H which has a half life of 12.3 years [31].

1.3.2 Multi-Blade and Multi-Grid Boron-10 Based Detectors

Novel detection methods that employ ^{10}B coated proportional counters are to be used at the ESS for thermal and cold neutron detection. Multi-Blade and Multi-Grid are such detectors. Multi-Blade (Fig. 1.9) will be used as the detection device for thermal neutron reflectometer instruments such as ESTIA [32] and FREIA [12]. Reflectometer instruments require good spatial resolution and high counting rate capability. The Multi-Blade detector, is currently comprised of an array of nine multi-wire proportional chambers (MWPC), filled with Ar (80%) and CO_2 (20%). Each individual chamber is identical and is known as a 'cassette'. It measures 11×130 mm^2 and contains an Al 'blade' coated with $^{10}B_4C$ to convert incident neutrons, and a read-out system comprised of 32 strips and 32 wires layered in planes offset from parallel by 0.14^o [33]. The wire pitch and strip width are both 4 mm and the blade is inclined at 5^o with respect to the particle beam. The cassettes are placed in a circle around the sample and slightly overlapped to avoid dead areas. The spatial resolution across the wire and strips is ~ 0.5 mm and 3.5 mm respectively [34].

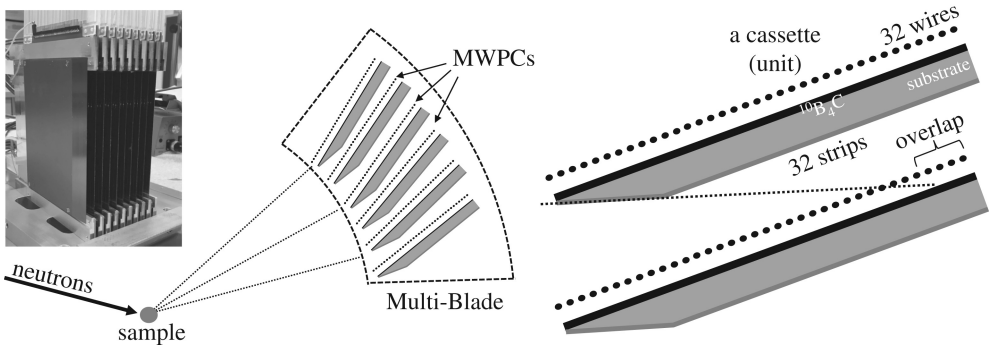

Figure 1.9: A Multi-Blade detector cassette (left) with cross-sections (middle and right) of the MWPCs. Image taken from [33].

The Multi-Grid detector (Fig. 1.10), will be used for several time-of-flight neutron spectrometer instruments, CSPEC [35], T-REX [36], and eventually VOR [37]. The detector is an array of MWPC modules filled with Ar (80%) and CO_2 (20%). The modules are divided by $^{10}B_4C$ coated Al sheets. The grids are separately insulated and act as the cathode of the detector. A wire through each grid acts as the anode, creating a MWPC element with segmented cathodes. The position of the incoming neutron is determined by a coincidence between wire and grid signals. The event can be localised to an area of $22 \times 22 \times 11$ mm^3 [38]. The layering of $^{10}B_4C$ is increased from 1 μm to 2 μm as the neutrons traverse through the detector from front to back to improve the detection efficiency and uniformity of the detector's response. Neutron spectrometers require very low background counting rates. To achieve this, high purity Al was used for the coated blades to minimise alpha-emitting impurities.

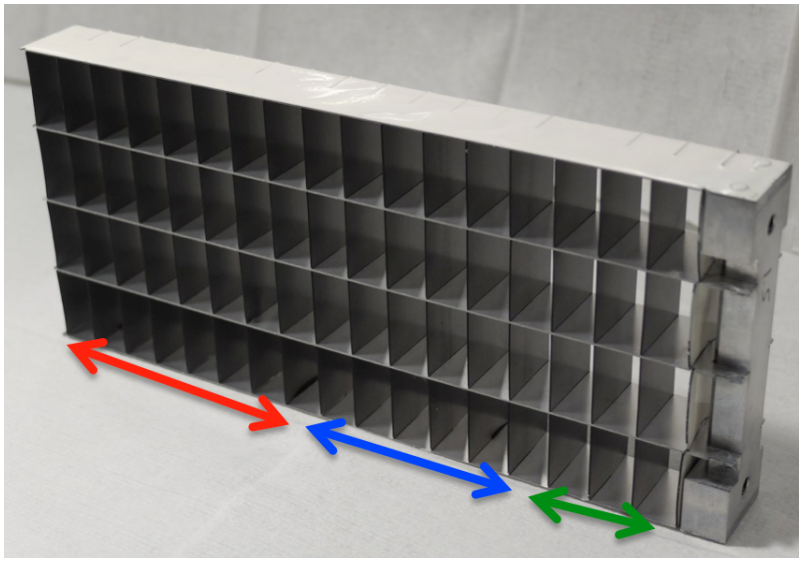

Figure 1.10: A view of the grid setup with regions of boron layer thicknesses increasing from left to right. Image taken from [38].

Although both types of detector can handle high rates of neutron flux, the resolution of the Multi-Grid detector is not precise enough for the SKADI SANS application, which requires a

pixel resolution of 6×6 mm^2. These detectors were originally designed for reflectometer and spectrometer instruments.

1.3.3 Microstructured Semiconductor Neutron Detectors

The need for a replacement for ^{3}He detectors prompted a surge in the development of highly efficient and low cost microstructured semiconductor neutron detectors (MSNDs). Traditionally thin film or 'foil' type thermal neutron detectors have been used when the film containing ^{10}B or ^{6}Li is deposited on a planar diode [39]. In these detectors, the following reactions are used to detect neutrons,

$$^{10}\mathrm{B} + \mathrm{n} \rightarrow \begin{cases} ^7\mathrm{Li}^* \text{ (at 1.015 MeV) + } ^4\mathrm{He} \text{ (at 1.777 MeV),} \\ \text{Reaction Q-Value = 2.792 MeV (to ground state),} \\ ^7\mathrm{Li}^* \text{ (at 0.840 MeV) + } ^4\mathrm{He} \text{ (at 1.470 MeV),} \\ \text{Reaction Q-Value = 2.310 MeV (1st excited state) [39].} \end{cases} \tag{1.6}$$

$$\begin{gathered} ^6\mathrm{Li} + \mathrm{n} \rightarrow ^3\mathrm{H} \text{ (at 2.73 MeV) + } ^4\mathrm{He} \text{ (at 2.05 MeV)} \\ \text{Reaction Q-Value = 4.78 MeV [39].} \end{gathered} \tag{1.7}$$

^{10}B and ^{6}Li capture cross-sections (σ) decrease with increasing neutron energies. Both have a 1/v dependence (where v is velocity) for energies approximately < 1 MeV, so that thermal neutrons are more readily absorbed than fast neutrons [40] [41] [42]. The variation of neutron capture cross-section for ^{10}B, ^{3}He and ^{6}Li with increasing energy is shown in Fig. 1.11. An

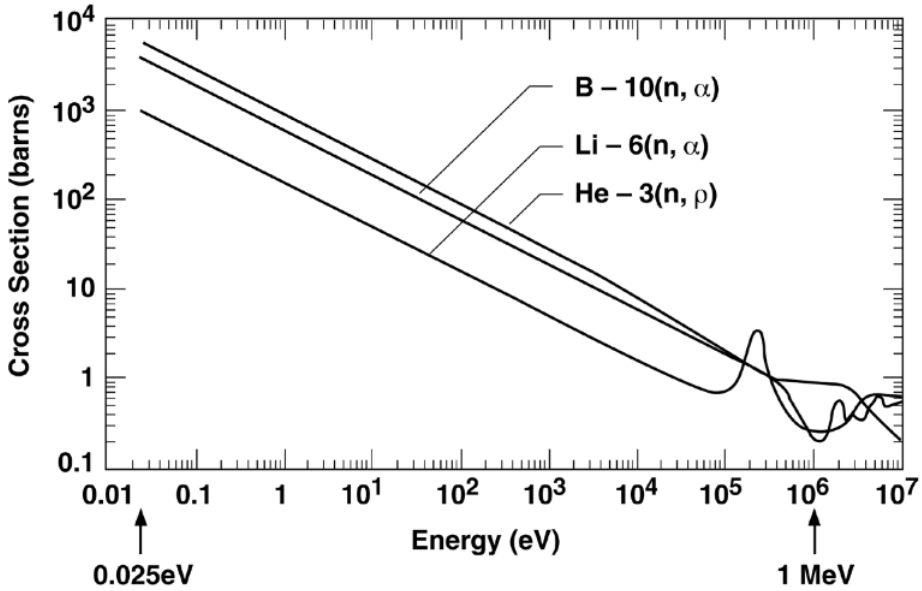

Figure 1.11: Neutron capture cross-sections for ^{6}Li, ^{10}B, and ^{3}He in barns for increasing energy (eV). Image taken from [41].

intrinsic problem with the foil is self-absorption (where the charged ion stops in the neutron

absorbing foil before it reaches the diode) which is a limiting factor in the neutron detection efficiency. Alternative reactions that have been used in solid-form films for neutron detection include ^{157}Gd(n,γ)^{158}Gd and ^{113}Cd(n,γ)^{114}Cd. Gadolinium is a desirable material as it has a very large thermal neutron (0.025 eV) cross-section, $\sim$ 240,000 b [43], however the low energy emitted gamma radiation is hard to distinguish from background gamma radiation, and this also applies to cadmium [39],

MSNDs were developed in order to increase the relatively low efficiency of planar thin-film-coated devices from $<$ 4 - 5% to 35% detection efficiency (the theoretical maximum) for 0.5mm thick devices backfilled with ^{6}LiF [44] [45] [46]. Like thin film coated neutron detectors, they are easily mass produced, compact, and operate at a low voltage. MSNDs are built by etching perforations into a semiconductor material, coating a p-n junction layer into these micro-sized trenches and finally backfilling the perforations with a neutron reactive material [46] e.g. ^{6}LiF, as shown in Fig. 1.12.

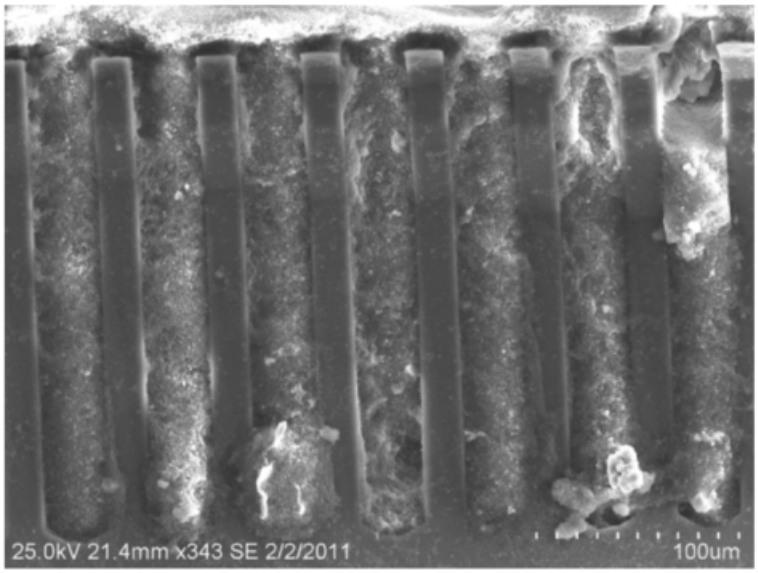

Figure 1.12: Side view of an MSND backfilled with ^{6}LiF nanopowder. The wet-etched straight trench micro-structures are 224 microns deep. Image taken from [46] © 2011 IEEE.

Perforation increases the effective thickness of converter material presented to incident neutrons while maintaining a short distance between the neutron absorption point and the active Si [47]. By stacking two MSNDs and properly aligning them, it is possible to obtain a neutron detection efficiency of 42% [46]. MSNDS have been proposed for use at SNS-ORNL (spallation neutron source, Oak Ridge National Laboratory). The 3000 pixel array will have extremely fine spatial resolution resolution (100 micron), $\sim$ 30% intrinsic thermal neutron efficiency, and $<$ 10 microseconds dead-time [48].

Dual-Sided Microstructured Semiconductor Neutron Detectors

Whilst current market MSNDs are approaching theoretical detection limits, a fraction of neutrons continue to pass through the device undetected. Dual-sided microstructured semiconductor neutron detectors (DSMSND) have been developed with similar trenches on both the front and back side of the device, hence sensing these previously undetected neutrons. These semiconductor devices are theoretically capable of $> 80\%$ intrinsic thermal neutron detection efficiency for a 1mm thick device backfilled with ^{6}LiF [49] The large detection efficiency of these devices makes them the potential front runner for future neutron detection devices.

There exist two basic types of DSMSNDs, a vertically-operated, high-efficiency opposing-pattern design (Fig. 1.13a) with complementary front and rear designs, and an interdigitated version (Fig. 1.13b) of conformally-doped junctions.

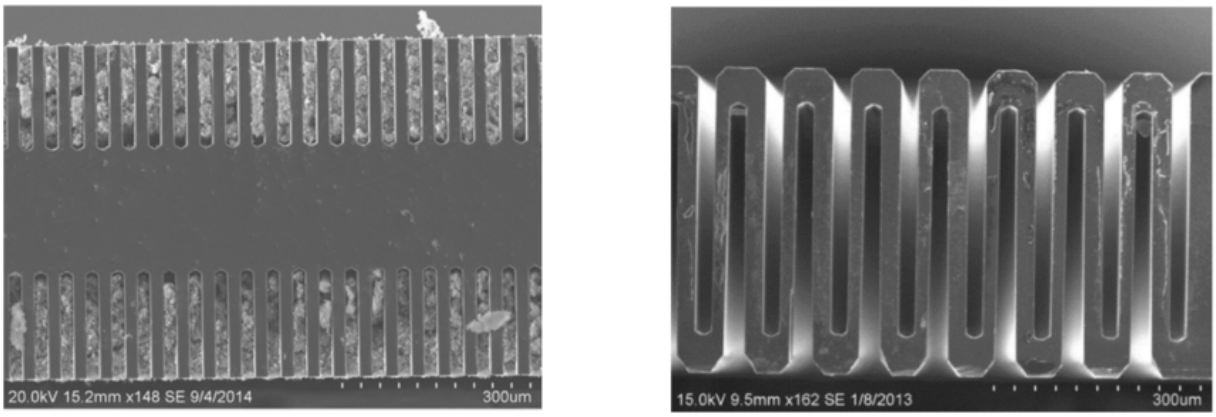

(a) (b)

Figure 1.13: Two possible iterations of a dual sided microstructured semiconductor neutron detector. The complimentary backfilled 'trenches' in (a) work to give ultra-high efficiency in sensing neutrons. The interlacing trenches of (b) create an ultra-low dead-time neutron sensor. Image taken from [49].

The detection efficiency of the DSMSNDs would fulfill the requirements for the SANS instrument and the position resolution ($\sim \mu$m) of the technology is far superior to the requirements of SKADI (6×6 mm^2).

1.3.4 Scintillators

Scintillators are phosphorescent materials that, when struck by ionising radiation, produce visible-ultraviolet photons. This characteristic is known as photoluminescence. A scintillation detector generally consists of a piece of scintillation material, a photon sensor, and optional components to transport the light between scintillator and sensor. A number of photo-sensitive materials exist and will be discussed later. The light sensor converts the scintillation photons into electronic signals which carry crucial information including:

- Sensitivity to energy. Many scintillators display a light output relationship almost linear to the energy deposited, and since a photomultiplier tube (PMT) also has linear behaviour the final electronic signal output will be proportional to the initial energy input, thus making a scintillator a suitable energy spectrometer.

- Time response. The response and recovery time for some scintillators can be fast in comparison to other detectors. This enables the time of detection to be determined precisely and allows for high counting rates as the dead time (time lost whilst waiting for the scintillator to recover/relax) is small [28].

- Pulse shape discrimination (PSD), wherein one has the ability to distinguish between two different types of radiation (e.g. alpha and gamma) by analysing their pulse shape. For some materials the scintillation decay time depends on the dE/dx of the incident particle.

Scintillators can be in solid, liquid, and gas form, and may be further subdivided into organic/inorganic. The detection of thermal neutrons uses neutron capture reactions where the compound nucleus subsequently splits to produce energetic charged ions. Elements such as ^{6}Li and ^{10}B have high neutron capture cross-sections.

Organic Scintillators

Organic scintillators can be subdivided into plastic scintillators, organic crystals, and liquid scintillators. All are aromatic hydrocarbon compounds that contain benzene-ring structures. These materials scintillate due to the transitions of delocalised electrons occupying the 'π' orbital within the molecule.

Solid plastic scintillators are the most widely used of the organic scintillators and are similar in composition to liquids. Some common inert plastic bases to which active benzene-related molecules are added include polyvinyl toluene PVT (highly transparent), polyphenylbenzene and polystyrene (fast neutron detection). Plastic scintillators are desirable as they are easily machined and can be cast in many shapes. PVT-based plastic scintillators have a density $\rho \sim 1.03\text{g/cm}^3$ and a refractive index of 1.58 [50]. Plastic scintillators have a high light output and a decay constant of about 2 - 3 ns [28]. For thermal neutron detection plastic scintillators may be loaded with nuclides with high capture cross-sections such as, ^{6}Li, ^{10}B, and ^{157}Gd. However, upon neutron capture ^{157}Gd produces gamma-rays across a range of energies rendering it useless for PSD in thermal neutron SANS detection. Plastic scintillators with pulse shape discrimination capabilities based on ^{6}Li-Salicylate have been synthesized by bulk polymerisation [51].

Organic crystals are desirable for their rapid decay time ($\sim$ ns) [52], good neutron/gamma separation due to slow and fast decaying components (ideal for PSD), and high light output. However, large crystals are very difficult to grow and are expensive, not ideal for the hundreds of individual modules proposed for SKADI. The most common types of organic crystals include anthracene $C_{14}H_{10}$ (used as the standard comparison for light yield, 17,400 photons/MeV) [53],

stilbene $C_{14}H_{12}$ and naphthalene $C_{10}H_8$. The presence of hydrogen in these scintillators makes them ideal for fast neutron detection (elastic scattering off the hydrogen atoms generates ionising recoil protons), but not for thermal neutron detection. ^{6}Li-Salicylate (LiSal, $LiC_6H_5O_3$) crystals are sensitive to thermal neutrons, have a light yield of approximately 8000 photons/MeV (when measured with both beta and gamma sources) [54], and good neutron/gamma pulse shape discrimination (Fig. 1.14). However, organic crystals can be fragile to mechanical or thermal shock.

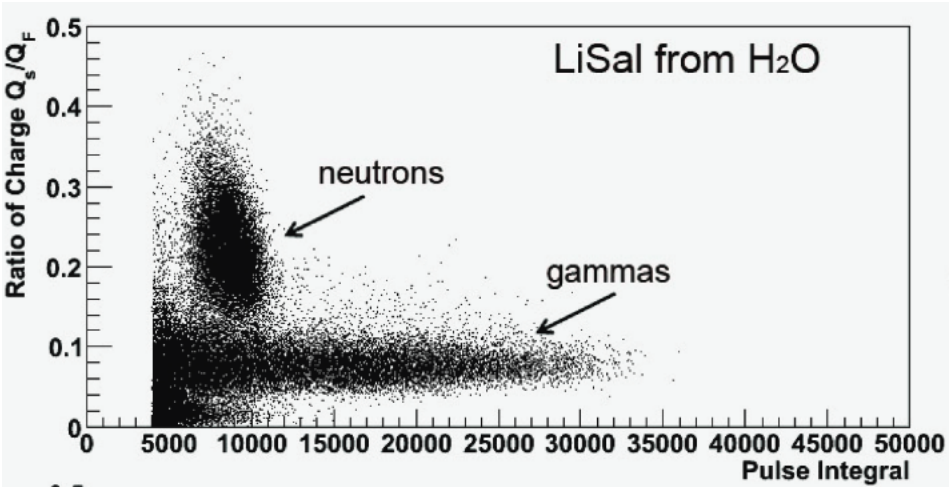

Figure 1.14: The thermal neutron/gamma pulse shape discrimination capabilities of a LiSal single crystal. Image taken from [54].

Liquid solutions are commonly used as organic scintillators. Unlike crystalline/solid materials the energy absorption mechanism is different. In theory the ionisation energy is absorbed mainly by the solvent (e.g xylene, toluene, and benzene) and then passed on to the scintillation solute, however this is still not yet fully understood [28]. Common organic scintillators used in solute form for fast neutron detection include p-Terphenyl $C_{18}H_{14}$, PPO $C_{15}H_{11}NO$, and the wavelength shifter POPOP $C_{24}H_{16}N_2O_2$. Examples of liquid scintillators for fast neutron applications (originally developed by Nuclear Enterprises and now marketed/produced by Saint Gobain) are shown below in Table 1.2 [55]. One of the most notable scintillators is NE213A, known

Table 1.2: A comparison of liquid scintillators available from Saint Gobain. Information provided by [55].

Scintillator	Distinguishing Features	Principal Applications
BC-501A	excellent pulse shape discrimination	γ >100 kev, fast n spectrometry
BC-519	pulse shape discrimination properties	γ, fast n; n-γ discrimination
BC-525	Gd loaded; mineral oil base	n spectrometry in large acrylic tanks

also as BC-501A (BICRON) which has excellent pulse shape discrimination properties [56].

Liquid scintillators can be doped with neutron-capture substances such as ^{6}Li or ^{10}B to enable thermal neutron detection. NE320 loaded with 0.15% ^{6}Li gives a light yield of 31% of

anthracene (equivalent to $\sim$ 5400 photons/MeV) [57]. ^{10}B loaded liquid scintillators such as BC523A2 (2%) and EJ339A2 (2.5%) have light yields of 2450 and 2190 phe/MeVee (Photoelectrons/Mega Electron Volts Electron Equivalent) respectively [58]. Doping/loading comes at a cost as it usually increases the decay time of the scintillation, and decreases the light output (de-excitation without the production of radiation). This effect is known as 'quenching', and can be reduced by adding biphenyl or naphthalene to the solvent [28], or by decreasing the percentage of neutron reactive substance in the material [58].

Inorganic Scintillators

Crystalline inorganic scintillators are commonly alkali halides containing trace additives that function as activators. The main advantages of inorganic scintillators are high light output giving good energy resolution, and high stopping power due to greater density and higher atomic number [28]. However they can be hygroscopic, meaning they must be housed in air-tight-moisture-free environments e.g. LiI(Eu). Table 1.3 [59] [60]compares a number of thermal neutron sensitive inorganic scintillators, as well as a ^{6}Li-glass scintillator which will be discussed later in further detail.

Table 1.3: A comparison of some of the main properties of inorganic and glass scintillators capable of thermal neutron detection. Table derived from [59].

Host	Dopant	Density ρ (g/cm^3)	Abs. length at 1 Å (mm)	Light yield photons per		λ_{em} (nm)	τ (ns)
				Neutron	MeV γ		
^{6}Li-glass	Ce	2.5	0.52	$\sim$ 6000	$\sim$ 4000	395	75
^{6}LiI	Eu	4.1	0.54	50,000	12,000	470	1400
^{6}LiF/ZnS	Ag	2.6	0.8	160,000	75,000	450	> 1000
NaI	^{6}Li+Tl	3.7			35,000	419	230
Cs_2LiYCl_6	Ce	3.3	3.2	70,000	22,000	380	1000
$Cs_2LiLaBr_6$	Ce	4.2			40,000	420	180/1080

Crystalline ^{6}LiI is chemically similar to NaI, and when doped with europium it can produce $\sim$ 35% of the light output with respect to NaI:Tl (40,000 photons/MeV). ^{6}LiI has a decay time of 1.4 μs, and due to the crystal's high density the thinner slices may be used to achieve very efficient thermal neutron detection, e.g. 10 mm of highly enriched ^{6}LiI has an efficiency close to 100% for thermal neutrons [61] dropping to $\sim$ 90% at 1 mm thickness. Gamma-ray rejection capabilities for a ^{6}LiI:Eu crystal are poorer than that of typical gas filled proportional counters as the gammas can deposit more energy in the crystal. Similar to NaI, LiI is highly hygroscopic, meaning it cannot be exposed to water vapour and must be housed in an air-tight container. Although ^{6}LiI has promising thermal neutron detection efficiency and short decay

time, its hygroscopic nature poses engineering issues and its gamma-discrimination is too poor for SKADI.

Li co-doped NaI:Tl (NaIL), maintains most of the same scintillation qualities of NaI with the advantage of thermal neutron detection. NaIL demonstrates great thermal neutron/gamma pulse shape discrimination (Fig. 1.15). NaIL can be grown in large ingots exceeding 100 litres for use in portable monitors for border patrol or vehicle-mounted area monitors [62]. NaIL exhibits impressive detection efficiencies for large crystals (50×50 mm^2) with light output of $\sim$ 34,000 - 30,000 photons/MeV for 1 - 3% ^{6}Li doping respectively, outperforming other thermal neutron detection techniques such as ^{3}He tubes.

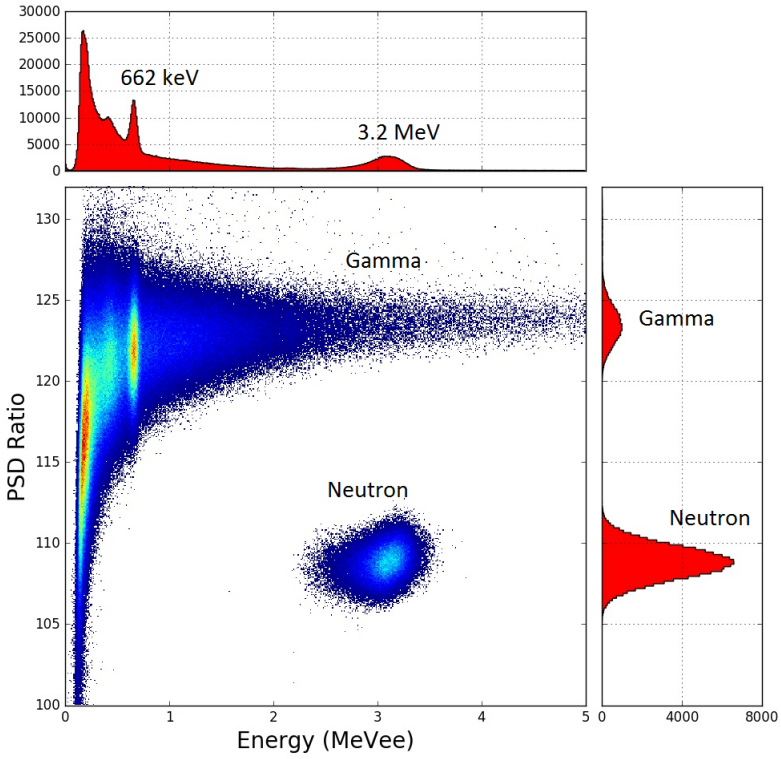

Figure 1.15: Pulse shape discrimination achieved using a 1% ^{6}Li doped NaIL crystal with a moderated ^{252}Cf neutron source and ^{137}Cs gamma source. The neutron energy is given as MeVee (electron equivalent). Image taken from [63].

The ^{6}LiF coated ZnS scintillator has a very high light yield for both neutron and gamma sources. ^{6}LiF/ZnS sparked the development of the $^{10}B_2O_3$/ZnS ceramic (on glass substrate) scintillator which boasts a 1.2-fold higher detection efficiency than ^{6}LiF/ZnS at 1 Å [64]. $^{10}B_2O_3$/ZnS scintillator has an estimated ^{10}B density of 6×10^{21} cm^{-2} [64] and is generally kept thin (1 - 2 mm) due to opaqueness of the ZnS to its own scintillation light and also to minimize path length uncertainty of the secondary ionising radiation to avoid undue degradation of position resolution. The transparency of the scintillator may be increased with the addition of H_3 [65]. The advantage however of using ^{6}Li over ^{10}B when doping or coating a scintillator stems from the large reaction Q-value (Eq. 1.6 and 1.7) of the output products, and the single

clean peak achieved with the ^{6}Li reaction as there is a single break-up channel of the ^{7}Li* compound nucleus.

Cs_2LiYCl_6:Ce (CLYC), shows a high light yield and a decay time $\sim 1\ \mu$s. The detector is sensitive to gamma-rays, and both thermal and fast neutrons through the ^{6}Li(n,α)t and ^{35}Cl(n,p) reactions respectively. Pulse shape discrimination can be achieved using the charge comparison method [66]. CLYC is hygroscopic which again leads to engineering issues for installation.

$Cs_2LiLaBr_6$:Ce (CLLB), is another promising inorganic scintillator with high light output, good proportionality and scalability [67]. However, the presence of ^{138}La and contamination from ^{227}Ac increase the internal radioactive background of the crystal, affecting the signal to noise ratio for thermal neutron detection, and decreasing PSD capabilities [68].

Gas Scintillators

Gas scintillators for thermal neutron detection [69] may use ^{3}He (Eq. 1.5). A 2D position sensitive detector was developed by A. Morozov *et al.* [70] for use in reflectometry and SANS instruments. The detector consists of a gas scintillator proportional counter filled with ^{3}He/CF_4 pressurised gas. The active volume is sandwiched between Micro-Strip Gas Chambers (MSGC) and a drift electrode mesh, followed by an output window and PMT-array (Fig. 1.16).

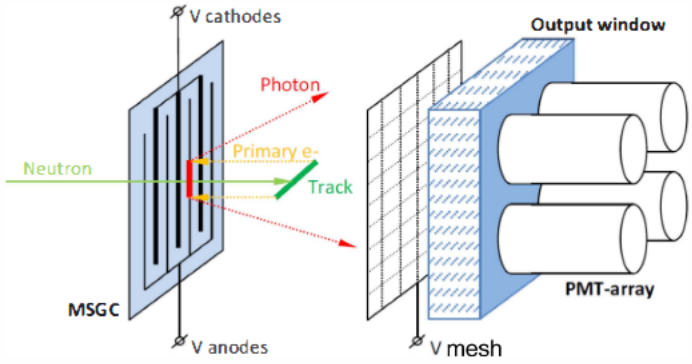

Figure 1.16: A conceptual design for the gas scintillator proportional counter. Image taken from [70] © 2012 IEEE .

The work hoped to achieve sub-millimetre position resolution, a rate capability > 1 MHz, and a high efficiency > 50%. In principle a hybrid detector could be made to operate at very high rates however, the current rate capabilities of this detector fell short of the 20 MHz requirement for SKADI, and the reliance on ^{3}He makes it irrelevant for use at the ESS.

Glass Scintillators

Glass scintillators (Ce activated silicates) for neutron detection applications are manufactured with varying concentrations of neutron sensitive elements such as ^{6}Li or ^{10}B, and are commonly used in neutron spectrometry, neutron radiography, and oil/gas exploration. The light output of

^{10}B doped glass is approximately ten times lower than ^{6}Li doped glass, and is therefore rarely used [28]. Glass scintillators are popular due to their fast response and short decay time ($\sim$ tens of ns). They are cost effective, durable, radiation hard, and chemically inactive with high melting points, making them ideal for applications in extreme environments. For neutron/gamma separation the glass sheet is kept thin and discrimination is achieved on the basis of pulse height, as there is effectively no PSD capability (discussed in Sec. 2.1.1). A thinner glass scintillator will have less thermal neutron detection efficiency, but will contribute to better position resolution when used in conjunction with a photo-sensitive detector. The light output of glass scintillators relative to anthracene is $\sim$ 25 - 30% [28]. Some examples of ^{10}B doped scintillators include GL-55, GL-535, G-127(2) and a mixed glass containing both ^{10}B and ^{6}Li Gl-173 (all found in Ref. [71]). The aforementioned ^{10}B doped glasses display timing uncertainties of $\sim$ 30 ns, however as mentioned previously their light output is comparatively lower than ^{6}Li doped glasses. Some examples of ^{6}Li doped scintillators include GL-232 [71], GS2 [72], GS20 [72] (row one of Table 1.3), KG2 [72], and ST-602 [73]. The most widely used on this list is GS20. GS20 has a lithium content of 6.6% which is enriched to 95% ^{6}Li. GS20 is the only scintillator listed which is sensitive to neutrons across an energy range of 0.01 eV - 6 MeV. For these reasons GS20 was chosen as the ideal scintillator for implementation in the SKADI instrument.

1.4 Photon Detectors

There are a number of position sensitive photon detectors to consider when aiming to detect thermal neutrons with a ^{6}Li loaded glass scintillator, a few of the main options are discussed below.

1.4.1 Multi-Pixel Silicon Photomultipliers

A silicon photomultiplier (SiPM) is based on a reversed biased p/n junction (boundary between two types of semiconductor materials) which can detect light between $\sim$ 350 - 750 nm in wavelength (near ultraviolet to near infrared) [74]. The main structural face of a SiPM is an array of minute highly sensitive pixels as shown in Fig. 1.17. Each micro cell is a Geiger-Mode avalanche photo-diode (GM-APD) [75].

SiPMs are extremely sensitive, highly efficient photon detectors with good timing resolution, suitable for low light applications down to the single-photon level. SiPM tiles come in sizes from $\sim 1 \times 1$ mm^2 to 6×6 mm^2. SiPMs are designed to have a high gain and detection efficiency, sensing around 30 - 40 % of the photons incident on the surface of the detector [76]-[77]. However, SiPMs are not radiation hard and sustained radiation damage limits their long term use. Therefore a SiPM would not be an appropriate option. When the call from the ESS for a solid state thermal neutron detector went out $\sim$ 10 years ago the signal-to-noise ratio of

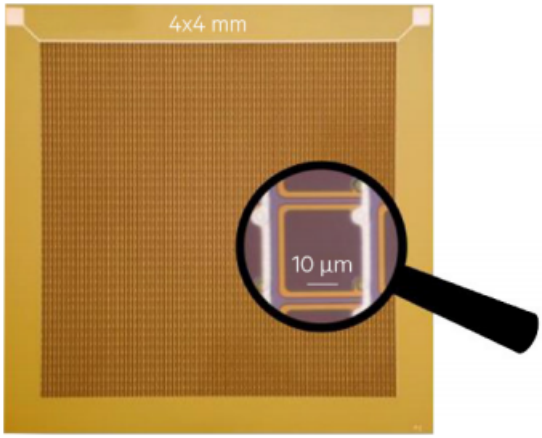

Figure 1.17: A 4×4 mm^2 SiPM interface, with individual pixel dimensions 10×10 μm^2 acting as a sensitive elements. Image taken from [74].

SiPMs was poor, this stemmed from high levels of dark current, therefore more mature detector technologies were considered.

1.4.2 Microchannel Plate Photomultiplier Tubes

A microchannel plate (MCP) is composed of numerous glass capillaries/channels arrayed in parallel to form a two dimensional detector. The individual channels have an internal diameter on the order of micrometres with the internal walls coated to produce secondary emission electrons, acting as independent electron multipliers. A diagram of the MCP arrangement and principle of multiplication are shown in Fig. 1.18. The electrons are accelerated by the electric field created by the voltage V_D applied across the input/output electrodes. The full MCP photomultiplier tube (PMT) is required for photon detection and consists of an input window, photocathode to provide electrons, an electric field to accelerate them, a MCP to multiply them, and an anode to collect the electrons.

MCPs boast high gains $> 10^5$ ($> 10^8$ can be achieved [79]), fast time response, two-dimensional detection with high spatial resolution (pixel size dependent), stable operation, and low power consumption [78]. Normally two MCPs are stacked to obtain sufficient gain. However if the gain becomes too high ion feedback can occur creating a very noisy signal. The lifetime of the detector becomes a major issue when dealing with high levels of radiation/background. The photocathode deteriorates during the electron multiplication process due to gas/ion build-up, decreasing the quantum efficiency of the detector. Some steps can be taken to increase the lifetime of the detector such as blocking the gas/ions from reaching the photocathode [80]. Depending on the photocathode material MCP-PMTs may need to be cooled during operation. The linear response of MCP-PMTs drops off at high photon levels, as a result of saturation effects, which limit the rate capabilities (Fig. 1.19) [81]. MCP-PMTs are also expensive in comparison to multi-anode PMTs, with the Hamamatsu R10754-07-M16 [82] priced at £20.65/mm^2 (effec-

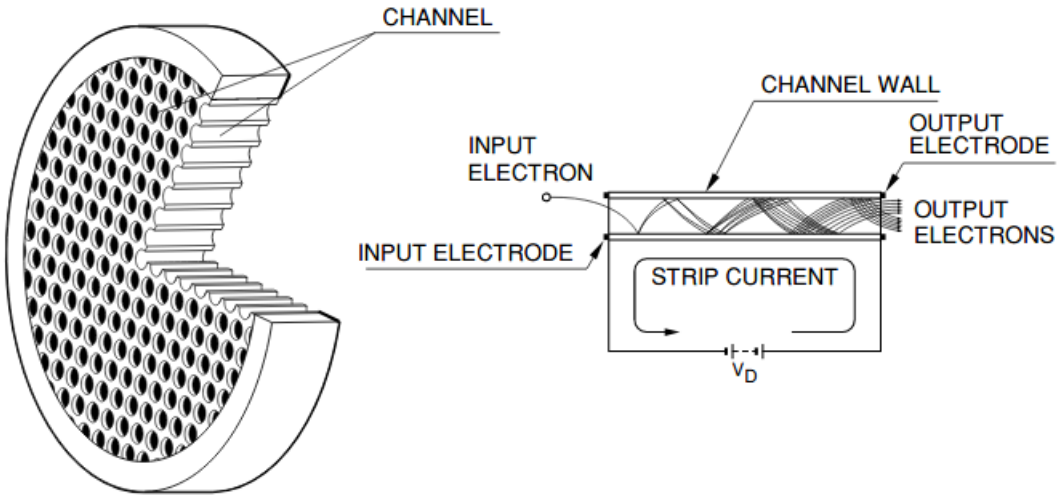

Figure 1.18: A cross-section of the MCP general design with a two dimensional array of separate channels (left), and an illustration of the channel's structure and electron multiplication process. Image taken from [78].

tive active area), compared to the Hamamatsu H14220A and H12700A MAPMTs [83] priced at £1.85/mm^2 and £1.36/mm^2 respectively.

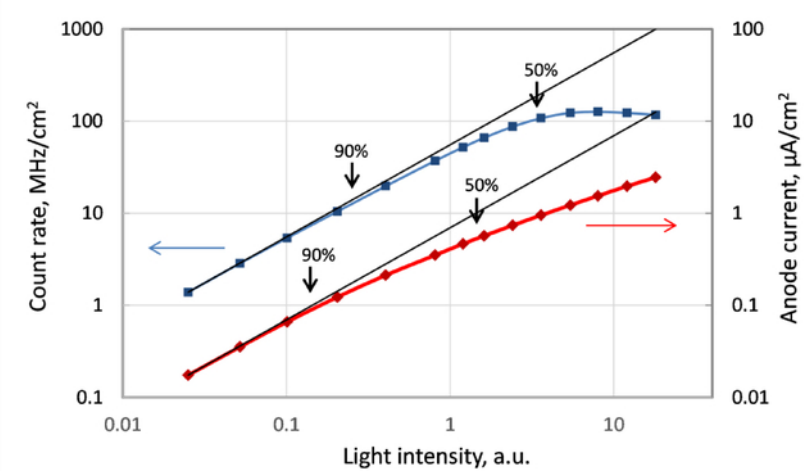

Figure 1.19: Averaged detector count rate (blue) and anode dc-current (red) as a function of continuous light intensity (LED source with 8 mm diameter illumination spot) for a conventional MCP-PMT (gain 10^5). The black lines represent the calculated theoretical linear behavior of the detector. The black arrows indicate the light intensities where experimental curves are within 90% and 50% of the theoretical linear output. Image taken from [81].

1.4.3 Multi-Anode Photomultiplier Tubes

Photomultiplier tubes are most commonly associated with scintillating devices and are used to convert light signals into a measurable electric current. A PMT (Fig. 1.20) is housed in a glass evacuated tube and is comprised of an optical input glass window/face plate through which the

light from the scintillator enters, followed by a photocathode which converts the photon into a photoelectron (external photoelectric effect). The photoelectrons are then directed and accelerated using focusing electrodes onto the primary dynode. The dynodes act as electron multipliers via secondary electron emission and create a cascade effect which results in current amplification ranging from 10 - 10^8 times (dependent on the number of dynodes, their structure/material, and the applied high voltage) [78]. The output electrons from the final dynode are collected on the anode producing a pulse of current. An example of the internal structure of a PMT is shown in Fig. 1.20. If the cathode and dynode systems are assumed to be linear, the current at the output of the PMT will be directly proportional to the number of incident photons [28].

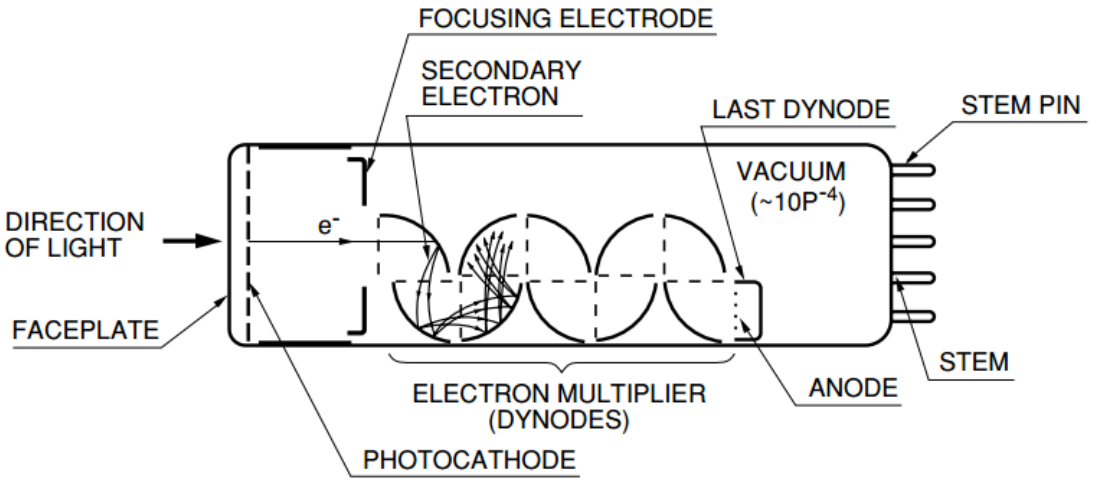

Figure 1.20: Diagram of a photomultiplier tube's internal design, including electron multiplying dynodes. Image taken from [78].

For position sensitive applications, pixellated PMTs such as multi-anode photomultiplier tubes (MAPMT) can be used. These come in a variety of pixel array dimensions (4×4, 8×8, 16×16 etc.). MAPMTs share a common optical window and photocathode material. However, to achieve position sensitivity, separate dynode chains and independent anodes are used to read out individual pixel areas of the photocathode. An 8×8 Hamamatsu H12700 MAPMT was selected for the SoNDe application.

The optical window of any PMT tends to absorb ultraviolet radiation, and the short wavelength limit is determined by the UV transmittance of the window [78]. UV-transmitting quartz can be used in applications, and extends the cutoff to 185 nm. The most common window material is borosilicate glass which does not transmit UV radiation shorter than 300 nm [78]. Borosilicate glass has a density of 2.23 g/cm^3, a refractive index of 1.473, and a B_2O_3 composition of $\sim$ 10%. The presence of boron, which has a 20% natural abundance of ^{10}B, indicates that some thermal neutron absorption may occur at the optical window of a detector (measured in a later chapter).

Photocathode materials are generally made of compound alkali metals with low work func-

tion. A typical example of a material used is the bialkali (Sb-Rb-Cs, Sb-K-Cs) which has a high sensitivity to photons and a low dark current. Photocathode sensitivity or 'conversion efficiency' varies with the incident light wavelength. This relationship is known as the spectral response and includes radiant sensitivity and quantum efficiency. The radiant sensitivity (S_K) can be expressed as

$$S_K = \frac{I_K}{L_P}, \tag{1.8}$$

where I_K is the photoelectric current generated by the photocathode and L_P the incident radiant flux at a given wavelength. The quantum efficiency (η) is the ratio of the number of photoelectrons emitted from the photocathode to the number of incident photons. It can be expressed as a percentage by the equation

$$\eta(\%) = \frac{hc}{\lambda e} S_K \cdot 100\%, \tag{1.9}$$

where h is Planck's constant, c is the velocity of light in vacuum, λ the wavelength of the incident light (nm), and e is the electron charge. As longer wavelength photons carry less energy than photons of shorter wavelengths they have a decreased likelihood of contributing to the photoemission probability. Therefore, the long wavelength limit is dependent on the photocathode material, and the distribution of S_K and η between the short and long wavelength limit is called the spectral response. In general the maximum quantum efficiency occurs at a wavelength slightly shorter than that of the peak radiant sensitivity.

Some of the main characteristics to consider when choosing a MAPMT are:

- Time response
- Gain uniformity
- Crosstalk
- Stability
- Dark current
- Signal-to-noise ratio.

The time response of a detector will be dictated mainly by the transit time uncertainty taken by the emitted photoelectrons to reach the anode. For the SKADI application the detector will need to withstand a high intensity radiation field (minimal dead time) and have μs time resolution capabilities. The sensitivity of the photocathode, dynodes and anode will deteriorate over time so that individual detectors will need to be re-calibrated on a regular basis. Crosstalk is the leaking of signal from one channel into neighbouring channels and occurs mostly within the dynode structures, HV biasing components, and pickup at the anode end. The stability of a detector can be assessed over a short period of time (drift) and over longer periods $\sim 10^3$ - 10^4 hours (life characteristics). Both drift and crosstalk are investigated in more detail in sections

2.2.2, 4.3.1, and 2.2.6, 4.7 respectively. Dark current is current that arises when the detector is operated in complete darkness. There are a number of causes of dark current including: thermionic emission (current from the photocathode and dynodes), leakage current (between the anode and other electrodes), and direct interactions of background ionising radiation with internal structures of the PMT. PMT dark current will in general make a significant contribution to the noise level of a scintillation counter if the scintillation intensity is low.

1.5 Summary

Given the criteria laid out by SKADI and taking into consideration the above characteristics, GS20 scintillation glass has a decay time of a few tens of ns, while the MAPMT has a small electron transit time (4.9 ns), small transit-time uncertainty (0.35 ns) and high quantum efficiency (33% at 380nm) well matched to the peak scintillation emission at 395 nm. The MAPMT pixel size is 6×6 mm^2, but sub-pixel position resolution in principle is possible if an amplitude-weighted mean position of active pixels is performed, as in an Anger Camera [84] [85]. This may be important when very small scattering angles are measured. This method may be employed with the detectors situated at the 'zero angle' position with respect to the sample.

Good spatial resolution gives good scattering-angle resolution which is necessary to achieve high resolution imaging of the scattering sample in the reconstructed pixellated image. If a pixel in the 400 module detector array dies, the image reconstruction software should have a process to work around/compensate for this. However, this will affect the image quality locally. The coverage of the detector is also not completely continuous (Fig. 1 of Ref. [86]), therefore edge effects will become apparent (as discussed in Sec. 5.3).

By combining a 1 mm thick GS20 glass scintillator with the H12700A MAPMT one can achieve a thermal neutron detection efficiency of $\sim 75\%$ [2] with good gamma-discrimination by pulse height, an estimated global (1×1 m^2) count rate capability of 37 MHz [86] (see tables.A.1 and A.2), and a modular design with no reliance on ^{3}He.

Chapter 2

SoNDe Design and Characterisation with Laser Light

2.1 The SoNDe Module

The Solid State Neutron Detector (SoNDe) module developed for ESS is comprised of a 64 channel 52 $\times$ 52 mm^2 (48.5 $\times$ 48.5 mm^2 active area) Multi-Anode Photomultiplier Tube (MAPMT) [83], a 50 $\times$ 50 $\times$ 1 mm^3 sheet of GS20 [72] ^{6}Li doped glass scintillator, and a portable data acquisition (DAQ) [87]. The scintillator and detector are 'dry' fitted, meaning there is no optical coupling agent, such as epoxy or silicone, between them. The ESS hopes to achieve a pixel resolution of $\sim$ 6 $\times$ 6 mm^2 (or better) [24] using this detector configuration. In Fig. 2.1 the MAPMT, portable DAQ, and integrated circuit system are displayed from left to right. For the

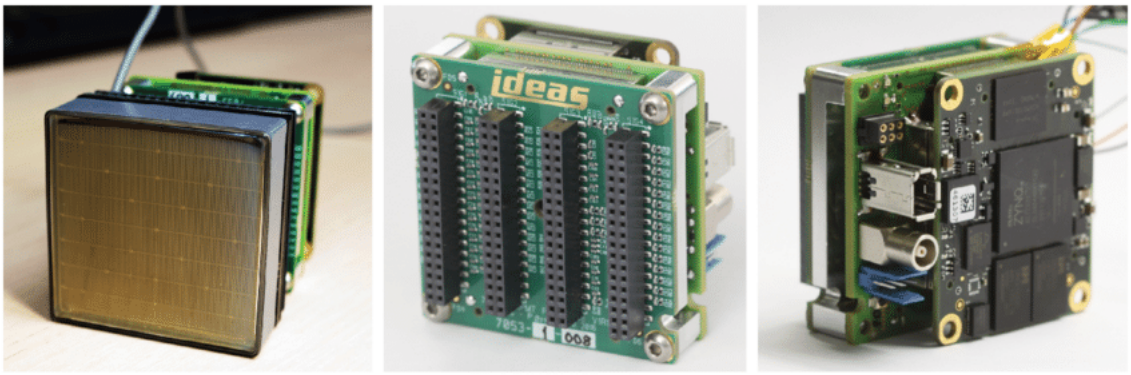

Figure 2.1: L-R:The SoNDe module (minus scintillator), the portable DAQ pin connection array, and the integrated circuit view. Image taken from [88].

characterisation studies conducted in Glasgow a VME (Versa Module Europa) based data acquisition and AcquRoot [89] analysis software were used instead of the portable DAQ. This setup will be referred to as the 'SoNDe Test Module'. The portable DAQ will be used in the final setup at ESS.

2.1.1 GS20 Scintillator Glass

GS20 is a Ce-activated aluminosilicate scintillation glass which contains 6.6% lithium, of which 95% is ^{6}Li [72]. The scintillator is manufactured by Saint-Gobain[1] and its dimensions span 50 $\times$ 50 $\times$ 1 mm^3. The key properties of GS20 are shown below in Table 2.1.

Table 2.1: GS20 key properties. Information taken from [72]

Key Properties	**GS20**
Density [g/cm^3]	2.50
Light output relative to anthracene*	20-30%
Decay time†, neutron excitation [ns]	18 / 57
Decay time†, alpha excitation [ns]	16 / 49
Decay time†, beta excitation [ns]	20 / 58
Wavelength of maximum emission [nm]	395
Refractive index at maximum emission	1.55

*Determined by thickness, increasing with decreasing thickness down to approximately 2mm.

†Fast and slow component respectively.

^{6}Li has a thermal neutron (0.025 eV) capture cross-section of 936 $\pm$ 6 barns [90]. The neutron is captured by the ^{6}Li which decays into alpha and triton particles. These secondary particles ionise the $Ce^{(3+)}$-activated aluminosilicate molecules in close proximity to their capture location, with the alpha and triton ranges in GS20 being approximately 7 μm and 36 μm respectively [91]. The reaction

$$^6_3\mathrm{Li} + ^1_0\mathrm{n} \rightarrow ^7_3\mathrm{Li}^* \rightarrow ^4_2\mathrm{He} + ^3_1\mathrm{H} + 4.78 \ \ \mathrm{MeV} \tag{2.1}$$

releases 4.78 MeV of energy, split between the alpha (2.05 MeV) and triton (2.73 MeV). The detection efficiency of the scintillation glass is approximately 75% at 1 mm thickness for thermal neutrons (0.025 eV), producing $\sim$ 6000 photons per absorbed neutron. The scintillator cannot distinguish different forms of radiation on a pulse shape basis as the decay times are not sufficiently separated, therefore discrimination must be done on a pulse height basis (Fig. 2.2). The 1 mm thickness of the scintillation glass results in low detection efficiency for gamma rays which are expected to be a major source of background.

2.1.2 Hamamatsu H12700A MAPMT

The model H12700A is a metal channel dynode type MAPMT with matrix anode layout. The detector response ranges from 300 - 650 nm with typical quantum efficiency of 33% at $\sim$ 350 nm and cathode radiant sensitivity maximum at $\sim$ 380 nm [83]. The active area of the detector is 48.5 $\times$ 48.5 mm^2, which is 87% of the total area occupied. A typical gain of 1.5 $\times$ 10^6 can be achieved at -1000 V, which increases up to $\sim$ 3.0 $\times$ 10^6 at -1100 V. Typically the gain can vary

[1]GS20 ® Scintacor

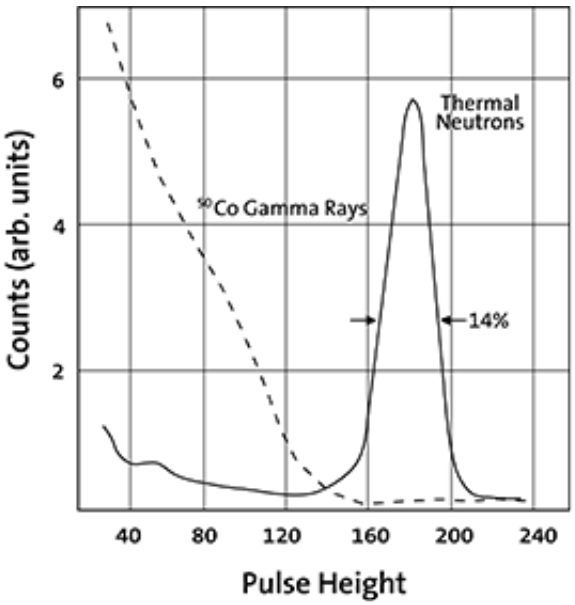

Figure 2.2: The spectra of thermal neutrons (0.025 eV) and gamma rays from ^{60}Co in GS20 scintillator separated on the basis of pulse height. Image taken from [92].

by a factor 2 from pixel to pixel, and up to a factor 3 in the worst case. The faceplate/optical window is made of borosilicate glass. The photocathode is composed of a bialkali compound and the photoelectrons ejected from it are focused through a mesh before entering the metal channel dynode chain. The H12700 has a 10-stage dynode chain and a schematic of the dynode structure is displayed below in Fig. 2.3. The advantages of using metal channel dynodes for the SKADI instrument include, low cross talk between secondary electron paths for different channels and relatively good uniformity across active pixel areas.

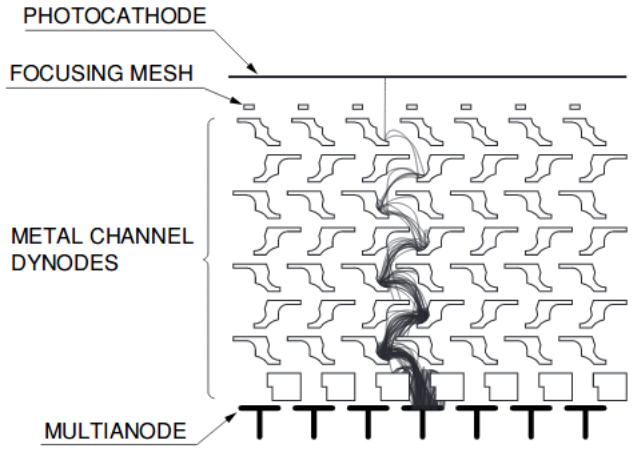

Figure 2.3: A diagram of the dynode chain electrode structure. The photoelectron is directed through the focusing mesh, is multiplied along the metal dynode chains, and the current is recorded at the anode. Image taken from [78].

Crosstalk

Crosstalk in a multichannel system is the leakage of the signal from one channel to another adjacent channel [78]. There are a number of factors which contribute to crosstalk including, electron dispersion across neighbouring metal dynode chains, and scattering of incident light within the optical window/faceplate. The results for the crosstalk measurement of the detector are discussed in Sec. 2.2.5.

Uniformity

The anode uniformity (pixel relative gain map) measurement provided by Hamamatsu for the MAPMT used in the majority of tests in this thesis is shown in Fig. 2.4. Hamamatsu achieved this by using a Tungsten lamp with a blue filter and a mask for the detector face, separately illuminating every pixel with a 6 mm square spot. The highest gain pixel is assigned a value of 100 (%) and all other pixel gains expressed as a percentage of this. The gain variation of the detector will be explored later in Sec. 2.2.3.

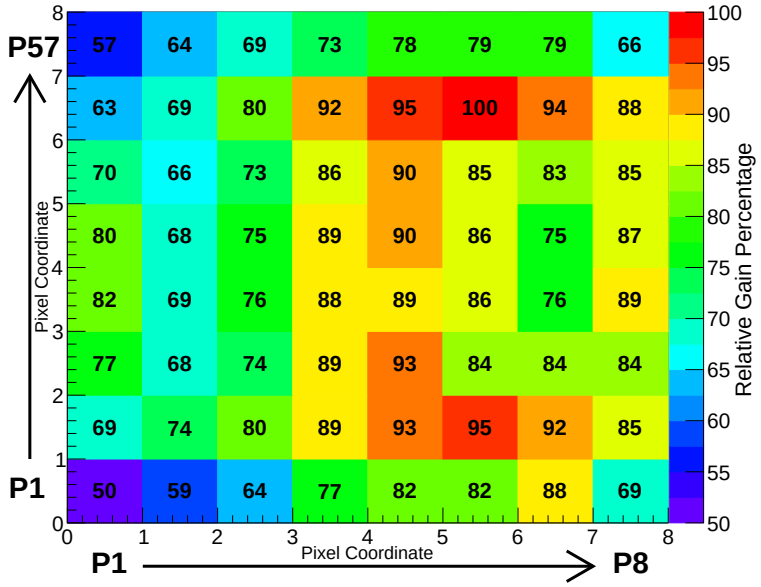

Figure 2.4: Hamamatsu relative pixel gains for H12700A MAPMT Serial No. LA0125 represented as a 'heat map' with P1 located bottom left and P64 top right. The standard deviation of the relative gains across all 64 pixels $\sigma = 11$ %.

2.1.3 IDEAS ROSMAP-MP DAQ

The self-contained DAQ displayed in the centre of Fig. 2.1 was specifically designed as a portable readout module for Hamamatsu MAPMT models 8500C and H12700. The portable DAQ has dimensions $50 \times 50 \times 55$ mm^3 and a mass of 113g. Considering that there will be

$\sim$ 400 SoNDe modules in the SKADI setup, the DAQ's compact size and lightweight nature is ideal for close packing/minimal dead-space and makes the design of housing and support frames easier whilst greatly reducing the need for bulky cabling and crates of electronics. Signals from the MAPMT pixels are amplified and shaped (1.4 μs time constant) before passing to a discriminator and 13-bit ADC. The discriminator thresholds are individually programmable to compensate for non-uniformity of gain and the outputs are time stamped by an internal clock which has a resolution of 10 ns. Control of the DAQ system and readout of the data acquired are performed via an ethernet interface, so that these tasks can be handled by a standard personal computer (PC). The system has two operational modes: spectroscopy and timing. The former will be used for calibration purposes. It returns channel ID, pulse height and time stamp for all active pixels and can operate at rates up to $\sim$ 10 kHz (observed in practice). The latter will be used for time-of-flight measurements as it transfers channel ID and time stamp only at rates up to 250 kHz [2] per module, i.e 100 MHz over the entire detector which is substantially greater than the required 20 MHz.

2.1.4 VME Based DAQ and AcquRoot

As previously mentioned, a VME based DAQ and AcquRoot software were used during characterisation studies in Glasgow as this gives increased flexibility with respect to signal processing and data handling.

The VMEbus is a parallel communication bus which connects modular electronics, housed in a powered rack-mounted crate. Modules include a master bus controller and slave modules such as Analogue-to-Digital Converters (ADC) and modules such as programmable discriminators and logic modules. The present VME hardware uses the 32-bit (address and data) version of the VMEbus although 64-bit versions are now available [94].

AcquRoot is based on the ACQU software tools for the acquisition and analysis of data from nuclear and particle physics experiments, used mainly but not exclusively within the Mainz A2 collaboration [89]. The AcquRoot analyser is built on the framework of ROOT [95], the CERN C++ based suite of software tools and libraries [89].

AcquRoot also includes AcquDAQ, a C++ based data acquisition software designed around a set of classes which implement control and readout functions for a diverse set of hardware, e.g. VME, CAMAC etc.

2.2 Laser Based Detector Characterisation Studies

Throughout this investigation the SoNDe Test Module was studied using a variety of radiation and light sources which include: alpha particles, thermal and fast neutrons, gamma-rays, and laser light. These sources were used to determine the realistic response of the detector to both

the thermal neutrons of interest and possible background radiation. This will provide an insight into the detector's response when placed in-situ at the ESS. The laser based characterisation studies use a controllable light source and provide an understanding of the MAPMT's structure and response to photons of a similar wavelength to the scintillation photons. Two SoNDe Test Module detector units were used throughout these studies. The H12700A MAPMT Serial Number (S/N) LA0125 was used in the majority of the tests, and H12700A MAPMT S/N ZA0250 in Secs. 4.6 and 6.3 only. The sheets of GS20 scintillation glass used were similar for both test modules.

2.2.1 Motivation and Setup

The SoNDe module is designed to serve as a position sensitive device. Before directly extracting the position of the incident radiation one needs to understand the intrinsic non-uniformities of the detector's response and effects of crosstalk which may compromise position determination. Laser scans across the sensitive area of the detector were performed to study the response of the MAPMT in detail. Laser scans can be used to reveal a number of unique characteristics inherent to each individual detector, some of which include the gain variation across the pixel array, and crosstalk between pixels.

The scans were performed using the electronic setup shown in Fig. 2.5. The laser controller fires a short (35 ps) laser pulse and also supplies a Transistor-Transistor-Logic (TTL) trigger pulse. This is converted to the Nuclear Instrumentation Module (NIM) standard, shaped to $\sim$ 100 ns width and timed via cable delays for the leading edge to occur $\sim$ 20 ns before the delayed anode pulses from the MAPMT. This pulse provides the gate for the Charge to Digital Converter (QDC) modules, which determines the period over which anode charge is integrated. The VMEbus master (CAEN2718) is connected to a PC via an optical link to the PCI bus of the PC. It provides an event-readout "interrupt" to the PC and also resets the trigger busy signal when readout is complete.

A 2mW pulsed laser [96] with wavelength λ = 403.8 $\pm$ 1.7 nm [97] and variable beam divergence was mounted onto a motorised Thorlabs NRT150 X-Y translator inside a light-tight box. The size, behaviour and stability of the laser spot was determined using a Hamamatsu C9260-901 CCD camera. Millimetre stepped scans were then performed at intensities producing approximately single photoelectrons (PE) and 60 PE at the photocathode. The scans started in the dead space above P1 (red dot) and finished in the dead space below P64 (green dot), mapping from left to right then resetting to begin a new line as seen in Fig. 2.6.

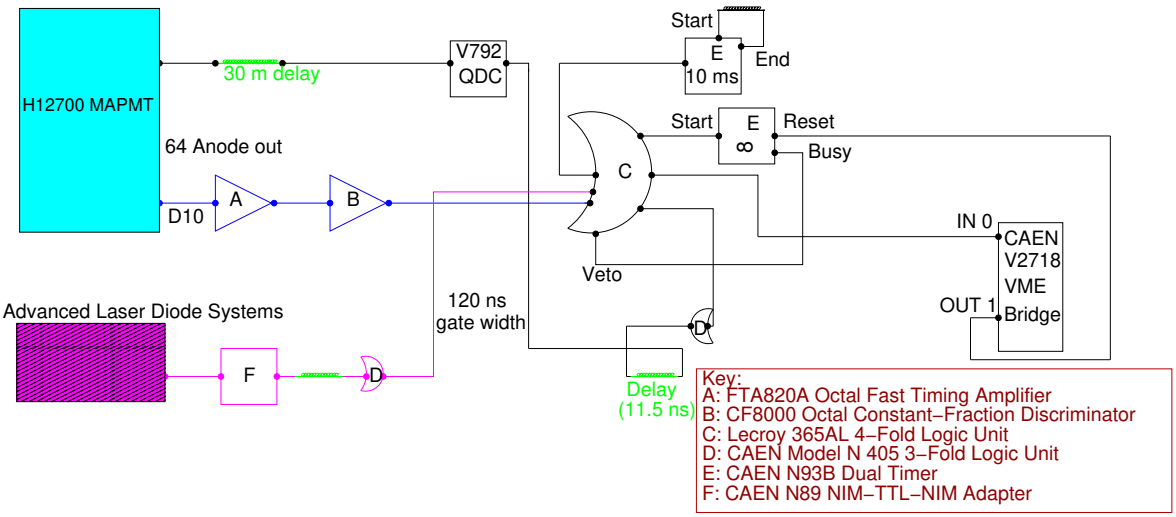

Figure 2.5: Laser (404 nm) trigger setup for MAPMT detector scans.

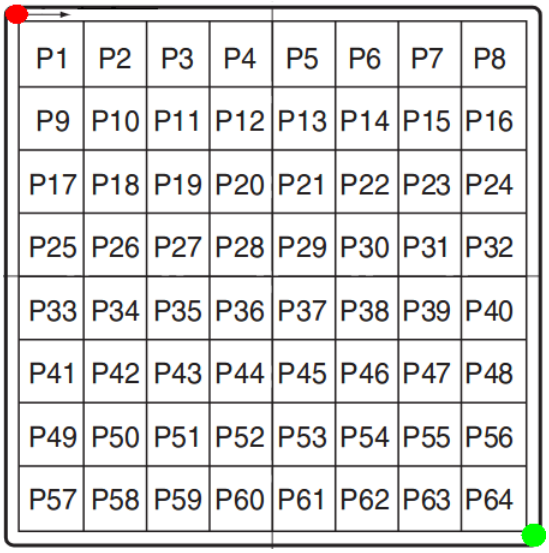

Figure 2.6: Laser start (red) and finish (green) positions for millimetre stepped scans of the MAPMT face. Modified from [83].

2.2.2 Laser Characterisation and Stability

Blue Spot Laser Characterisation with a Charge-Coupled Device

The Charge-Coupled Device (CCD) measurement setup can be seen in Fig. 2.7. The effective area of the camera is 8.67 $\times$ 6.60 mm^2, with individual cell sizes measuring 6.45 $\times$ 6.45 μm^2, and a quantum efficiency of $\sim$ 45% at 404 nm [98]. The measurements were carried out by moving the CCD camera along the Z-axis and aligning the laser perpendicularly to the detector. The laser repetition rate was set to 60 MHz (producing high intensity so any abnormalities would be clearly visible in a short time), laser pulse amplitude = 75%, and pulse width = 35 ps. The images were analysed using the associated Hamamatsu HCImage software.

Fig. 2.8 displays images from the CCD camera positioned at well separated points along the

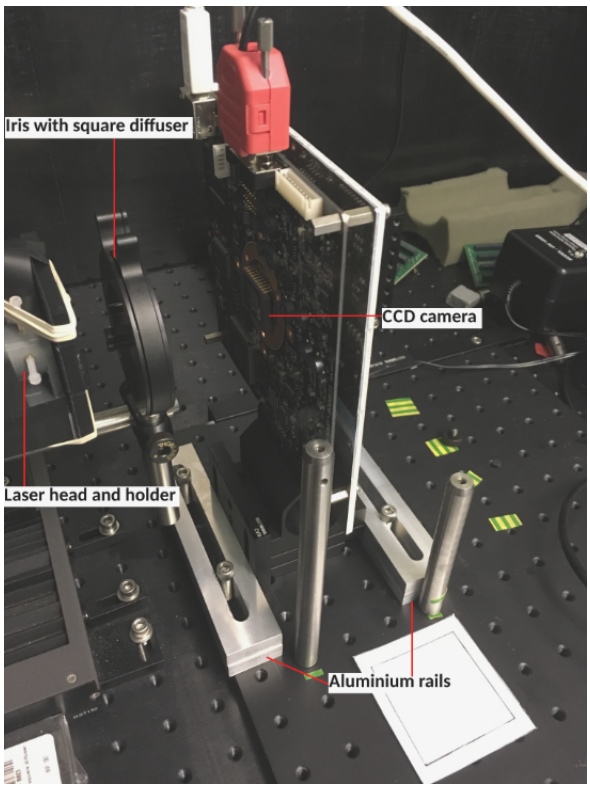

Figure 2.7: The CCD camera setup between two aluminium rails which hold it in a fixed position. The laser holder is situated left, within the adjustable grey tube. The iris used to hold the square diffuser (relevant to Sec. 2.2.5) is positioned between the laser and CCD.

Z-axis, approximately 45 mm and 195 mm from the detector, corresponding to spot diameters measuring $\sim$ 1.55 mm and $\sim$ 4.45 mm respectively. The central position of the spot deviates in the X-direction by $\sim$ 90 pixels, equivalent to 0.58 mm (pixel dimensions 6.45 $\times$ 6.45 μm^2). This corresponds to an offset of 0.2 degrees from the perpendicular. This slight misalignment is not significant. A portion on the right side of the beam appears less intense, and a 'halo' outlines the beam circumference at the furthest position from the laser. At a spot diameter of 1.0 mm, repetition rate of 1.0 kHz, laser pulse amplitude = 50 %, and pulse width = 35 ps these effects become negligible.

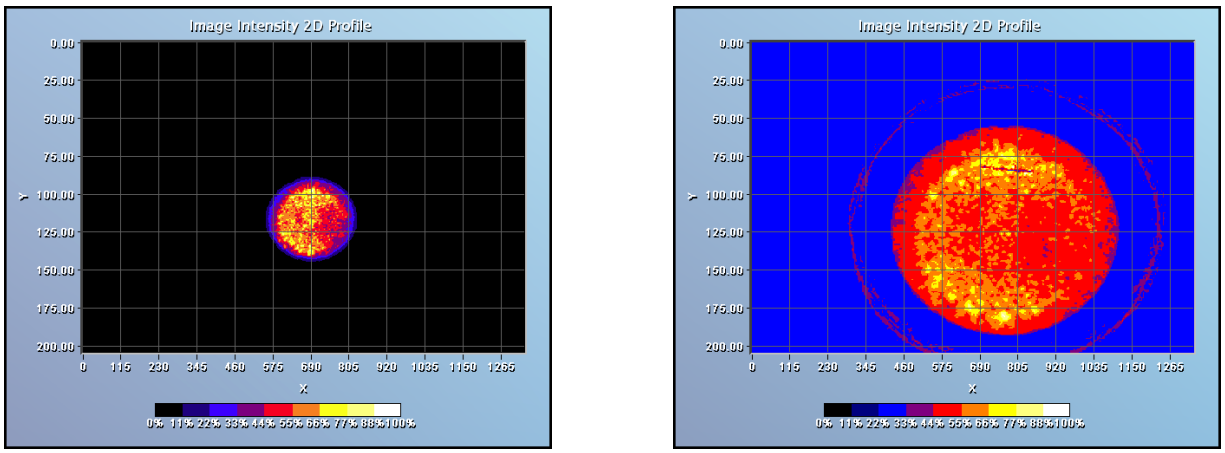

(a) (b)

Figure 2.8: 2D intensity images of the laser spot light at extreme positions on the Z-stage. (a) was positioned at 45 mm with respect to the laser and has a spot diameter of $\sim$ 1.55 mm. (b) was positioned at 195 mm with respect to the laser and has a spot diameter of $\sim$ 4.45 mm. An offset in spot centre was calculated in the X-direction as 0.58 mm. A non-uniformity of the laser head is visible on the right of both images, and a halo surrounds the larger spot.

Focal Point and Laser Diameter

The focal point (smallest diameter measurable for laser beam) for the setup was measured to be Z = 56.45 mm $\pm$ 0.5 mm. The diameter of the laser at this point was found to span approximately 44 $\pm$ 2 pixels in the X-direction. Each pixel measures 6.45 μm, so this would equate to a spot diameter of approximately 0.284 mm $\pm$ 0.013 mm. The angular divergence of the laser beam is therefore θ = 0.9 degrees. The settings for a mm spot size are 155 $\pm$ 2 pixels in the X-direction, as displayed in Fig. 2.9 and this was achieved at a distance of 65.73 mm $\pm$ 0.5 mm. The intensities in the X and Y directions are shown in Fig. 2.10.

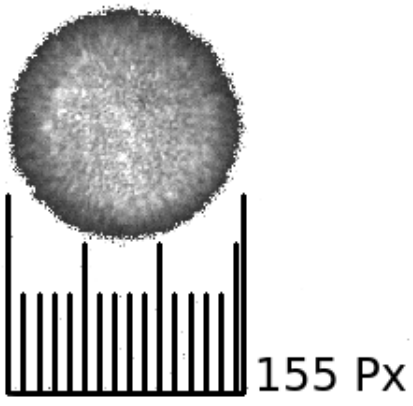

Figure 2.9: Millimetre spot size for the blue laser was found to be 155 pixels wide in the X direction.

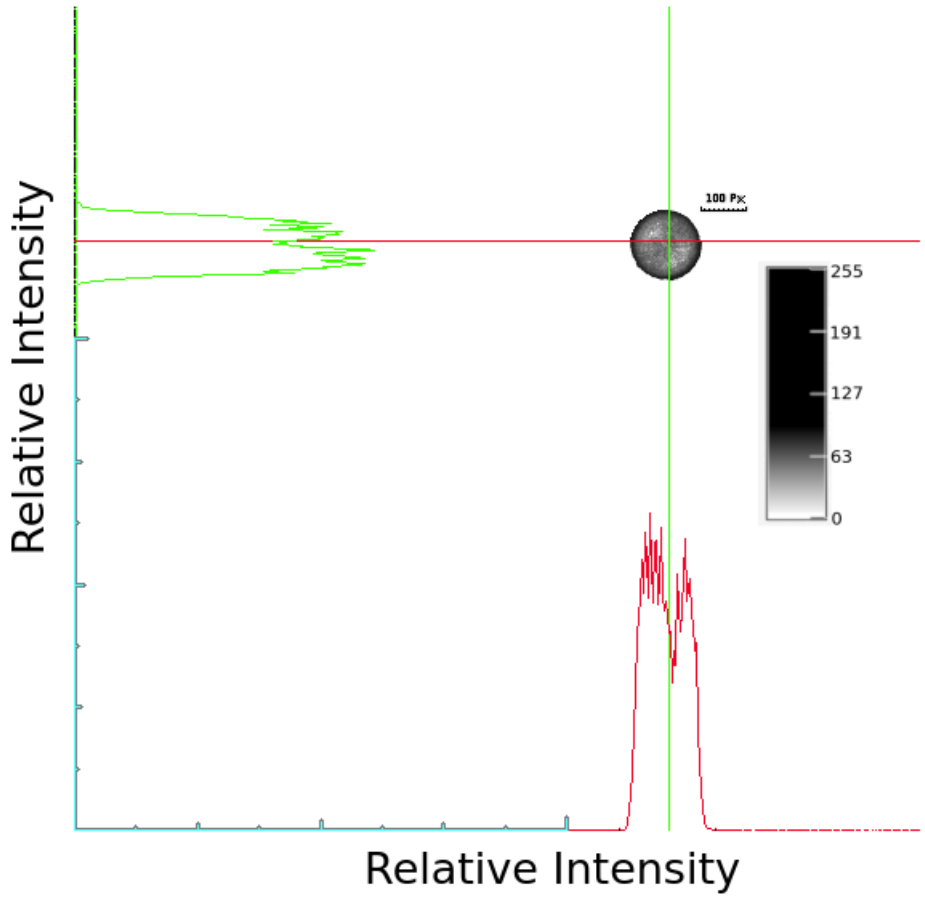

Figure 2.10: The relative X and Y intensities of a mm spot cross-section highlighted in red and green respectively. The grey-scale Z axis indicates the increasing beam intensity from light to dark. The intensity across both the X and Y axes show a dip indicating a slight non-uniformity in the laser head.

System Stability Test

The purpose of this test was to determine the output variation/stability of the MAPMT operated at -1000 V (the recommended HV for the H12700) when started from 'cold'[2] and run for an extended period ($\sim$ 34 hours). 'Drift' refers to instability measured over a short time period, whereas variations observed over longer time periods (10^3 to 10^4 hours) are referred to as 'life characteristics'. The cathode sensitivity of MAPMTs tends to remain stable over long periods of operation, therefore drift and life characteristics are related to the electron multiplication stages of the detector [78]. This means gain variations within the pixels will be expected over time. The ESS will be using $\sim$ 400 of these detectors and a knowledge of their stability under certain start up/running conditions is critical.

The laser was initially warmed up for 15 minutes and directed at the centre of pixel 45 (P45). The detector was switched on 10 seconds before the DAQ software was set to start. The results are shown in Fig. 2.11. The mean QDC channel of the P45 spectrum was plotted against time.

[2]turned off completely and left to rest for several hours

As the detector warmed up the mean decreased rapidly in the first 60 minutes by $\sim$ -1.94 $\times$ 10^{-3} QDC bins/s, followed by a more gradual drift. A linear fit of the mean channels between times 3600 and 124000 seconds produced a slope of -1.48 $\times$ 10^{-5} QDC bins/s, expressed as a percentage per hour as 1.15 $\times$ 10^{-4} %/hr. Hamamatsu recommend a warm-up period of 30 - 60 minutes (black dashed line indicates the 60 minute mark) for initial phase operation of their tubes (from 'cold'), and a shortened warm-up period after long periods of operation [78]. This recommendation should be followed by the SKADI group when operating the MAPMTs and investigations into the lifetime characteristics of the detectors should be explored. Each detector should have its relative pixel gains re-calibrated periodically to ensure that the results remain consistent.

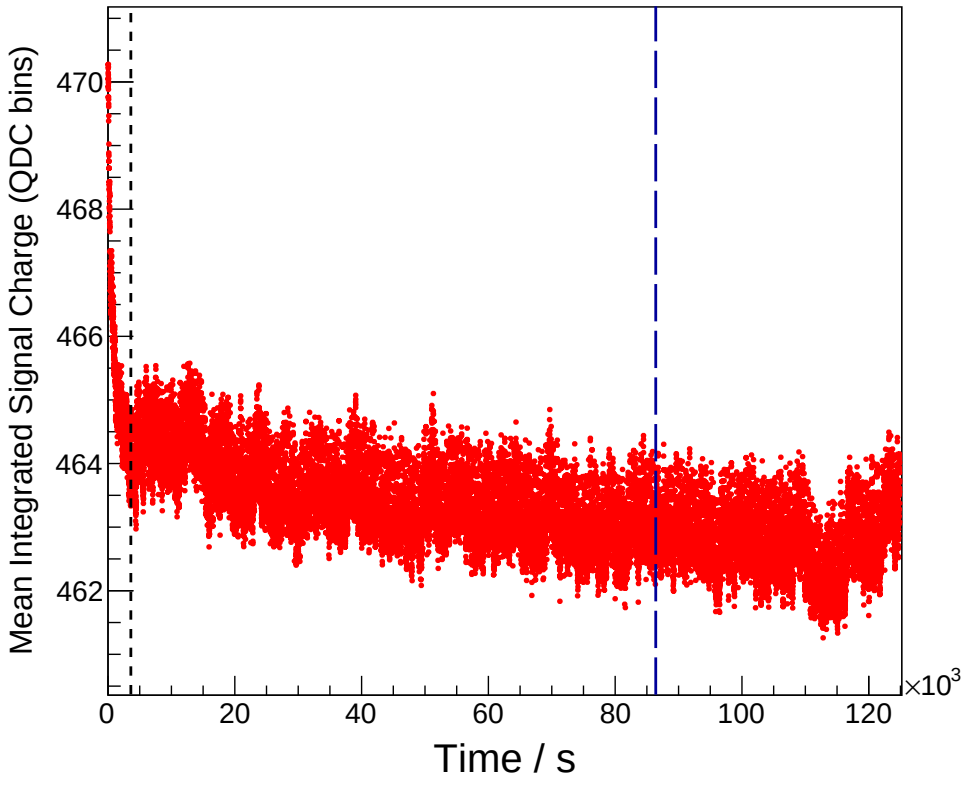

Figure 2.11: System stability test performed using the blue laser centred on P45 shows the mean integrated signal charge variation against time in seconds, over approximately 34 hours. The black dashed vertical line represents 60 minutes, the period of time Hamamatsu recommends for warm-up, and the blue dashed line represents the passage of 24 hours.

2.2.3 Multi-Photoelectron Level Scans

Single PE scans were performed on the MAPMT to test the detector's sensitivity, calibrate its gain at low light intensities, and to help set the 60 PE light level (the original estimation [99] for the number of PEs one would expect for a thermal neutron capture reaction in the ^{6}Li scintillator calculated for a similar H12700A MAPMT S/N ZA0250, discussed in the next section). To reach low levels of intensity, Neutral Density Filters[3] (NDF) of varying Optical Density (*OD*) were used to attenuate the laser light intensity. The Optical Density and Transmission (T) relationship can be written as

$$OD = log_{10}\left(\frac{1}{T}\right), \;\; or \quad T = 10^{-OD} \tag{2.2}$$

where T is a value between 0 and 1. It is expected that the production of a few PE follows Poisson statistics. To verify the single PE level the expected value (μ) of the Poisson formula has to be ≤ 1 PE producing the pulse. Below, Equation 2.3 shows the standard Poisson equation, wherein k denotes the actual number of PEs produced.

$$P(k;\mu) = \frac{e^{-\mu}\mu^k}{k!} \tag{2.3}$$

where μ is defined as

$$\mu = mp, \tag{2.4}$$

m is the mean number of photons hitting the photocathode, and p is the quantum efficiency of the photocathode [100]. The parameter μ is determined by a number of factors, which include: the mean number of photons incident on the photocathode, the quantum efficiency of the photocathode, and the collection efficiency of the dynode system.

The Gaussian Distribution used to characterise the pedestal and photon peaks (Fig. 2.12) is given as

$$N(x;\mu,\sigma) = \frac{1}{\sqrt{2\pi\sigma^2}} e^{\left[-\frac{(x-\mu)^2}{2\sigma^2}\right]}. \tag{2.5}$$

From these first principles a gain calibration fit function was developed by M. Mirazita [101]. This was derived from the mathematical description of the PMT [102] single PE response which is explained by R. Perrino *et al.* [103]. The pedestal (PED) contribution to the spectrum, which includes electronic noise/background, is defined as,

$$\text{PED} = e^{-\mu}\left(\frac{1-w}{\sigma_0\sqrt{2\pi}} e^{\left[-\frac{(q-Q_0)^2}{2\sigma_0^2}\right]} + w\theta(q-Q_0)\frac{1}{\lambda}e^{(-q-Q_0)/\lambda}\right). \tag{2.6}$$

The pedestal peak is the zeroth PE peak. The variable q denotes QDC bin number, Q_0 the mean position of the pedestal peak, and w its contribution fraction defined by a decreasing exponential

[3] Kodak Wratten 2 Optical filters

tail for constant λ.

The fit function for the full single photoelectron spectrum (including pedestal contributions) is described below in Equation 2.7.

$$f(q) = A\left(\mathrm{PED} + \sum_{k=1}^{N_{Max}} \frac{e^{-\mu}\mu^k}{k!} \frac{1}{\sigma_1\sqrt{2\pi k}} e^{\left[-\frac{(q-Q_k)^2}{2k\sigma_1^2}\right]}\right). \tag{2.7}$$

A is a normalisation parameter for the fit, k denotes the photoelectron number (up to a maximum value of N_{Max}), and μ represents the expected number of detected photoelectrons. The function describes the addition of the Poisson weighted pedestal contributions (PED) with the Gaussian smeared Poisson distribution from the photoelectron contributions.

The standard deviations of the Gaussian distributions are given by $\sigma_k = \sigma_1\sqrt{k}$ and their mean positions as $Q_k = Q_1 + d(k-1)$, where d is the inter-peak distance in units of QDC bins. The absolute gain is measured as the distance between the pedestal peak and single photoelectron peak. The fit function also returns the mean value, μ which as described previously corresponds to the photoelectron level of the charge spectrum.

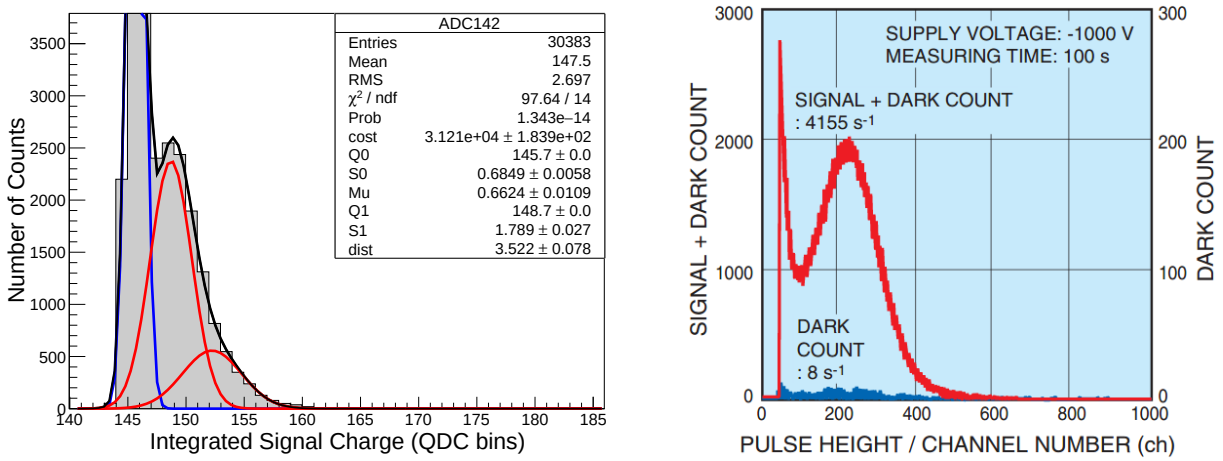

(a) (b)

Figure 2.12: (a) Single photoelectron level verification for P45 with μ = 0.66. The pedestal peak Gaussian distribution is outlined in blue with Q_0 = 145.73 ± 0.08, and photon peaks in red with Q_1 = 148.74 ± 0.09. (b) Hamamatsu H12700A single photoelectron level spectrum. Image taken from [83].

The single PE spectra for P45 at HV = -1000V is shown in Fig. 2.12a. The pedestal peak is shown in blue, the summed individual photoelectron peak in red with a secondary peak representing 2 PE level, and the overall fit defined in the function Equation 2.7 in black. The mean value μ for P45 = 0.66 ± 0.01, consistent with a single PE intensity level. This method was performed without a calibrated reference detector, therefore the spectra can be assumed to be 'low-photon level' as opposed to absolute single photon level [104]. However, they will be

termed 'single photoelectron'-level for the sake of the studies.

The absolute gain of the H12700 MAPMT S/N LA0125 given by Hamamatsu is 0.84×10^6 (Fig. A.1) at a high voltage of -1000 V. The absolute gain (G_{abs}) can be found via the equation

$$G_{abs} = \frac{((Q_1 - Q_0)[\text{QDC bins}]) \times (100[\text{fC}])}{e}, \tag{2.8}$$

where e is the charge of an electron, Q_0 and Q_1 were obtained from the peak channels of the QDC distributions and the nominal QDC conversion gains (100 fC/channel). For P45, a relatively high gain pixel, the absolute gain is found to be 1.88×10^6, larger in comparison to the value quoted by Hamamatsu. The calculation does not take into account the attenuation of the signal from the anode to the QDC modules, therefore there is a large uncertainty in the absolute gain of P45 which could be out by a factor of 2 or more. The higher gain of P45, or the calibration of the single PE level may also contribute to this larger value.

The quality of the single PE fit varies from pixel to pixel due to gain variations across the detector. In the case of the MAPMT used, some pixels were too poor to clearly resolve the single PE peak as more than a shoulder. The gain variations were studied (Sec. 2.2.3) by scanning the whole detector in mm steps to reveal intricate differences in the detector's response as the laser crossed pixel boundaries.

Expected Light Level For Thermal Neutrons

As mentioned at the beginning of Sec. 2.2.3 the single PE level was used to set the 60 PE light level (approximate light output of a thermal neutron event). This figure was derived from the equation

$$q = G \times n \times e, \tag{2.9}$$

where q is the mean charge of the signal converted from QDC bins to Coulombs (1 QDC bin = 100 fC), G is the absolute gain of the MAPMT supplied by Hamamatsu, n is the number of photoelectrons expected, and e is the charge of an electron (1.6×10^{-19} C). Using the P45 moderated AmBe spectrum as an example (Sec. 5.6, Fig. 5.12), the mean position of the signal peak in QDC bins (minus the pedestal peak) is 88, giving a charge of 13.5 pC. The absolute gain for the MAPMT (0.84×10^6) was used instead of the P45 absolute gain, due to its large uncertainty. This gives a total number of photoelectrons as 100.4. Due to availability of neutral density filters and previous estimations, approximate light levels of 60 PE and 120 PE were used to emulate thermal neutron events for full detector illuminations and fine scanning laser data.

Stepped Scan of MAPMT

For the low light level scans the laser spot size was set to 1.0 mm diameter by adjusting the detector position from the laser source along the Z-axis. The detector was operated at -1000 V and scanned at both single and $\sim$ 60 PE levels, with and without the addition of the scintillator. The 60 PE level (approximate PE output for a thermal neutron) was obtained using its peak position in QDC bins via the equation

$$Q_{60} = Q_1 + d(60-1), \tag{2.10}$$

where Q_{60} and Q_1 are the mean of the 60 PE and single PE peaks respectively, and d is the single-PE inter-peak distance in units of QDC bins. Due to the number of free parameters in the fit function (Eq. 2.7) the uncertainty in d will be much larger than that quoted in Fig. 2.12a. The limitations of the fit function mean the variation of d could differ by a factor of 2 or 3. Noise contributions from the system may also have affected the widths of the peaks.

One of the main reasons these detectors are being used at ESS is their position resolution, which will depend on the uniformity of the MAPMT response. The mm scans can reveal whether the structural boundaries between pixels have a significant effect and if the response within a pixel varies. They also show the extent of crosstalk between adjacent pixels. The results can be seen at single PE level in Fig. 2.13 and at $\sim$ 60 PE level in Fig. 2.14 for a pixel layout shown in Fig. 2.15. The Z-scale for the single PE scan is given as the percentage of the number of counts above the pedestal threshold (PED + 2.5σ, where σ is the width of the Gaussian fit to the pedestal peak) and the Z-scale for the 60 PE level scan is the difference in the signal mean and pedestal mean in QDC bins. A 'dead' pixel (on the MAPMT, not electronics) along the top row is clearly visible in both scans. Individual pixel areas are visible in the single PE scan with some overlapping, whereas these features are not as easily distinguished in the 60 PE scans due to the increased response along the top and bottom rows. This may be due to the presence of the focusing electrode structure of the MAPMT. This is further discussed in Sec. 2.2.7.

Stepped Scan of MAPMT with GS20

A similar single PE scan was performed with the addition of the GS20 scintillator, providing an opportunity to observe if light scatters within the scintillator. The results are shown in Fig. 2.16 and are broadly similar to Fig. 2.13 with some pixels resolved to a better standard. The positions of the scanned data for single PE and 60 PE are verified in Fig. 2.17. The plot shows the output of the ADC channel exhibiting the strongest signal and the corresponding laser position. The relative X and Y-coordinates are the same as the millimetre scan data. The Z-axis colour corresponds to the ADC channel number (minus 100). The ADC channels begin at 100 and end at 163. Each ADC channel corresponds to a specific pixel number and a conversion table can be found in Table A.3. The position verification map matches the relative laser and pixel positions

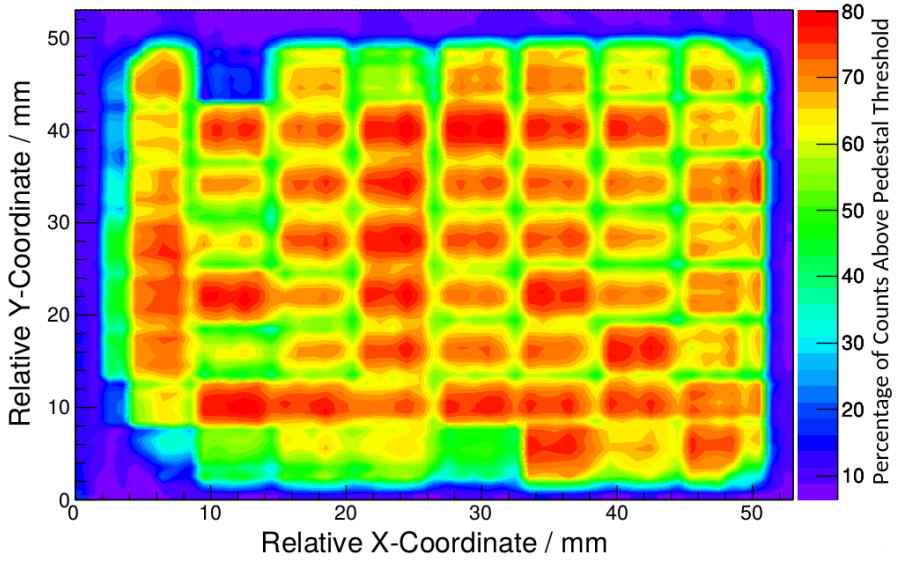

Figure 2.13: Single PE level mm step scan of the SoNDe Test Module without the GS20 scintillator. The Z-scale is the fraction of the number of counts above the pedestal threshold.

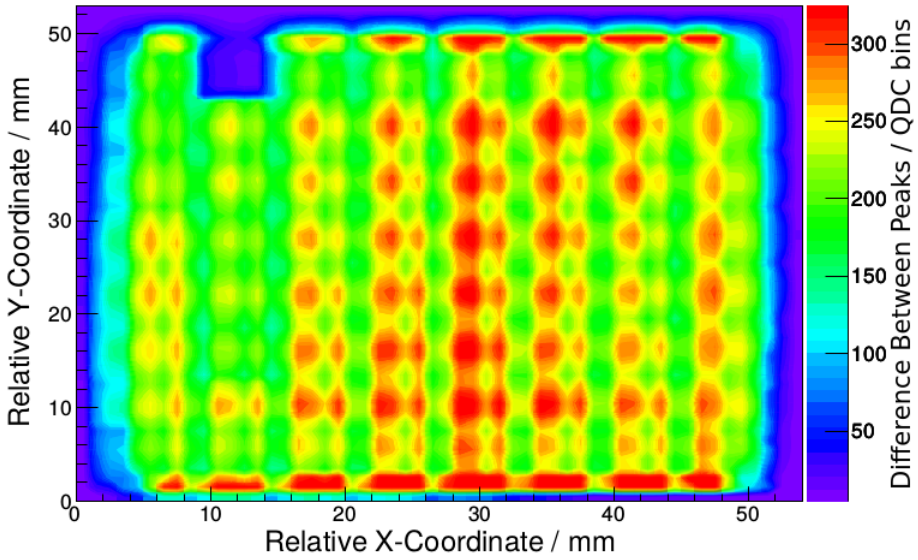

Figure 2.14: 60 PE level mm step scan of the SoNDe Test Module without the GS20 scintillator. The Z-scale is the difference between the signal peak and pedestal peak in QDC bins.

with some small areas of 'overlap' observed in the top two rows where the adjacent pixel has a stronger signal output at the pixel boundaries than the target pixel.

2.2.4 Gain Variation at Single PE

In order to compare the relative gains supplied by Hamamatsu (Fig. 2.4) to the gains one would expect at single PE level a similar gain map was produced. The laser was positioned at the

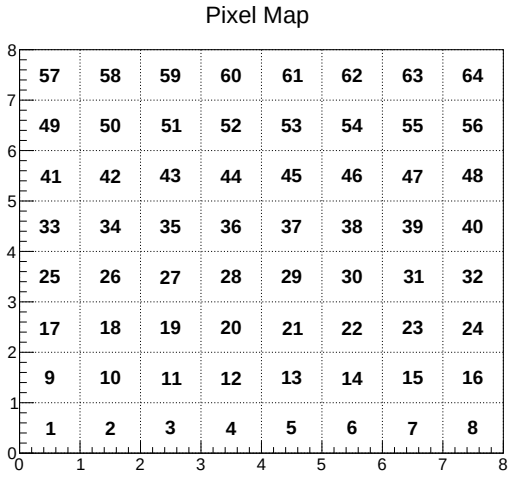

Figure 2.15: Pixel layout of scanned data for reference. With P1 located at the bottom left corner and P64 in the top right corner.

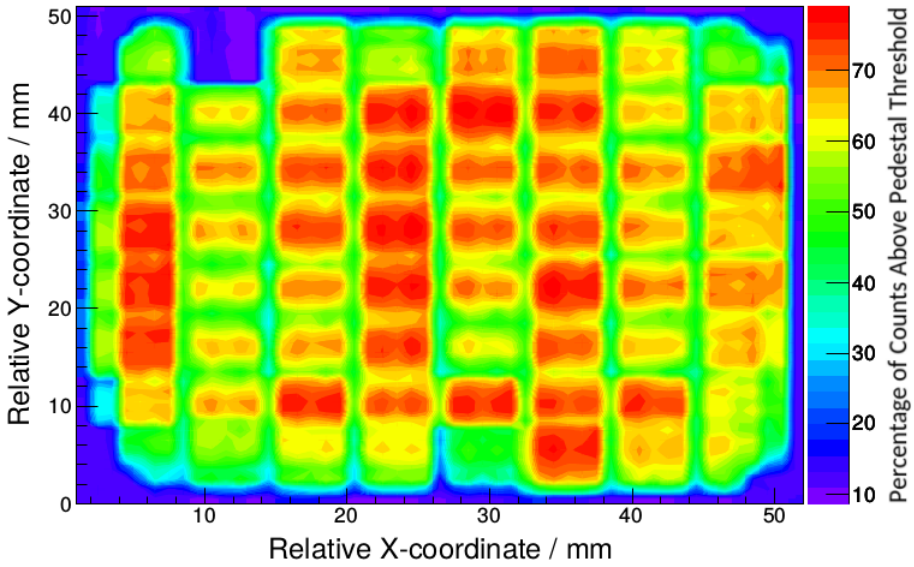

Figure 2.16: Single PE level mm step scan of the SoNDe Test Module with GS20 fitted. The Z-scale is the fraction of the number of counts above the pedestal threshold.

centre of each pixel for $\sim 10^4$ events for a MAPMT operated at -1000 V. The single PE peaks were fitted as before. The gain is defined as the difference between Q_1 and Q_0 (the single PE peak - pedestal peak). The gains were taken for all 64 channels as the ratio of a particular pixel gain to the highest pixel gain expressed in %. The results are shown in Fig. 2.18. The standard deviation of all gain values is $\sigma = 16\%$.

The gain map in general follows a similar trend to the specification given by Hamamatsu with lower gain pixels at the edges, and higher gain pixels tending to cluster together. The map shows a factor of ~ 3 maximum variation in gain, rather larger than the factor 2 specified by the

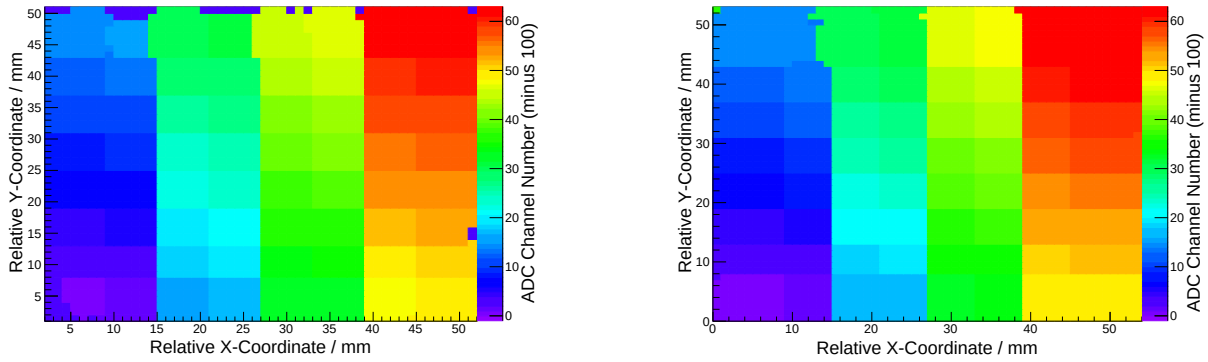

(a) (b)

Figure 2.17: (a) Single PE and (b) 60 PE position verification plots.

manufacturer. The relative gain varies from 32 to 100 and 58 out of 64 pixels conform to the Hamamatsu specification of factor 2 variation in gain. A number of pixels clearly have low gain. Obtaining a single PE fit is difficult as their distributions appear as a shoulder to their pedestal, so that the uncertainty in these gain values is relatively large.

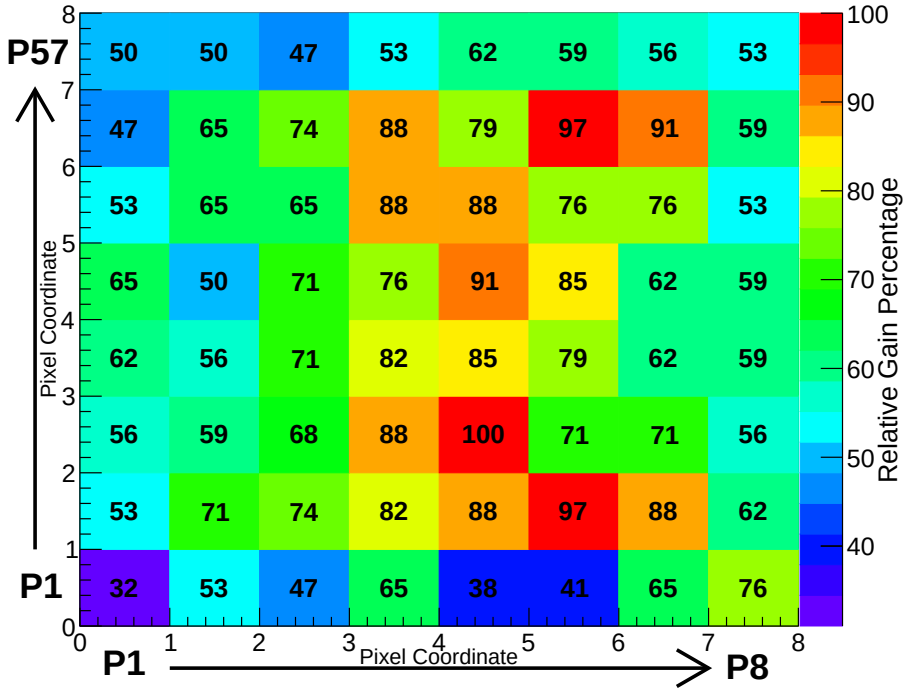

Figure 2.18: Relative gain map at single PE normalised to 100 for the pixel with the highest gain (Z-axis). High voltage = -1000 V and standard deviation across the pixels σ = 16%. The X and Y axes indicate the pixel location.

2.2.5 Diffuse Laser Illuminations

The laser beam spot illuminates only a 1 mm diameter circular area at the centre of each pixel. This does not give a fair representation of the response of each pixel in its entirety. A uniform response of the SoNDe Test Module was achieved by using the 404 nm laser and a Square Diffuser[4]. The projected square beam was made larger than the detector face. This was to ensure that the light drop off at the edge of the beam would not negatively affect the results of the pixels at the edge of the MAPMT. The extent of the light drop off at the edge/corner of the beam were studied using the CCD camera, and compared with the central position. As the CCD camera sensitivity is much lower than the MAPMT a higher light level had to be used. The setting used included: no neutral density filters, laser pulse amplitude = 75%, repetition rate = 60 MHz, pulse width = 35 ps.

Diffuse Blue Laser Characterisation with CCD

The CCD camera setup is shown in Fig. 2.19. The paper mask (centred on the CCD) indicated the size of the MAPMT face (inner square) and the beam was enlarged to the size of the outer square by adjusting the Z-stage distance of the detector from the laser. Measurements were taken at the centre, edge, and corner of the square profile to evaluate the extent of any drop off at the edges or any non-uniformity in the diffuse intensity profile. Fig. 2.20 shows a representation of the measurement taken at the edge of the area which represented the MAPMT face and the resultant image and intensity profile shown in Fig. 2.21.

The results of the data taken at each position produced a similar Gaussian like shape, a signature of a uniform distribution. Therefore, it was concluded that the diffuse square beam had an acceptable uniformity to carry out the full MAPMT illumination measurements.

Multi-Anode Photomultiplier Tube Characterisation with Diffuse Blue Laser

The uniform illuminations of the MAPMT face were performed at -1150 V. These measurements were taken before the addition of the FTA820A Octal Fast Timing Amplifier (Fig. 2.5 labelled 'A') and the increased HV used to compensate for a poor MAPMT output, therefore they cannot be directly compared to the -1000 V relative gain data. It was used to test the viability of relative gain characterisation using the diffuse laser and compare the response of all 64 pixels simultaneously. The advantage of this method being how rapidly it can be performed. The ESS will need a technique that is quick and reliable to characterise $\sim$ 400 of these detectors. The centre pixel scans performed with the 1 mm diameter laser may have experienced small amounts of drift due to the duration of time required to perform the scan (32 hours versus 30 minutes for single PE level with the uniform illumination). Thus, the gain recorded in the first pixel illuminated may appear artificially better/worse relative to the last pixel illuminated due to

[4]Thor Labs ED1-S20-MD Square Engineered Diffuser

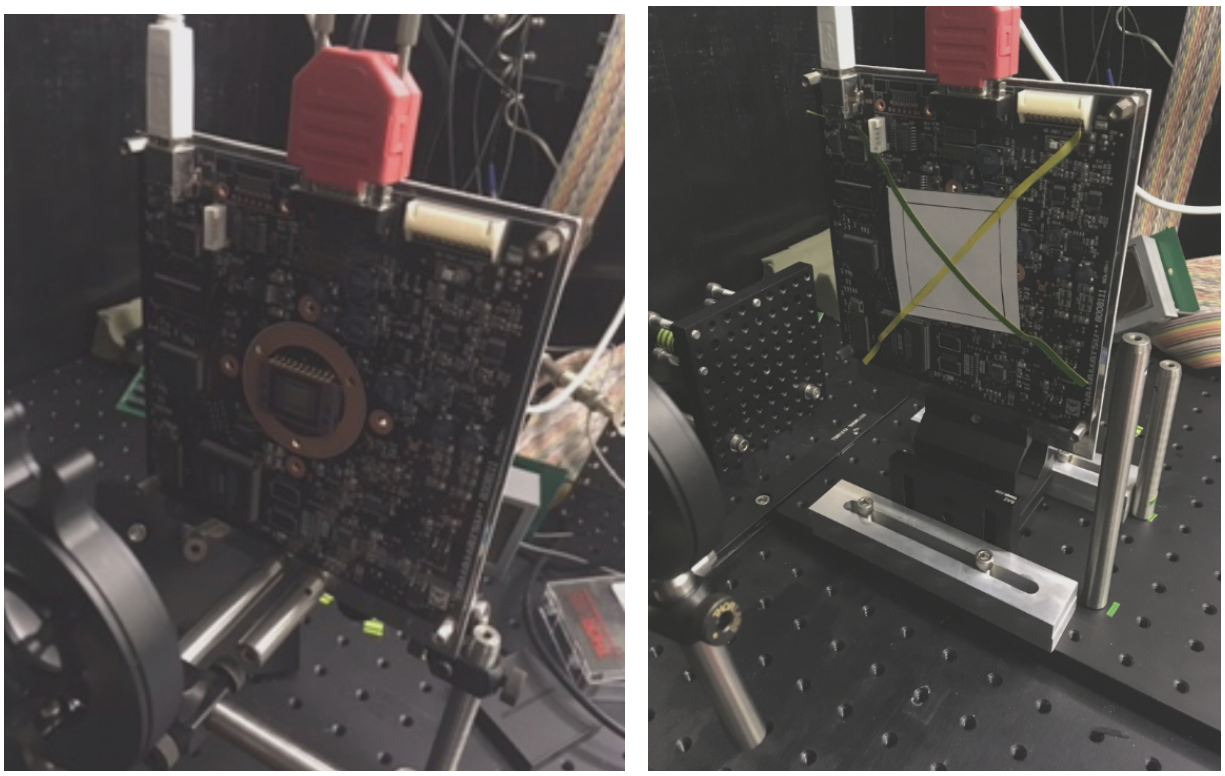

(a) (b)

Figure 2.19: (a) CCD camera placed in front of square diffuse laser beam. (b) The CCD camera covered with a paper mask indicating the size of the MAPMT face (inner square), and a larger square surrounding it as a size guide for the beam.

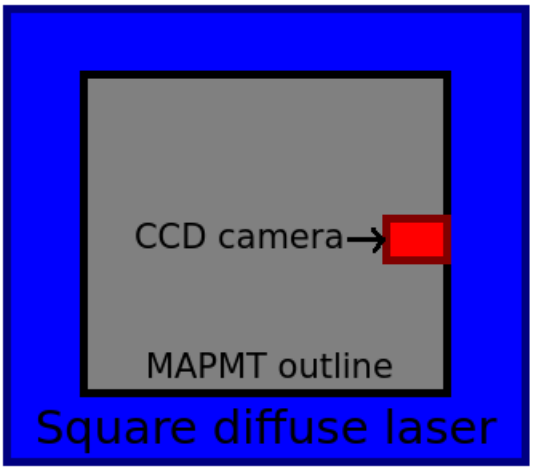

Figure 2.20: A representation of the CCD measurement taken at the edge of the area representing the MAPMT face.

the variations in drift (Fig. 2.11). Using the neutral density filters and adjustable amplitude of the laser, the single and 120 PE levels were found and their settings displayed in Table 2.2. A 120 PE level was chosen as this gave the cleanest result.

The variation in the mean PE level, μ, (from Eq. 2.4) at single PE light level was obtained

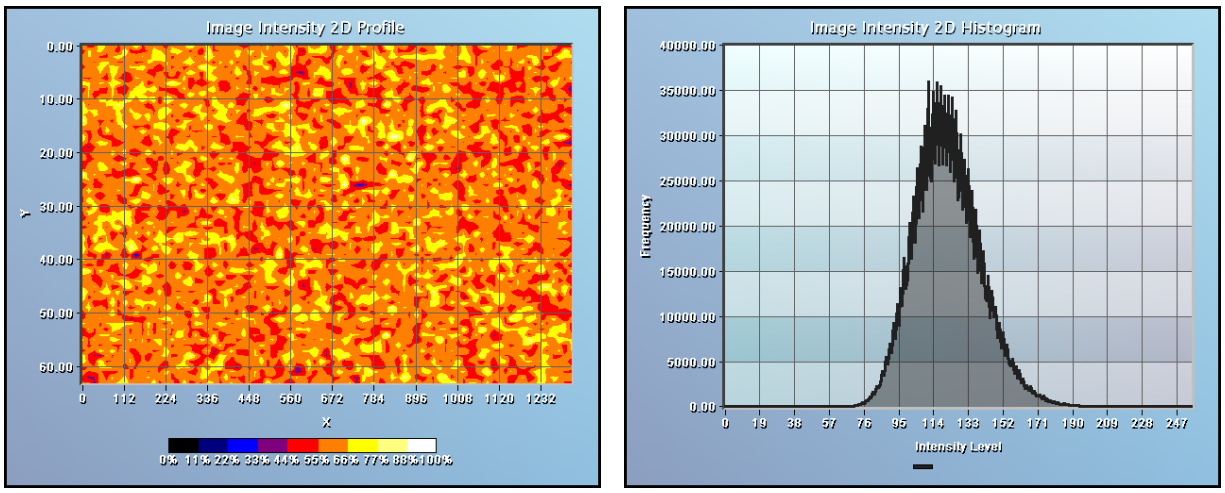

(a) (b)

Figure 2.21: (a) CCD image of the square laser beam projection. (b) the intensity profile of the square beam with a nearly uniform distribution.

Table 2.2: Blue laser settings for single and 120 PE levels for the square diffuse beam.

	Single PE	**120 PE**
Neutral Density Filters	3.0	0.0
Laser Pulse Amplitude	75%	25%
Laser Repetition Rate	600 Hz	600 Hz

and plotted for all 64 channels. The results are indicative of the relative gains of the pixels and are shown in Fig. 2.22 with the average μ value = 0.46 $\pm$ 0.01 and standard deviation σ = 0.087. As in the Hamamatsu relative gain map (Fig. 2.4), pixels 1 and 57 have the lowest gain/probability of a single PE event. Likewise there is a 'hot' region in the middle. Pixel P5 has the largest value of μ (0.65) and relative gain of 82%, compared to the highest gain pixel P54 with μ = 0.49. Fig. 2.23 shows the single PE fits for pixels 20 and 1 (relative gains of 89% and 50% respectively). There is a correlation between the probability of a single PE event and the gain of the pixel. Poor gain pixels tend to have an unresolved single PE peak which forms a shoulder with the pedestal peak. The gains of the poorer pixels are not ideal for single PE calibration purposes, and therefore if this type of detector is ever used at low PE levels or if the SKADI instrument scientists rely on using single photon measurements as absolute gain measurements a more reliable MAPMT with a ratio of anode output better than 1.0 : 2.0 would be required.

The variation in peak means for the 64 channels at 120 PE level are also indicative of relative pixel gains and are shown in Fig. 2.24. These relative gain maps produce: a standard deviation σ = 12% , a ratio of anode output 1.0 : 1.9, and 64/64 pixels conforming to the Hamamatsu 1.0 : 2.0 anode output ratio. These results are in close agreement with the Hamamatsu specification data. A similar trend with the higher gain pixels clustered towards the centre and lowest gain pixels at the corners is observed. The increase in HV may have an impact on the relative gain

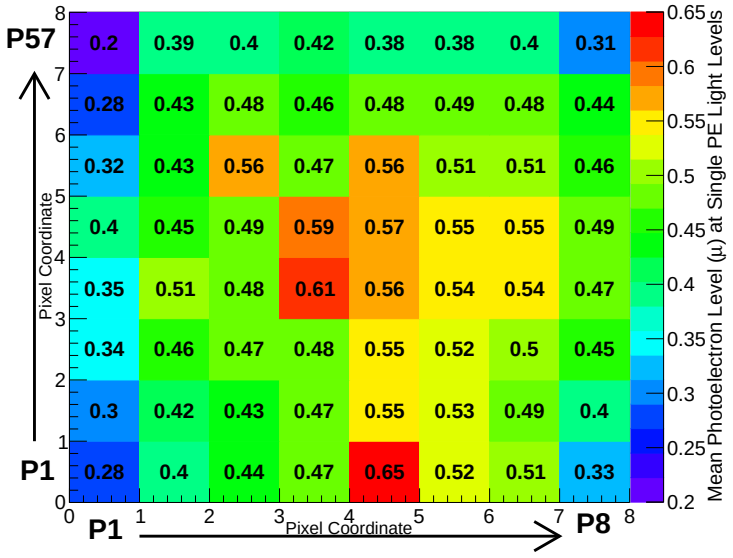

Figure 2.22: The mean PE level μ returned by the fit function variation across the 64 channels of a uniformly lit MAPMT at single PE light level. The X and Y axes are given as the pixel coordinates and the Z-axis as the probability of a single PE event.

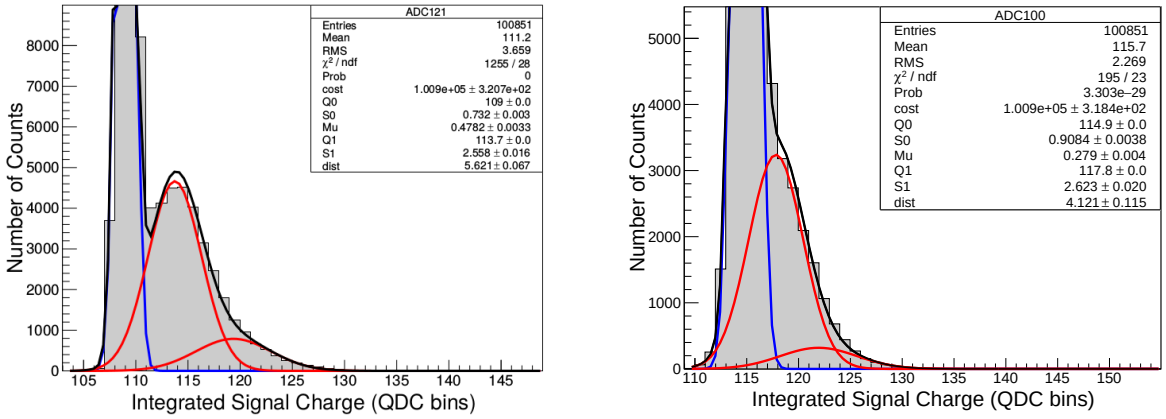

(a) (b)

Figure 2.23: The single PE fits for pixels 20 (a) and 1 (b). The μ values were 0.48 and 0.28, corresponding to pixel gains of 89 and 50 respectively. The second red peak corresponds to the 2 PE peak contributions. Absolute gains of pixels 20 and 1 are 2.94×10^6 and 1.81×10^6 respectively. For pixel 20, $Q_0 = 109.27 \pm 0.06$ and $Q_1 = 113.71 \pm 0.09$. For pixel 1, $Q_0 = 114.90 \pm 0.05$ and $Q_1 = 117.82 \pm 0.08$.

variation as the current multiplication may not increase uniformly, pixel to pixel, with increasing supply voltage [78]. Four pixels have a maximum gain of 100% (gains rounded to the nearest whole number), and twice as many pixels have a relative gain ≥ 90. The results at a higher light level and increased HV gives a strong indication that this method of simultaneous illumination could be used for rapid gain characterisation.

These methods of gain characterisation show promising results at both single and 120 PE

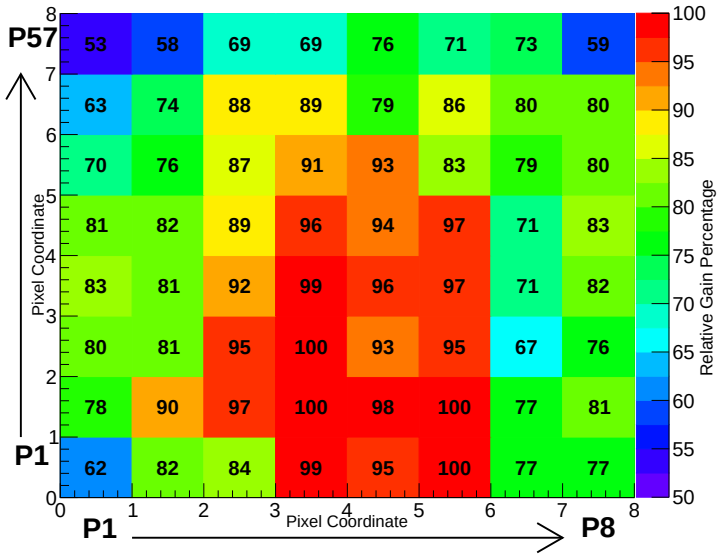

Figure 2.24: The relative gains of the 64 pixels at 120 PE levels with standard deviation σ = 12%, anode output ratio 1.0 : 1.9, and 64/64 pixels conforming to the Hamamatsu 1.0 : 2.0 ratio. The X and Y axes are given as the pixel coordinates and the Z-axis as the relative gain percentage.

levels. It would be recommended when characterising each individual detector that the MAPMT be run at a HV which is high enough to resolve a decent signal, but not too high that it will age the MAPMT. The present MAPMT has a lower absolute gain in comparison to similar detectors (Fig. A.1) and would likely be operated at a higher HV than those of a higher gain, hence why it is necessary to measure it at various HV settings to find which is most effective.

2.2.6 Crosstalk Measurements

Incident light spread within the GS20 sheet and borosilicate glass window of the MAPMT contributes to the greatest amount of crosstalk for the SoNDe detector. As previously mentioned in Sec. 2.1.2, crosstalk affects the accuracy of position reconstruction. If light/radiation is incident on the detector at a certain position is it detected and readout at the relevant anode(s)? 'Electron leakage' between the dynode chains (electron multiplication stages) has been identified [78] as the main source of crosstalk for MAPMT's. A photoelectron or secondary electron multiplied in the dynode chains deviates towards a neighbouring dynode chain and is amplified there, creating a signal in the 'wrong' pixel.

Electron leakage is only effective if the stray photoelectron hits the first dynode within the neighbouring chain. A stray electron originating from dynodes further down the chain (dynode > 1) will produce a very small contribution [105] due to reduced amplification and will be lost in the noise. 'Collection efficiency' is the probability that a photoelectron will fall upon the effective area of the first dynode in the chain. This is affected by the potential difference

between the cathode and first dynode. At least 100 V should separate these structures for good electron collection efficiency. A sharp pulse of current through a MAPMT can cause an upset on the applied bias voltage at the dynodes, which may induce spurious signals in other pixels. Stray capacitance between the anode pins of adjacent pixels is a further source of crosstalk. The electronics used to read out the signal from the MAPMT will contribute to a small amount of crosstalk due to the proximity of adjacent channel cabling (pickup) e.g. at the input of the QDC modules.

The GS20 scintillator is 'dry-fitted' to the MAPMT, i.e. uses no optical coupling interface. The dry fit leads to a thin layer of air between these materials. The change in refractive indices from GS20 (n = 1.55) to air (n = 1.0) and finally to borosilicate glass (n = 1.53) will cause multiple internal reflections within the GS20 and at the borosilicate window. Only photons close to perpendicular will be refracted through. The addition of a coupling agent, e.g. epoxy, does aid the transmission of a larger number of photon angles and therefore more light. However, the increased range of angles means a more spread out signal with increased optical crosstalk.

When a neutron capture occurs within the GS20 scintillation glass the secondary particles (α and ^{3}H) have a range around tens of μm. The light produced from this is isotropic and has a peak emission absorption length of $\lambda \sim 20$ cm (absorption coefficient ~ 0.05 cm^{-1} at 1.5 mm glass thickness [106]), meaning there may be a contribution to crosstalk from the light produced within the scintillator.

The Hamamatsu setup to measure crosstalk is shown in Fig. 2.25. The distance from the scintillating fibre and MAPMT may be varied, with the lowest crosstalk across pixels achieved when the fibre was placed flush with the detector face.

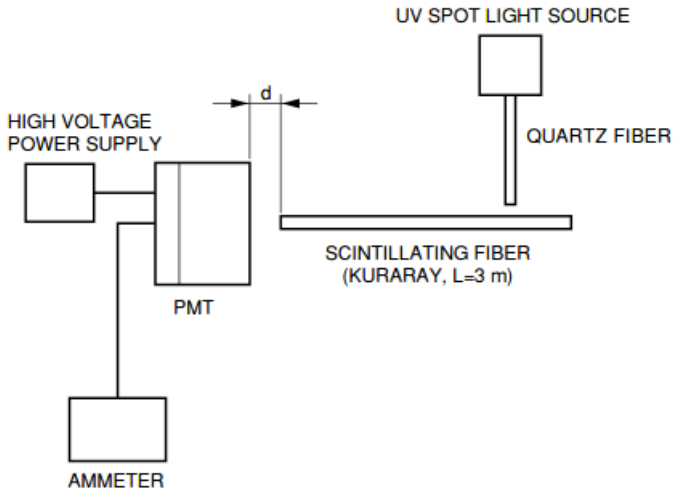

Figure 2.25: Crosstalk measurement setup used by Hamamatsu to test multi-anode photomultiplier tubes. Image taken from [78]

Results obtained by Hamamatsu for a 1 mm diameter optical fibre placed at 0.0 mm from a generic H12700 MAPMT detector face are shown in Fig. 2.26. The output of each neighbour

pixel is expressed as a percentage relative to the 'target' pixel.

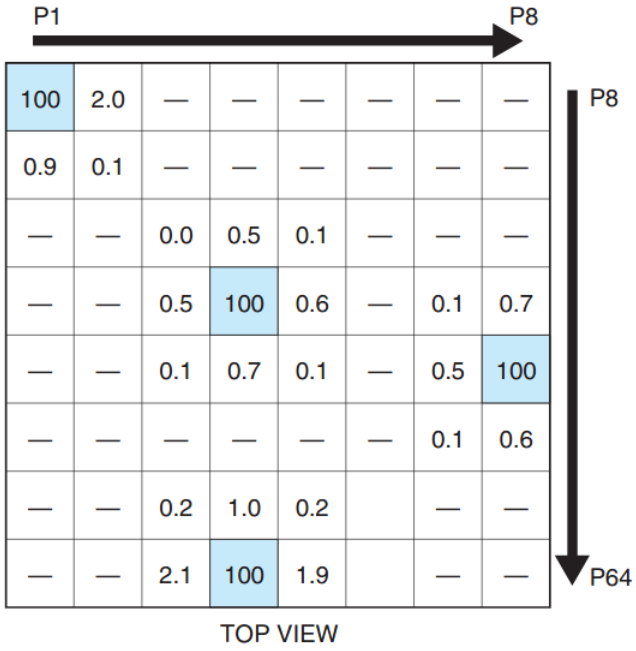

Figure 2.26: Hamamatsu crosstalk measurement for a typical MAPMT. Taken from [83]

The circuit shown in Fig. 2.5 was used for the present set of measurements. The MAPMT was placed at 65 mm from the laser beam to produce a clean 1 mm diameter spot. No optical fibre was used between the laser and MAPMT due to non-availability of suitable equipment. One of the issues with carrying out the measurements in this way is light dispersion from the laser head. To mitigate this issue a mask was made for the detector with a 1.5×1.5 mm^2 square hole at placed the centre of the target pixel to eliminate any beam halo effects.

The crosstalk measurements were performed at a light level of 60 PE. The crosstalk is calculated as a percentage using the following equation,

$$\text{Crosstalk} = \frac{S_x - P_x}{S_0 - P_0} \times 100 \tag{2.11}$$

where S_x is the mean of the neighbouring signal distribution, P_x is the mean of the neighbouring pedestal signal, S_0 is the mean of the target signal distribution, and P_0 is the mean of the target pedestal signal. The mean of each signal was calculated by fitting a Gaussian distribution. Fig. 2.27 shows the signal (red) and pedestal (blue) for the target pixel P45 (left) and for a neighbouring pixel P46 (right). The results given as a percentage for four individual pixels (8, 25, 45, and 59) are shown in Fig. 2.28. The results give slightly increased crosstalk in comparison to the Hamamatsu measurement. This may be due to the differences in electronics used, the setup/method, the spot diameter, and beam divergence of the laser light. The crosstalk measured here is a convolution of optical dispersion, electron leakage, collection efficiency, stray capacitance and pickup. It would be difficult to disentangle and quantify the crosstalk contributions

without taking the detector apart and measuring the current at various stages throughout the device. For a vacuum tube this is obviously impossible.

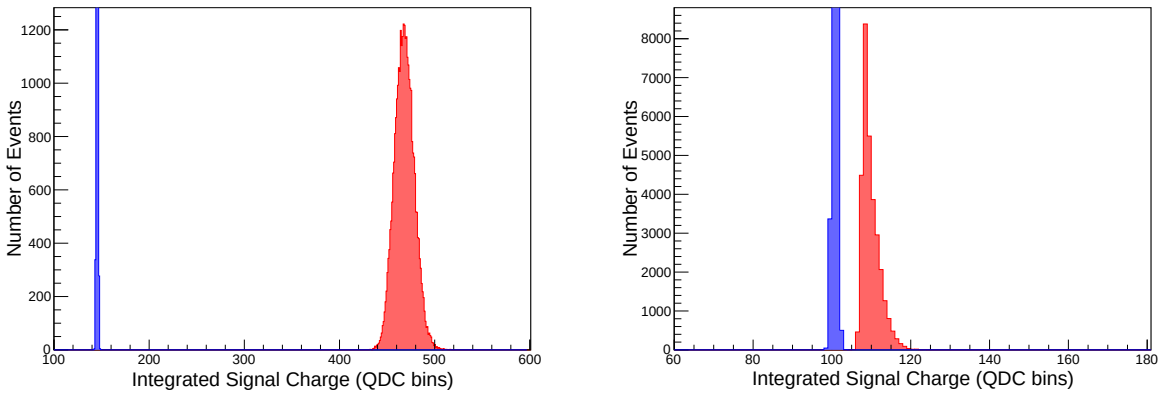

(a) (b)

Figure 2.27: (a) The laser signal (red) in the target pixel P45 with the pedestal signal (blue). (b) Crosstalk signal (red) in the neighbouring pixel P46 with corresponding pedestal signal (blue). Note the different X-axes ranges in the plots.

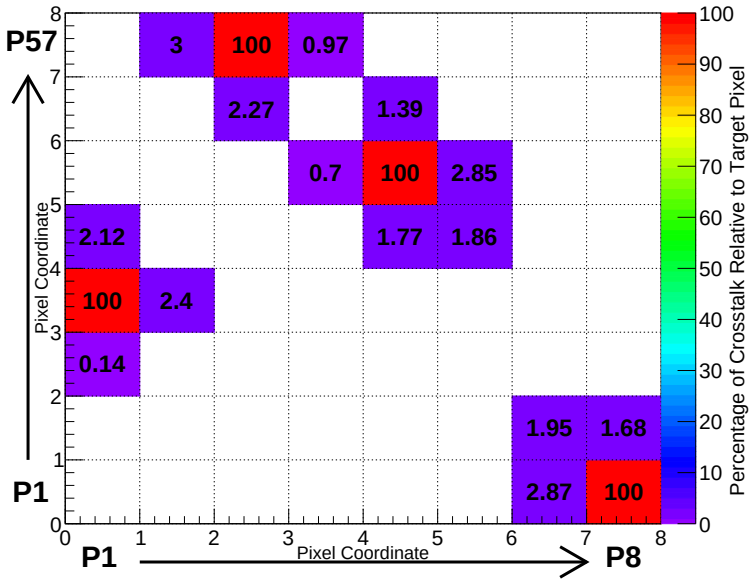

Figure 2.28: Measured crosstalk values for pixels 8, 25, 45, and 59. The MAPMT was masked and the laser head was positioned 65 mm away with an incident spot diameter of 1 mm, and a 60 PE light level.

2.2.7 Cross-Pixel Scans

Light spreading within the GS20 scintillator and borosilicate glass window of the MAPMT results in optical crosstalk. The 1 mm diameter laser beam spot was scanned from the centre of P45 to its horizontal, vertical, and diagonal neighbours as shown in Fig. 2.29. Pixel 45 was chosen due to it's high gain (measured as 90/100 from the anode uniformity test sheet by Hamamatsu in Fig. 2.4) and similarly high gain surrounding pixels. A black vinyl mask with 0.5 mm diameter holes spaced 1 mm apart was made to shield the MAPMT from stray laser light and any possible halo effects (Sec. 2.2.2). The scanned results for the masked MAPMT are plotted as the mean number of photons against their relative position. Differences in the relative gains between pixels are normalised and accounted for. Measured and simulated results for the scans are shown below. Further information regarding the simulation setup is provided in Sec. 3.1.

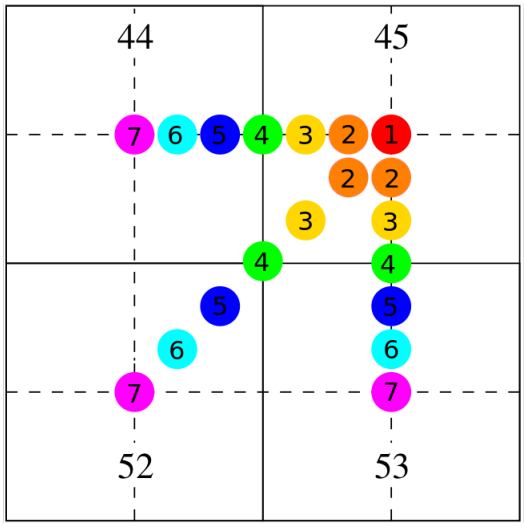

Figure 2.29: The mm scan positions beginning at the centre of P45 (position 1, red) and finishing at the centre of the neighbouring pixels (position 7, magenta).The intersection point of pixels 44, 45, 52 and 53 is taken as the origin of the X, Y coordinate system.

The results for a horizontal scan with/without the addition of GS20 are shown in Fig. 2.30. A slight offset from the centre of the pixel (i.e. where the red and blue lines intersect the boundary and the number of photons detected in each pixel is assumed to be the same) is visible in Fig. 2.30a. An offset of -0.07 mm from the nominal measurement positions was factored into the simulation. The summed values from the measured data show an oscillating position dependence while the simulated distribution is very flat. This may be due to the structural make-up of the MAPMT pixels. The dynode chains that are used to collect and multiply the photoelectrons have four vertical slits/openings per pixel. A close-up view of these slits is shown in Fig. 2.31. The height of the slits varies, with at least one in every four being shorter (Fig. 2.32). A study performed by M. Contalbrigo *et al.* [107] found a reduction in the normalised signal efficiency (fraction of counts above pedestal threshold) for the H12700A when scanning across dynode slit

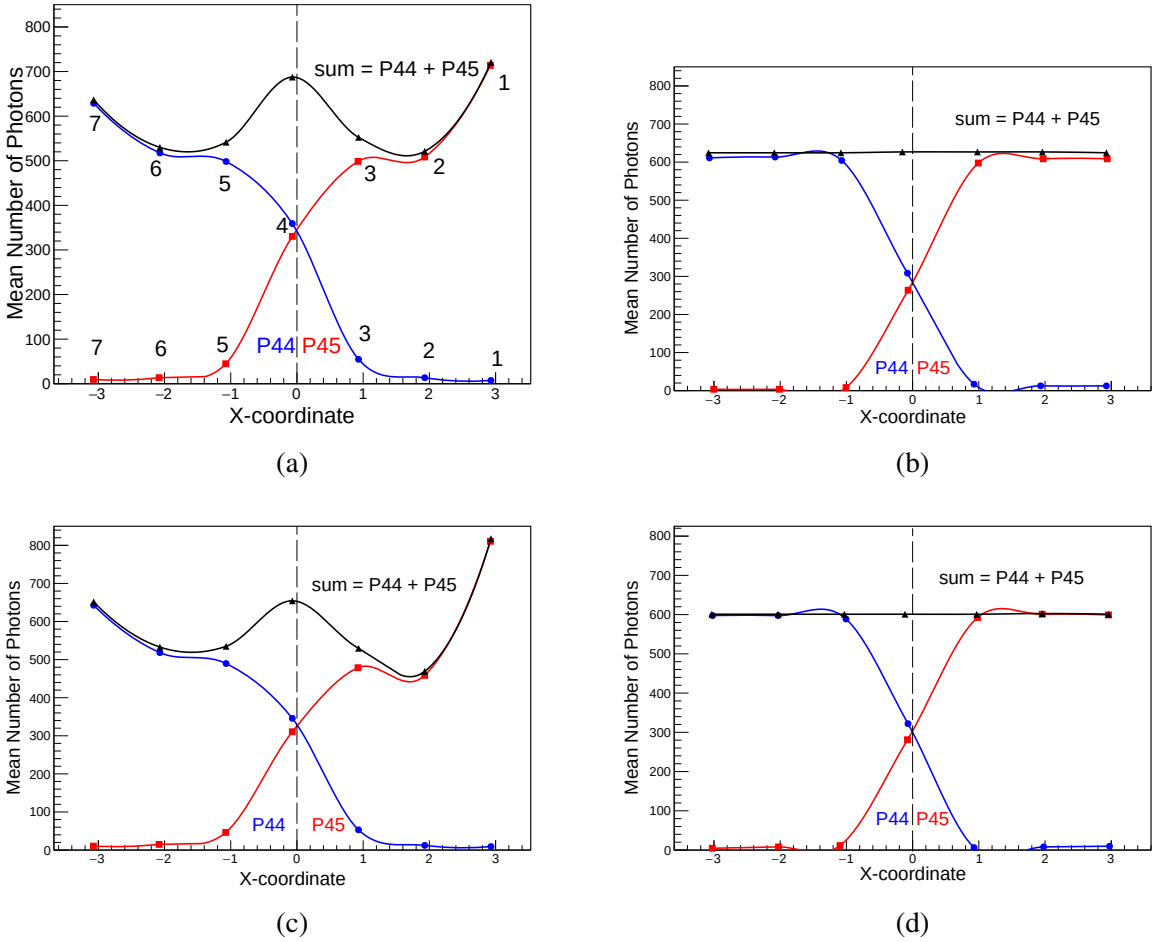

Figure 2.30: (a) Measured horizontal millimetre scan of MAPMT (no GS20) with a blue laser. (b) Corresponding simulated scan. (c) Measured horizontal millimetre scan of MAPMT+GS20. (d) Corresponding simulated scan. The black dashed line indicates the pixel boundary with data from P44 shown in blue and P45 in red. The sum of the mean number of photons for both pixels at each position is represented by a solid black line.

entrances. The results are shown in Fig. 2.33. One hypothesis is that the 'dip' at 2 and 6 may be due to the laser light falling between two slit entrances. The active area of the pixels along the top and bottom rows (Fig. 2.31b) is also decreased by horizontal support components which are part of the focusing electrode. These components may be the cause of the anomalies seen in the top and bottom row of the 60 PE mm scan in Fig. 2.14.

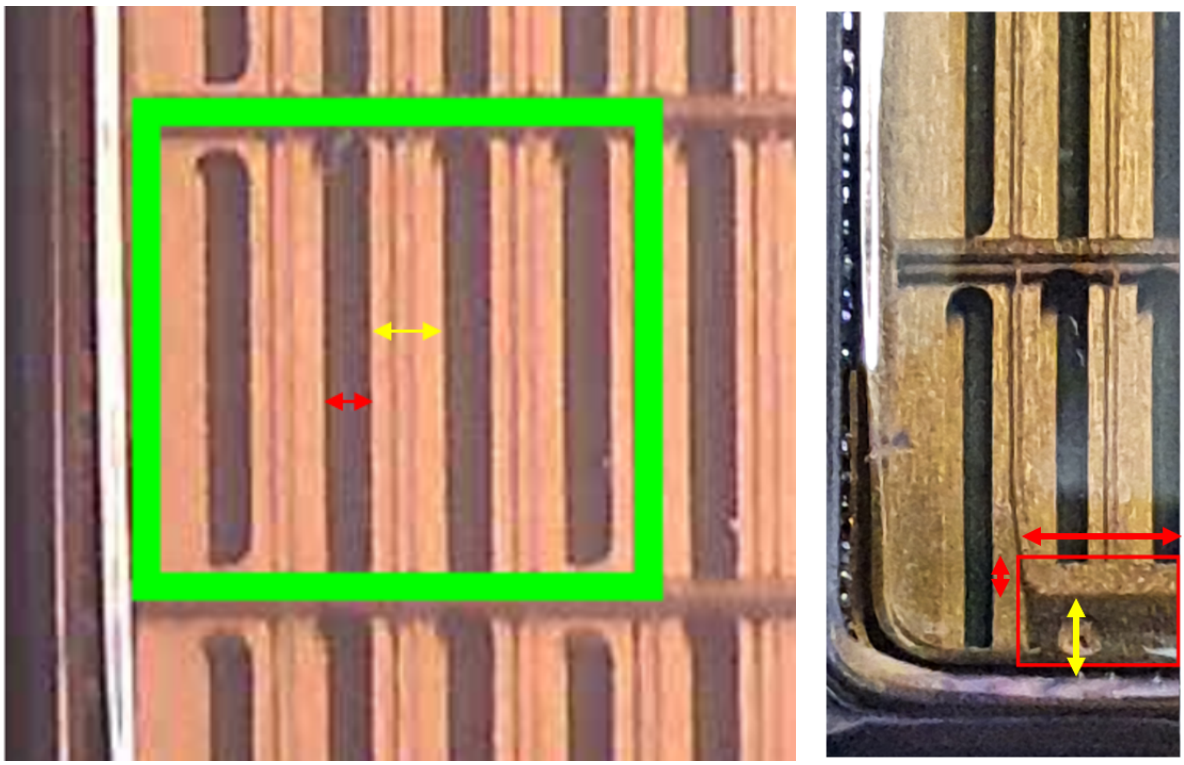

(a) (b)

Figure 2.31: An enhanced view of the H12700A MAPMT detector face. (a) The vertical slits are the entrances to the dynode chains of each pixel with four entrances per pixel highlighted by the green square. The opening of each aperture is ~ 0.7 mm (red arrow) and the space between each aperture measures ~ 0.8 mm (yellow arrow). The height of the entrance slit varies subtly across the active area. Figure (b) shows the bottom left corner of the detector, with part of the focusing electrode obstructing the dynode entrance slit (red rectangle). The yellow arrow measures ~ 1.28 mm and the red arrows measure ~ 0.5 mm and ~ 43 mm (extending across the length of the bottom and top row of the MAPMT.)

The summed data points for the vertical scan (Fig. 2.34) are similar to those of the horizontal scan at positions 2 - 6 but at positions 1 and 7 the vertical shows significantly less intensity. An offset of +0.13 mm was calculated for the vertically scanned data. The intensity near the pixel border is more pronounced in comparison to the response at the centres of pixels 45 and 53. This effect may have been a result of the laser falling at the centre of the pixels between two dynode slits. Although the vertical borders, seen clearly in Fig. 2.31, appear more robust than the seamless horizontal borders, the electrostatics of the device will still focus the photoelectrons into the dynode chains. There will however be a drop in collection efficiency at the borders, more so in the horizontal direction than the vertical according to Fig. 2.33. This behaviour within the substructure of the pixels was not included in the simulation. Up to this point the simulated results tend to predict a uniform response across the seven scan positions. The measured and simulated diagonal results (Fig. 2.35) agree that the least light is collected at the four pixel boundary (the point where the four pixels meet). Assuming that the simulation models the transport of optical

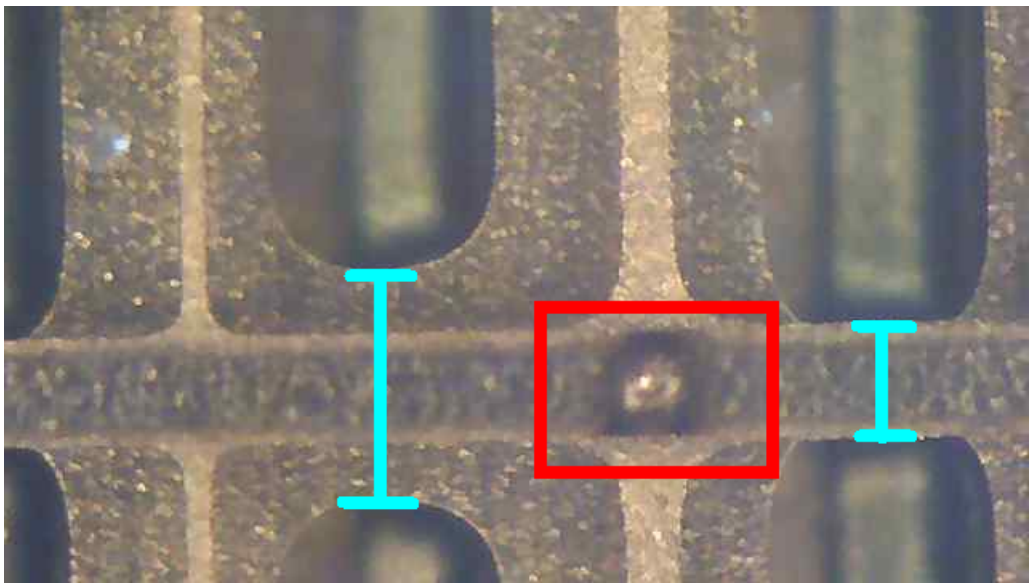

Figure 2.32: Close-up image of a welding point of the focusing electrode layers at an intersection point between four pixels (red). The variation in dynode aperture heights highlighted in cyan measure ~ 0.3 mm and ~ 0.8 mm.

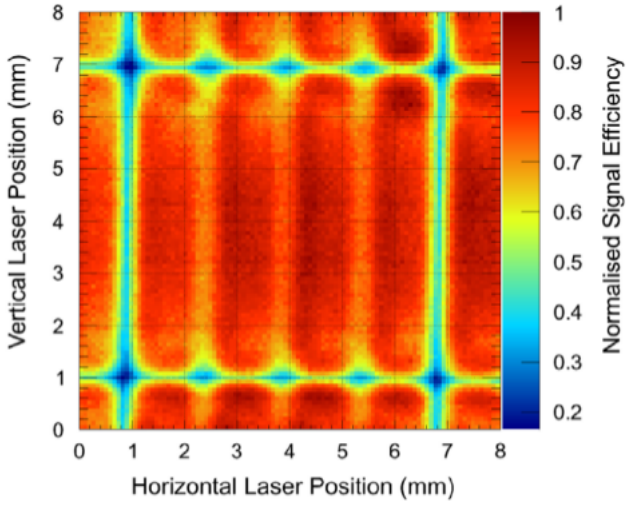

Figure 2.33: An 8×8 mm^2 scan of an H12700 pixel using a 635 nm wavelength pico-second pulsed laser beam with spot diameter 90 μm and step size 80 μm. The origin position of this μm scan differs from the mm scans in Fig. 2.30 etc. with their origin taken from Fig. 2.29. Image taken from [107]

photons reasonably accurately, the differences between the model predictions and measurements can pinpoint possible structural effects in the MAPMT. The simulation will be extended to investigate this more quantitatively. Again Fig. 2.33 shows the lowest signal efficiency at the four pixel border. This 'deadspace' corresponds to the welding point support structure shown in Fig. 2.32. The extent of light sharing at the boundaries and effect of deadspaces would need further investigation as to its implications on the SoNDe detector's ability to distinguish thermal neutron capture events and preventing optical crosstalk where possible. Optical crosstalk is further

investigated in Sec. 3.1.2.

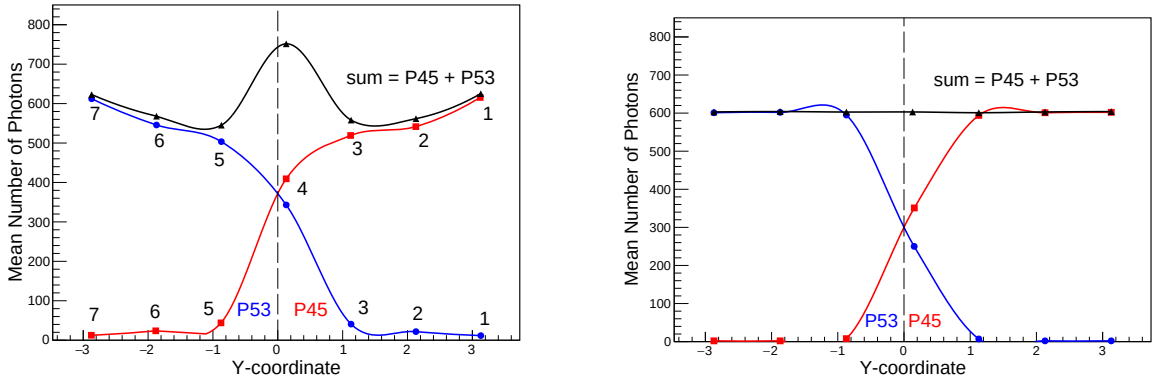

(a) (b)

Figure 2.34: (a) Measured vertical millimetre scan of MAPMT (no GS20) with blue laser. (b) Corresponding simulated scan. Similar to the horizontal scan, the vertical scan shows an increased response at the pixel boundaries.

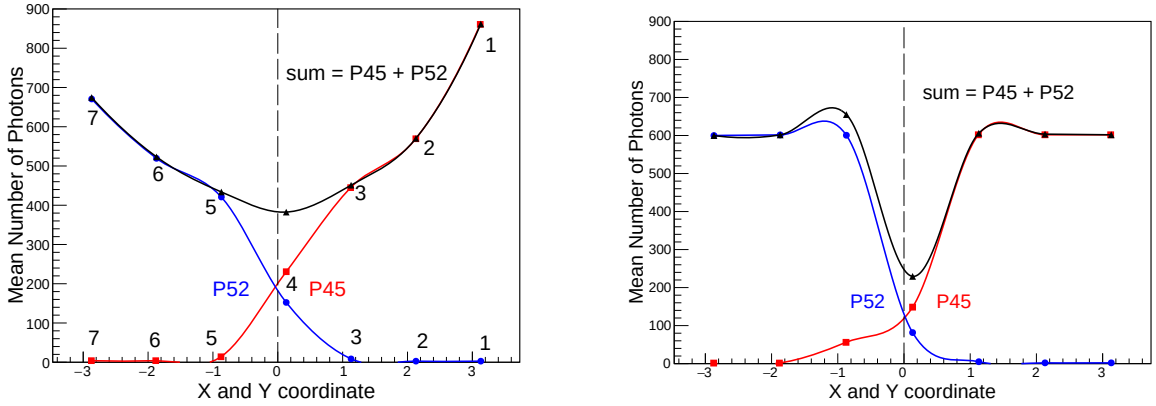

(a) (b)

Figure 2.35: (a) Measured diagonal millimetre scan of MAPMT (no GS20) with blue laser. (b) Corresponding simulated scan. At position (0,0) the light should be equally shared by 4 pixels so the sum of only 2 pixels shows a minimum.

2.3 Summary

The individual components that form the SoNDe Test Module (GS20 + H12700 MAPMT + VME based DAQ) were investigated. The Test Module was illuminated using a 404 nm laser, which itself was characterised using a CCD camera. The focal point of the laser occurred at a distance of 56.5 mm from the MAPMT where the spot diameter was 0.284 mm $\pm$ 0.013 mm. The distance for a laser spot of 1 mm diameter was 65.73 mm $\pm$ 0.01 mm. The CCD camera revealed some non-uniformities in the laser intensity distribution, as well as a small halo surrounding the beam at certain distances. The contribution of these factors were considered to have little to no impact on the measurements. A stability test (Fig. 2.11) performed using a 404 nm laser over a 34 hour period for a 'cold start' MAPMT had a drift of 1.15×10^{-4} %/hr. Over the 34 hr period the mean QDC channel of the pulse-height spectrum dropped from $\sim$ 470 to $\sim$ 464. A 30 - 60 minute warm up period for the SoNDe modules would be recommended before recording SANS data with the SKADI instrument.

The incident laser intensity for single photoelectron production at the cathode were established through an analysis of the MAPMT pulse height spectrum. The fit function may have been more effective had a number of free parameters been constrained. The pedestal measurements could have been carried out separately and fixed. This would have reduced the uncertainty in the overall fit. Laser scans in 1 mm steps (Figs.2.13, 2.14, and 2.16) at single and 60 PE levels revealed significant non-uniformities. The mechanical structure of the device does affect the uniformity but not to an extent that is an issue for the SoNDe application. A relative gain map at single PE level (Fig. 2.18) for the 64 pixels at -1000 V had a lower relative gain per pixel compared to the gain map provided by Hamamatsu (Fig. 2.4). It shows a ratio of anode output = 1.0 : 3.1, and a standard deviation of 16%, both larger than the ratio and standard deviation of the gains provided by Hamamatsu, 1.0 : 2.0 and 11% respectively. This is due to the low gain of the MAPMT and its inability to properly resolve the single PE peak. In similar tests (sections 4.3.3 and 5.6) this particular MAPMT performed well, so that for this test a higher HV setting may have been more suitable.

The uniform square beam illuminations of the SoNDe Test Module showed a slight variation in the μ values at single PE level (Fig. 2.22), indicative of a near-uniform square beam. The average μ = 0.459 $\pm$ 0.01 with standard deviation = 0.087. This in turn showed a correlation between μ and pixel gain, indicating that the gains of this particular MAPMT are relatively low. The method of full detector illumination at single PE level and comparing the μ values could be used to characterise the relative gains of the MAPMTs that form the SKADI detector. The 120 PE illumination results showed good correlation to the Hamamatsu data (σ = 12% and 1.0 : 1.9 ratio of anode output), with the main characteristics of low gain corner/edge pixels and high gain central pixels observed.

The measured crosstalk values for pixels 8, 25, 45, and 59 were found by comparing the ratio of the difference between the signal mean and pedestal mean for the neighbouring and

target pixels. The crosstalk range was found to lie between 0.14 - 3.0%, slightly greater than the data provided by Hamamatsu. It confirms that the H12700A MAPMTs are low crosstalk devices and ideal for this application.

The cross-pixel scans show a significant formation in the position dependence of the signal amplitude, which are not reproduced by the simulation. It is possible that this formation results from the structure of the entrance slits to the dynode chain. The vertically scanned data showed the largest light output near the P45 and P53 pixel border as opposed to the centres of the pixels. This may have been due to light incident at the 'centre' of pixels 45 and 53 falling between two dynode slits, decreasing the number of detected photons. The photoelectrons at the boundary are focused into the dynode chains due to the potential difference between the photocathode and the first dynode. The diagonal scan results showed a gradual decrease in light as the laser spot moved further from the pixel centre. The corresponding simulated data showed a 75% reduction in the number of photons detected by P45 at the boundary intersection between the four pixels. The effects of the dynode slits and MAPMT structures were not taken into account by the simulation, however the differences between the measured and simulated results highlights the degree to which their presence affects the signal variation.

The SoNDe Test Module had been extensively characterised using laser light, the next stage was to investigate altering the detector design and the effects this has on its response via Geant4 simulation. This is explored in Chapter 3.

Chapter 3

Geant4 Based Simulations

Geant4 [3] (GEometry-ANd-Tracking) is a Monte Carlo simulation package used to track particle interactions through matter for applications in accelerator and nuclear physics, high energy particle physics, nuclear medical, and space science. In this research Geant4 is used to simulate the response of the front end of the SoNDe module to various forms of radiation, including: optical photons, collimated beams of alpha-particles [108], protons [109], and uncollimated thermal-neutron, fast-neutron, and gamma-radiation sources. Electron sources have not been included in the study, but gamma-rays will produce secondary electrons. The SKADI instrument will experience a background radiation field of gamma-rays and fast neutrons, therefore it is important to simulate these. The simulation is directly compared to the measured data shown in later chapters, and (after successful verification) used to explore potential detector alterations to optimise the SoNDe module, e.g. a pixellated scintillator. The simulation may be operated in different modes:

1. Optical transport only. Photons were tracked at a wavelength of 395 nm.
2. Interactions of ionising radiation only, recording energy losses, times and interaction positions.
3. Interactions of ionising radiation, producing scintillation photons which are subsequently tracked. Photon wavelength followed the scintillation emission spectrum, which peaks at 395 nm.

The transport of optical photons (mode 1) is covered in this chapter, while full simulation of the detector response to alpha particles, protons, neutrons and gamma-rays is compared to measurements in Sections 4.4.2, 6.3 and 5.4 respectively.

3.1 Geant4 Based Optical Simulation

The Geant4 based optical simulation written by John Annand [110] was created to, gain a better understanding of light scattering within the GS20, explore possible scintillator glass configu-

rations/modifications, and test whether optical couplings between the scintillator and MAPMT would increase detection efficiency. The simulation uses the Geant4 Monte Carlo toolkit, version 4.10.6 [3]and is coded in C++. The optical simulation includes the following features:

1. An isotropic General Particle Source of optical photons with wavelength $\sim$ 395 nm (3.145 eV) (peak emission wavelength of GS20 scintillator) generated at a determined position in the scintillator using the Geant4 toolkit.

2. A ^{6}Li-doped glass scintillator (GS20, composition described in Sec. 2.1.1) with active area dimensions 50.0 $\times$ 50.0 $\times$ 1.0 mm^3, a peak emission absorption length $\lambda \sim 12$ cm, matching the scintillator piece that will be used at ESS by the SKADI instrument group. The default scintillator setting is a flat/plain sheet of glass. However the scintillator optionally may be pixellated into an 8 $\times$ 8 array (along pixel boundaries) by etching grooves into the glass surface and its thickness, groove depth and width can all be varied. The default scintillator glass finish is polished, however a polished Al, matt Al, and matt TiO_2 external reflector may be applied to the front face and grooves of the GS20 sheet.

3. A silicone rubber optical interface pad or optical epoxy based on Eljen Technology EJ-560 [111] and EJ-500 [112] respectively may be inserted optionally to study the effect on photon transport from the GS20 to the glass window of the MAPMT. The thickness of the coupling film is an input parameter. The default setting is no coupling medium, i.e. an air-gap of 0.08 mm which is due to a slight concavity in the borosilicate glass. Of the 35 MAPMTs measured the average depression was 0.08 mm (σ = 0.02 mm).

4. A borosilicate glass window measuring 52.0 $\times$ 52.0 $\times$ 1.5 mm^3 taken from the specification sheet of the H12700A MAPMT. A layer of bialkali photocathode measuring 48.5 $\times$ 48.5 mm^2 is deposited on the back side of the glass window. The quantum efficiency of the photocathode may optionally be made position sensitive with dips along the boundaries between pixels (Fig.3.1). Possible non-uniformity within a pixel has not been modelled. The internal electrode structures, such as the dynode chains were not included in the simulation.

The optical simulation was used to determine the degree of light spreading away from its production point for a variety of SoNDe module configurations. Parameters such as a pixellated GS20 scintillator, optical coupling between scintillator and borosilicate glass, and reflective coatings for the scintillator were studied in a variety of combinations.

3.1.1 Optical Properties and Photon Transport

The optical properties of each material were modelled in the simulation from information provided by the manufacturers. All optical simulations were performed at the GS20 peak emission

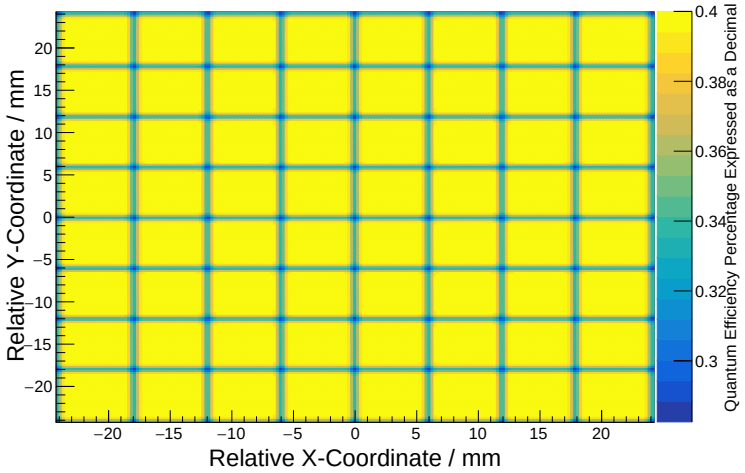

Figure 3.1: The quantum efficiency map of the simulated bialkali photocathode with X and Y axes units in mm, and an origin point at the centre. The Z-scale is derived from the approximate quantum efficiency provided by Hamamatsu [83], expressed as a decimal.

wavelength, λ = 395 nm. The scintillator coatings were chosen for their high reflectivity at the GS20 emission peak (395 nm). A commonly used matt TiO_2 paint (EJ-510 produced by Eljen) gives a (diffuse/Lambertian) reflectivity of 90% at 395nm [113], polished aluminium gives (specular) reflection of $\sim$ 92% at 395 nm with a small wavelength dependence [114] [115], and ground aluminium (diffuse/Lambertian) reflection of $\sim$ 70% at 395 nm [116]. The GS20 scintillator has a refractive index of 1.55 at emission maximum (395 nm), a light output relative to anthracene of 20% [72], and a 1/e absorption length of $\sim$ 12 cm at 395 nm.

At a wavelength of 395 nm the EJ-560 silicone optical interface has a refractive index of 1.43 [111] and a 1/e absorption length $\lambda \sim$ 3.9 cm. The optical epoxy is modelled on Eljen EJ-500 optical cement which has a refractive index of 1.57 [112] and a 1/e absorption length λ $\sim$ 0.6 cm. The borosilicate glass on the front of the MAPMT has a refractive index of approximately 1.53 and a 1/e absorption length $\lambda \sim$ 416.7 cm. Matching the refractive indices of the scintillator, optical coupling and MAPMT window materials is important to minimise reflection at the boundaries.

Photon Transport

The General Particle Source generates photons isotropically within the GS20 scintillator, that travel through the detector components and undergo absorption, Rayleigh scattering, and medium boundary processes. These boundary processes are simulated using the 'Glisur Model' of Geant4 and include [117]:

1. Dielectric - Dielectric, wherein depending on the photon's wavelength, angle of incidence, polarisation, and the refractive indices of the boundary materials the photon may undergo; total internal reflection, Fresnel reflection, and Fresnel refraction.

2. Dielectric - Metal, where the photon is absorbed (detected) or reflected.

3. Dielectric - Black, where the photon is absorbed.

The photons that are absorbed on the photocathode have their absorption location, wavelength, direction, and interaction position recorded. Photons absorbed outside of the photocathode or scattered beyond the detector volume are not recorded.

3.1.2 Procedure

The goal of the optical simulation is to determine how different configurations of scintillator and optical coupling affect the amount of optical crosstalk and the number of photons collected on the target pixel. Fig. 3.2a shows the trajectories of optical photons (indicated by the green tracks) scattering within a pixellated scintillator, and the side view (Fig. 3.2b) of the detector displays the GS20 scintillation glass (cyan), the borosilicate glass of the H12700 MAPMT (blue), and the bialkali cathode. The characterisation of the SoNDe module has been achieved by studying various detector configurations. For each of the configurations 10^6 optical photons were generated at the centre of P45 at a scintillation glass depth of 0.5 mm. For photons generated randomly within P37 see Ref. [110].

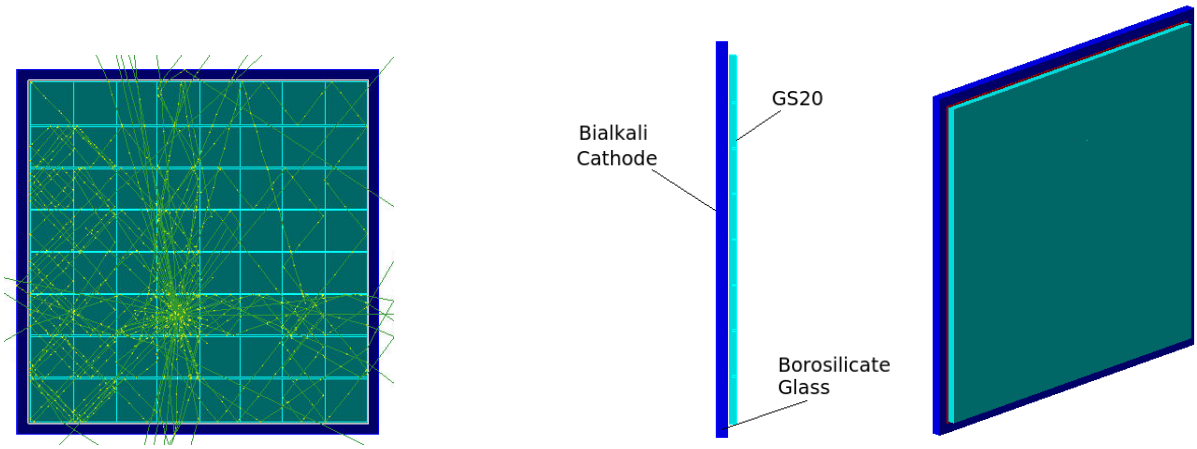

Figure 3.2: A visualisation of the SoNDe module front end. (a) A square pixellated scintillator, each pixel measuring 6×6 mm^2 with pixel 1 situated top left and pixel 64 at the bottom right. The optical photons have been generated isotropically at the centre of pixel 45 for 100 events. (b) A side-view of the detector setup which features the GS20 scintillator (cyan), the borosilicate glass (blue), and the bialkali photocathode deposited on the back. The dynode chains and back-end electronics are not included in the simulation. (c) A non-pixellated scintillator sheet placed on the MAPMT face.

The 73 simulated studies are listed below in Table 3.1 with repeated information omitted. The studies are numbered in an *i-j* format, where *i* denotes the variable and *j* corresponds to an increase in the magnitude of the variant. Studies 0-0 to 3-5 increase the pixellated depth 'PD'

in increments of 0.2 mm whilst maintaining a constant pixellated width 'PW' and varying the combination of scintillator coating 'SC' and optical coupling 'OC'. Studies 4-0 to 7-7 increase the PW in increments of 0.1 mm whilst maintaining a constant PD and varying the combination of external coating and optical coupling. Studies 8-0 to 9-4 increase the OC thickness in increments of 1.0 mm for two different coupling materials (EJ-560 and EJ-500) for a non-pixellated scintillator sheet with no SC. Study 10-0 to 10-3 varies the SC for a non-pixellated scintillator sheet with no OC (default is 0.05 mm air gap). Finally study 11-0 to 11-2 looks at the effect of a pixellated scintillator sheet with OC and varying SC.

The analysis for each of these studies focuses on the 'true-hit efficiency' ε_T and the 'true-to-false ratio' R_{TF} of hits in a given pixel. If n_T denotes the number of photons detected in the target pixel, n_F the number of photons detected outwith the target pixel, and P_N the total number of photons initially generated within the target pixel (in this case 1×10^6 events), then true-hit efficiency $\varepsilon_T = 100 \times n_T/P_N$, which is the ratio of detected photons to total generated photons within a pixel expressed as a percentage (%) (Fig. 3.3a). The true-to-false ratio $R_{TF} = n_T/n_F$ is the ratio of detected photons in the target pixel to the number of photons detected outwith the target pixel P45 (Fig. 3.3a).

The photon displacement δr from generation position can be determined as the x - y translation distance, $\delta\mathrm{r} = \sqrt{\delta x^2 + \delta y^2}$, where δx and δy are the differences between the initial photon generation position and the photon detection coordinates on the position sensitive photocathode (Fig. 3.3b).

The results for studies 5-0 and 8-4 are shown in Figs. 3.3 and 3.4 respectively, and a full summary of results is shown in Fig. 3.5 with ε_T displayed in red, R_{TF} in green, and δr in blue. The X-axis represents each study in *i-j* format from 0-0 to 11-2. The error-bars displayed on each histogram represent the standard deviation (σ) of P45. The uncertainty is calculated by splitting the Monte Carlo run into n-sub runs, e.g. 10 sets of 10^5 started photons in a total run of 10^6. In the case of true-hit efficiencies ε_T (Fig. 3.5a),

$$\sigma_\varepsilon = \sqrt{\frac{\sum_{i=1}^{N} (\varepsilon_i - \varepsilon_T)^2}{N-1}} \tag{3.1}$$

where each sub-run 'i' (i = 1-10) gives a value of true-hit efficiency ε_i, ε_T represents the true-hit efficiency for 10^6 events, and N = 10. Fig. 3.5b shows the pixel averaged mean true-to-false ratio R_{TF}, the error is given by the standard deviations of the individual-pixel ratios (calculated in a similar manner). Fig. 3.5c displays the mean values of δr for P45, where the error bars denote the standard deviation of the mean, related to the spread in event-by-event δr values over the entire detector region.

The current SoNDe DAQ system, in production mode, will not provide all of the information necessary for a cluster analysis of scintillation photon detection positions. This has emphasised

the importance of the scintillation photons being detected as closely as possible to the point of production. The ideal detector configuration would have high values of ε_T and R_{TF}, and a low δr value. However, optimising R_{TF} and δr may come at the expense of decreased ε_T. From the summarised results in Fig. 3.5 the greatest ε_T is achieved when the GS20 sheet is both grooved and coated in TiO_2 (studies 1 and 5), however these results have very low R_{TF} values and larger average δr values. The greatest R_{TF} is achieved when using a scintillator with: no grooves, no scintillator coating, and no optical coupling (current SoNDe module arrangement). This setting also gives the lowest δr. However, the ε_T of this setup is low $\sim 2.5\%$. Where an optical coupling medium is used, increasing the thickness of the coupling film (studies 8 and 9) causes decreasing ε_T and R_{TF} values, and increasing δr values. When a reflective coating is applied to the GS20 without an optical coupling, TiO_2 has the best ε_T, and matt Al the best R_{TF} and δr values. With the addition of an optical coupling, the TiO_2 is marginally better in all three results categories.

Given the varying setups studied in the simulation, the current SoNDe module configuration (no pixellated grooves, coatings, or couplings) would be the recommended choice going forward due to its high true-to-false ratio and low photon displacement. Although ε_T is low in this case, it is still sufficiently large to give reasonable numbers of detected photons. The SoNDe Test Module, thus far, has been thoroughly characterised using 404 nm laser light and simulated optical photons. It is important to understand the detector's response to ionising radiation, namely alpha and triton particles produced from the ^{6}Li neutron capture reaction. This can be investigated using an ^{241}Am alpha source and will be discussed in Sec. 3.2 and Ch. 4.

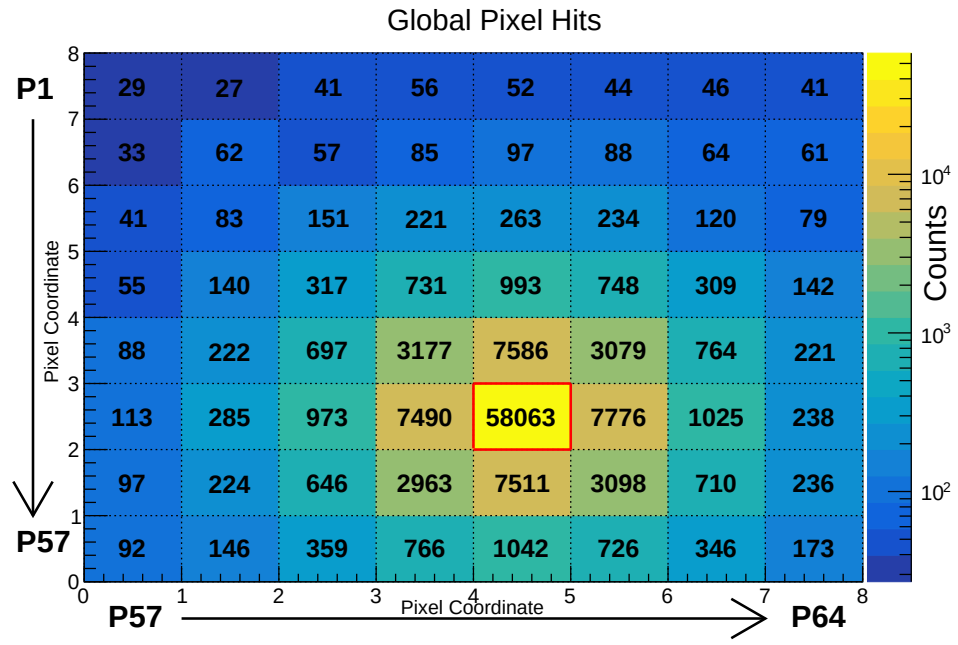

(a)

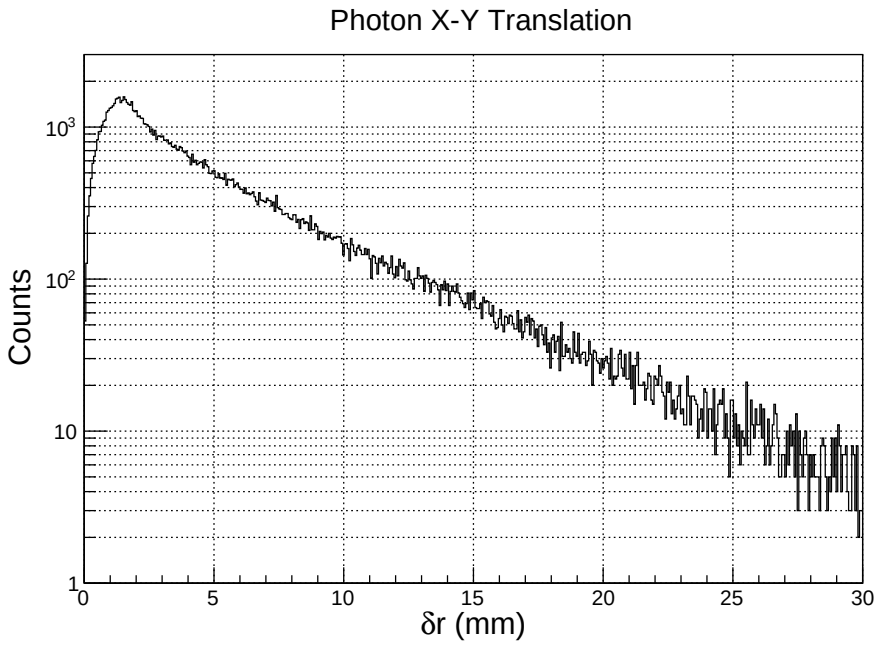

(b)

Figure 3.3: Results for study 5-0. (a) The target pixel P45 highlighted with a red border has 58063 detected photons from a total of 10^6 generated photons, giving ε_T = 5.81%. The total number of 'false hits' which equates to 58379, giving an R_{TF} = 0.995. (b) the distribution of δr which has a mean value of 5.01 mm.

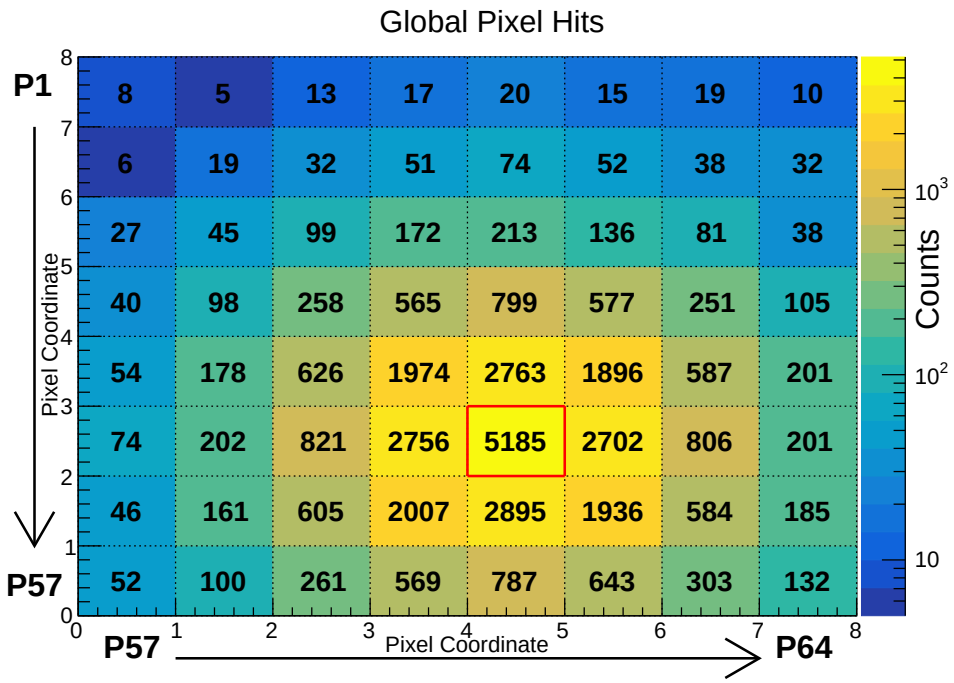

(a)

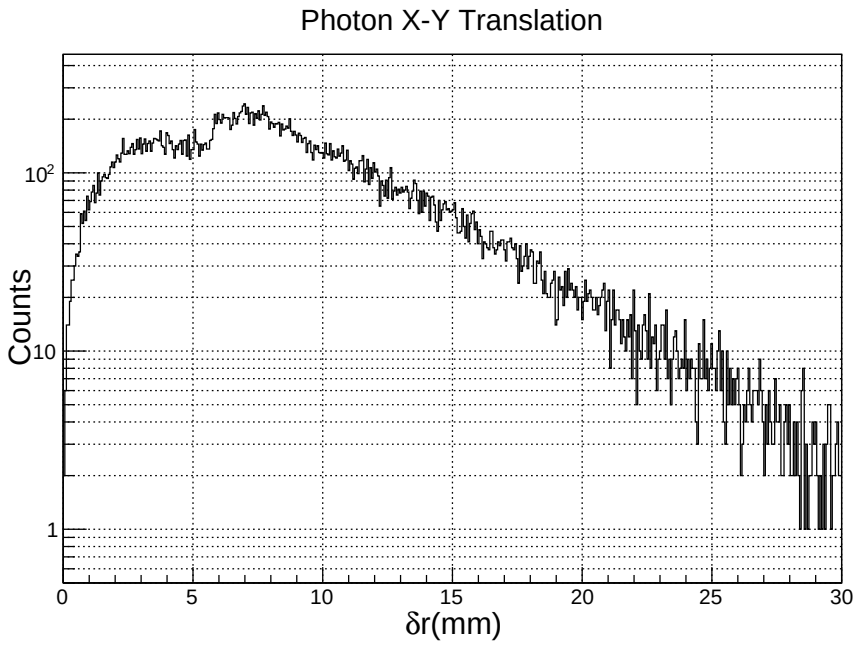

(b)

Figure 3.4: Results for study 8-4. (a) The target pixel P45 highlighted with a red border has 5185 detected photons from a total of 10^6 generated photons, giving ε_T = 0.519%. The total number of 'false hits' which equates to 31022, giving a R_{TF} = 0.167. (b) the distribution of δr which has a mean value of 8.73 mm.

3.1.3 Ionising Radiation

Radiation Transport in GS20

As previously mentioned the simulation has been extended to include different forms of ionising radiation. For interactions in the GS20 scintillator they have been modelled using the high-precision hadronic interaction class FTFP_Bert_HP and electromagnetic interaction classes G4 EmStandardPhysics and G4EmExtraPhysics.

For thermal neutrons the following classes were used to model the particle interactions within the scintillator; high-precision hadronic interaction class FTFP_Bert_HP, G4Neutron TrackingCut, G4NeutronHPThermalScattering, and G4NeutronHPThermalScatteringData.

The simulation traces the path of primary and any subsequent (from gamma-rays or neutrons) charged particles through the detector materials and records the energy loss of the particle, the mean step position and the time with respect to particle production at the source for each discrete step.

The Birks parameter models the non-linear response of the scintillator (with respect to energy deposit) which is due to quenching interactions between the excited molecules created along the path of the incident particle, i.e. interactions which drain energy which would otherwise go into luminescence [28]. The material dependent Birks parameter k_B is expressed within the following equation [118],

$$\frac{dL}{dx} = S\frac{\frac{dE}{dx}}{1 + k_B\frac{dE}{dx}} \tag{3.2}$$

where *dL/dx* is the scintillation light yield per unit path length, *S* is the scintillation efficiency, and *dE/dx* is the differential charged particle energy loss. The Geant4 simulation measures the Birks parameter in units of mm/MeV. An estimated value of k_B = 0.01 mm/MeV was used, equating to k_B = 0.0025 g/cm^2/MeV for the GS20 (ρ = 2.5 g/cm^3). In general inorganic scintillators have relatively low values of k_B [119], if compared to organic scintillators. The value of 0.01 mm/MeV is discussed in Sec. 5.5.

Full Calculation

The ionisation events produce scintillation photons along these charged-particle tracks. Čerenkov radiation is produced if the charged-particle velocity is greater than the group velocity of light within the medium. The optical photons are tracked in the same manner as in the 'Photon Transport' section and both optical photon and charged-particle parameters are recorded at each step in the tracking process as described above. The event by event data is recorded as a ROOT TTree format and analysed using a ROOT C++ macro. As mentioned previously, comparison plots of the measured and simulated data for alpha particles, protons, neutrons and gamma radiation are discussed in Sections 4.4.2, 6.3 and 5.4 respectively.

Table 3.1: Summary of simulation runs with PD = Pixellated Depth, PW = Pixellated Width, SC = Scintillator Coating, OC = Optical Coupling, CT = Coupling Thickness. Repeated information has been omitted.

Study #	Variant	PD / mm	PW / mm	SC	OC	CT / mm
0-0	PD	0.0	0.0	None	Air	0.05
0-1	PD	0.2	0.4	None	Air	0.05
0-2	PD	0.4	0.4	None	Air	0.05
0-3	PD	0.6	0.4	None	Air	0.05
0-4	PD	0.8	0.4	None	Air	0.05
0-5	PD	1.0	0.4	None	Air	0.05
1-0	PD	0.0	0.0	TiO_2	Air	0.05
1-5	PD	1.0	0.4	TiO_2	Air	0.05
2-0	PD	0.0	0.0	None	EJ-560	1.0
2-5	PD	1.0	0.4	None	EJ-560	1.0
3-0	PD	0.0	0.0	TiO_2	EJ-560	1.0
3-5	PD	1.0	0.4	TiO_2	EJ-560	1.0
4-0	PW	0.0	0.0	None	Air	0.05
4-1	PW	0.8	0.1	None	Air	0.05
4-2	PW	0.8	0.2	None	Air	0.05
4-3	PW	0.8	0.3	None	Air	0.05
4-4	PW	0.8	0.4	None	Air	0.05
4-5	PW	0.8	0.5	None	Air	0.05
4-6	PW	0.8	0.6	None	Air	0.05
4-7	PW	0.8	0.7	None	Air	0.05
5-0	PW	0.0	0.0	TiO_2	Air	0.05
5-7	PW	0.8	0.7	TiO_2	Air	0.05
6-0	PW	0.0	0.0	None	EJ-560	1.0
6-7	PW	0.8	0.7	None	EJ-560	1.0
7-0	PW	0.0	0.0	TiO_2	EJ-560	1.0
7-7	PW	0.8	0.7	TiO_2	EJ-560	1.0
8-0	OC	0.0	0.0	None	EJ-560	0.0
8-1	OC	0.0	0.0	None	EJ-560	1.0
8-2	OC	0.0	0.0	None	EJ-560	2.0
8-3	OC	0.0	0.0	None	EJ-560	3.0
8-4	OC	0.0	0.0	None	EJ-560	4.0
9-0	OC	0.0	0.0	None	EJ-500	0.0
9-4	OC	0.0	0.0	None	EJ-500	4.0
10-0	SC	0.0	0.0	None	Air	0.05
10-1	SC	0.0	0.0	TiO_2	Air	0.05
10-2	SC	0.0	0.0	Polished Al	Air	0.05
10-3	SC	0.0	0.0	Matt Al	Air	0.05
11-0	SC	0.8	0.4	TiO_2	EJ-560	1.0
11-1	SC	0.8	0.4	Polished Al	EJ-560	1.0
11-2	SC	0.8	0.4	Matt Al	EJ-560	1.0

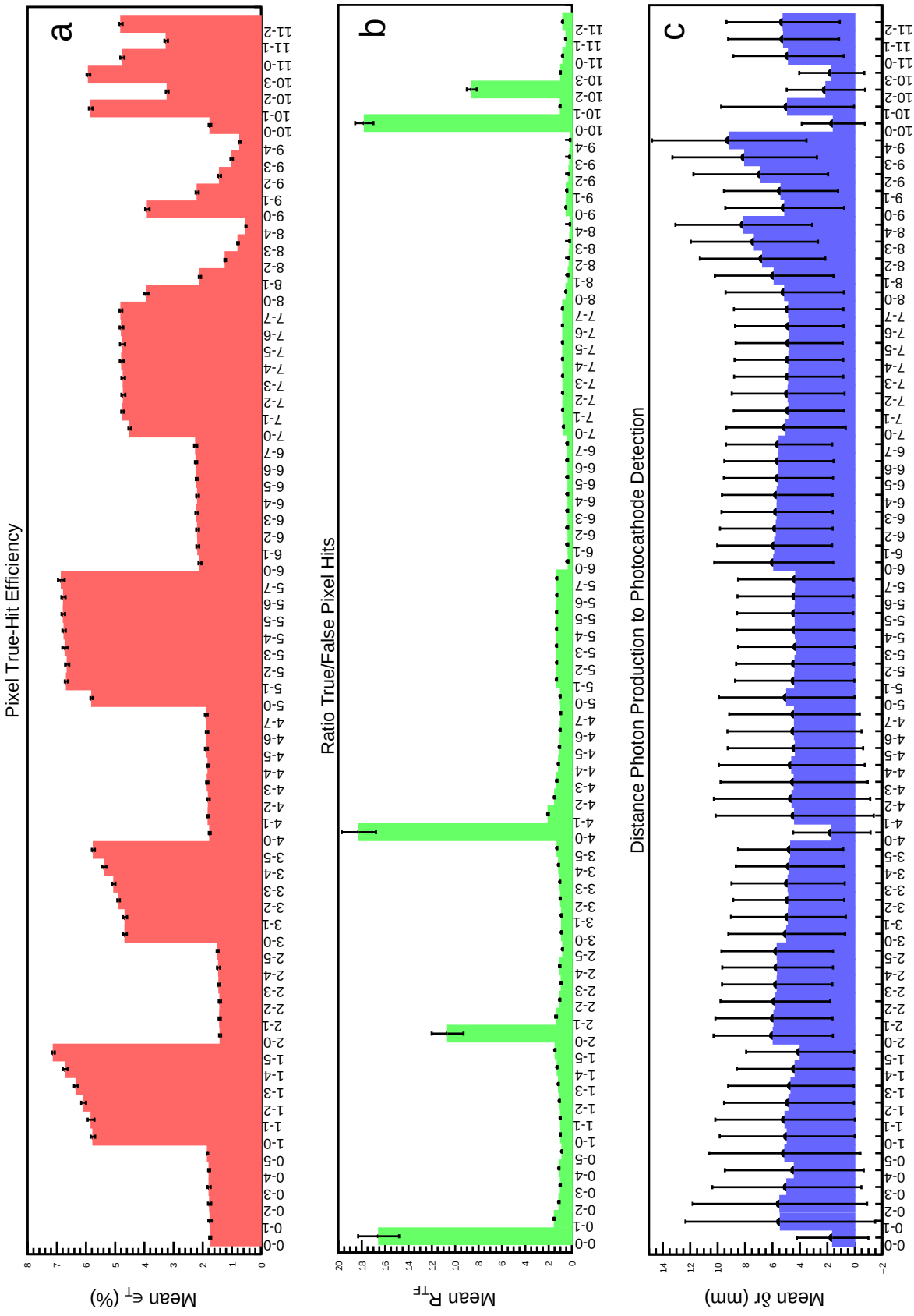

Figure 3.5: Summary of results for the 73 simulated studies showing (top, red) true hit efficiency as a percentage, (middle, green) the true-to-false ratio of hits, and (bottom, blue) the mean photon displacement in mm. The x-axis labels relate to run designation, as in Table 3.1.

Chapter 4

Characterisation using Americium-241

4.1 Motivation

The laser scans gave an in depth look at the response of the MAPMT to a beam of light of a similar wavelength expected from the GS20 scintillation glass. The ^{6}Li doped scintillator is designed to capture thermal neutrons and release alpha (2.05 MeV) and triton (2.73 MeV) particles,

$$^6_3\mathrm{Li} + ^1_0\mathrm{n} \rightarrow ^7_3\mathrm{Li}^* \rightarrow ^4_2\mathrm{He} + ^3_1\mathrm{H} + 4.78 \ \ \mathrm{MeV}. \tag{4.1}$$

The alpha and triton particles ionise the Ce^{3+} by exciting its outermost electron which de-excites after $\leq$ 100 ns, releasing scintillation photons of peak wavelength 395 nm (laser λ = 404 nm). The ionisation interactions of alpha particles within the GS20 scintillation glass are of interest. The range of alpha particles in GS20 is known ($\sim$ 7 μm), however the isotropic scintillation photon spread and extent of crosstalk into adjacent pixels can extend to much larger distances. This will affect the SoNDe detector's ability to resolve the location of capture events. An alpha beam is much easier to control/collimate within a small lab setup in comparison to a thermal neutron beam. Given these conditions, an alpha source was used to mimic the SoNDe Test Module's response to thermal neutrons.

4.2 ^{241}Am Source Properties

^{241}Am is an unstable nucleus that decays by alpha particle emission to produce the daughter nuclide ^{237}Np via the reaction

$$^{241}_{95}\mathrm{Am} \rightarrow ^{237}_{93}\mathrm{Np} + ^4_2\mathrm{He} + 5.638 \ \mathrm{MeV}. \tag{4.2}$$

5.638 MeV is the total kinetic energy released by the alpha decay [120]. The decay energy, Q_α, is equivalent to the total kinetic energy K_T, and is the sum of the individual energies of the alpha particle (E_α), recoil daughter nucleus (E_{recoil}), and gamma radiation (E_γ). It can be represented

as,

$$Q_\alpha = K_T = E_\alpha + E_{\text{recoil}} + E_\gamma. \tag{4.3}$$

The gamma-rays are produced in the de-excitation of the excited states of ^{237}Np populated in the alpha decay. The decay scheme for ^{241}Am is shown in Fig. 4.1. There are five distinct alpha energies with which the ^{241}Am decays. Their relative branching fractions are shown on the right in brackets as a percentage, with the most prominent alpha decay at 5.486 MeV. As previously mentioned, the 5.638 MeV decay energy (Q_α) is shared between the alpha particle (5.486 MeV) and the excited daughter nucleus. The recoil energy of the ^{237}Np and subsequent gamma-rays (de-excitation) account for some of the missing energy $\sim$ 150 keV. The recoil energy of the daughter nuclei can be calculated as a ratio of the ejected masses,

$$E_{\text{recoil}} = \frac{M_\alpha}{M_{\text{recoil}}} E_\alpha. \tag{4.4}$$

M_α represents the mass of the alpha particle, and M_{recoil} the mass of the recoiling daughter nuclei. The recoil energy will vary with the emitted alpha energies, and therefore the subsequent gamma energies can be found via,

$$E_\gamma = Q_\alpha - E_\alpha - E_{\text{recoil}}. \tag{4.5}$$

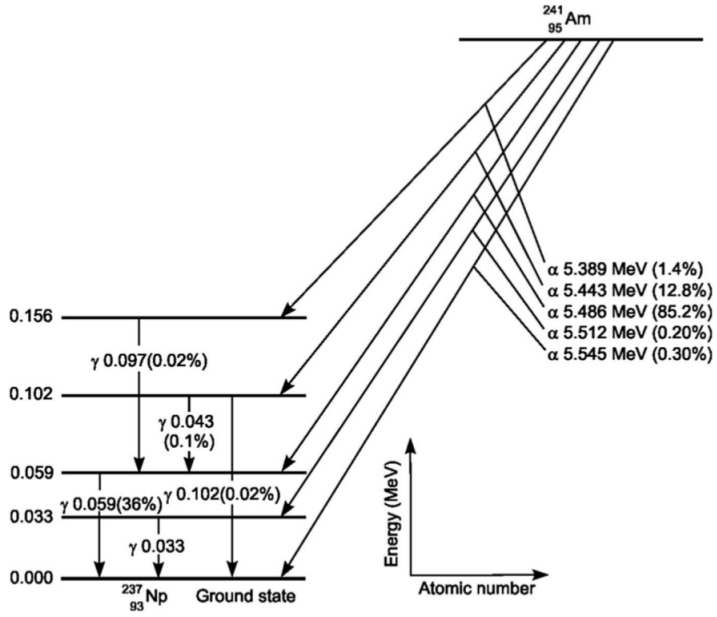

Figure 4.1: Decay scheme for ^{241}Am via alpha emission (relative intensity percentages in brackets) and subsequent gamma emissions to the ground state of ^{237}Np. Alpha and gamma energies are quoted in MeV. Image taken from [120].

The ^{241}Am source[1] used in the following studies is a closed source encased in steel with a thin mesh window. Its energy was measured by a calibrated Passivated Implanted Planar Silicon (PIPS) detector in a vacuum sealed chamber at SUERC[2]. When measuring the spectrum of ^{241}Am one would expect a peak energy around 5.486 MeV, which as mentioned above is the most prominent peak. The blue ^{241}Am spectrum in Fig. 4.2 shows the mean energy was measured at 4.54 MeV, 17% lower than the expected energy value. The peak is much broader in comparison to the three distributions of the calibration sources shown in black and to the right. The broad energy distribution of the Glasgow ^{241}Am may be attributed to the structure of the casing surrounding the source. A thin containment window covers the front end of the source casing. If this window is non-uniform the alpha energy loss will likewise be non-uniform, leading to a broadening of the energy spectrum. The source loses $\sim$ 1 MeV of energy to the window encapsulating it.

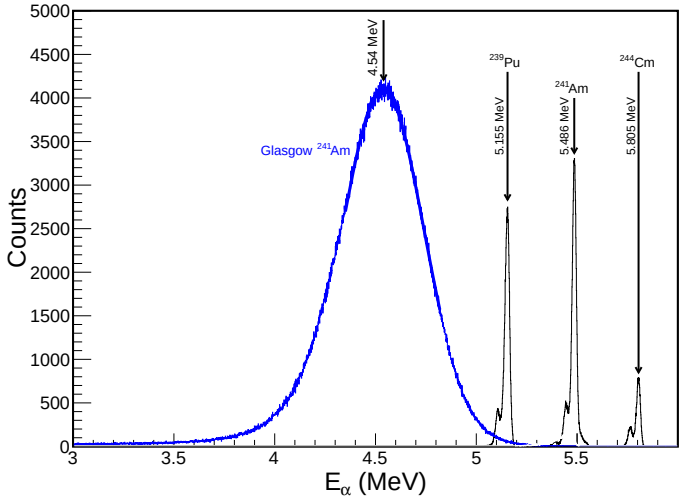

Figure 4.2: Spectra of Glasgow ^{241}Am source (blue) compared against a three-actinide ^{239}Pu, ^{241}Am, ^{244}Cm (black) calibration source. All sources were measured with a PIPS detector in a vacuum chamber.

4.2.1 Geant4 Based Detector Calibration

In order to determine the total energy loss of the incident alpha particles in air, a Geant4 based simulation [110] which employed the measured alpha spectrum in vacuum was used to simulate the mean incident energy upon the scintillator. Parameters such as: source distance to detector, solid angle of radiation, and detector configuration (as described in Sec. 3.1) were input parameters to the simulation.

The Geant4 *G4ionIonisation* class simulates the energy loss of positive ions, and when used

[1]Property of Nuclear Physics Experimental Group, University of Glasgow
[2]Scottish Universities Environmental Research Centre, David Sanderson

in conjunction with the *G4BetheBlochModel* class is valid for protons with T > 2 MeV, where T is the kinetic energy. For heavy charged particles a scaling relationship is required, and is defined as,

$$T_{scaled} = T\frac{M_{base}}{M_{particle}}, \tag{4.6}$$

where T is the kinetic energy, and M_{base} and $M_{particle}$ are the masses of the base particle (proton) and particle (α) [121]. The maximum energy that can be transferred to an unbound/free electron T_{max} can be described by the following equation:

$$T_{max} = \frac{2m_e c^2(\gamma^2-1)}{1+2\gamma(m_e/M)+(m_e/M)^2}, \tag{4.7}$$

where m_e is the mass of an electron and M is the mass of the alpha particle.

For continuous energy loss of heavy ionised particles moving through a medium a modified restricted energy loss (T < T_{cut}) Bethe-Bloch formula is used,

$$\frac{dE}{dx} = 2\pi r_e^2 mc^2 n_{el}\frac{z^2}{\beta^2}\left[ln\left(\frac{2mc^2\beta^2\gamma^2 T_{up}}{I^2}\right)-\beta^2\left(1+\frac{T_{up}}{T_{max}}\right)-\delta-\frac{2C_e}{Z}+S+F\right], \tag{4.8}$$

r_e = classical electron radius = $e^2/(4\pi\varepsilon_0 mc^2)$
mc^2 = mass energy of the electron
n_{el} = electron density in the material
z = charge of the hadron (units of electron charge)
β = 1 - $(1/\gamma^2)$
γ = E/mc^2
T_{up} = min(T_{cut},T_{max}), where T_{cut} is the kinetic energy cut-off or production threshold
I = mean excitation energy in the material
Z = atomic number of the material
δ = density effect function
C_e = shell correction function
S = spin term = 0, for s = 0, $\left(\frac{0.5T_{up}}{E}^2\right)$, for s = 1/2
E = primary energy
F = high order corrections.

For a full and more detailed derivation the reader should consult pg 153 of the Geant4 Physics reference manual [121].

As the alpha particle passes through the GS20 scintillator it loses energy. When the energy drops below 2 MeV the simulation switches calculation of *dE*/*dx* from Eq. 4.8 (as Bethe-Bloch breaks down at low energy) to a parametrisation of evaluated data for stopping powers. The data can be found in [122]. The *G4BraggIonModel* class is automatically included in the

G4ionIonisation class and is used for alpha particle parameterisation. In order to transition between the high and low energy models a modified energy loss equation can be used,

$$P(T) = P_H(T) + (P_L(T_{lim}))\frac{T_{lim}}{T}, \;\; T > T_{lim}, \tag{4.9}$$

where P is smoothed stopping power, P_H is the stopping power dE/dx as described in Eq. 4.8 and P_L is the low-energy parameterisation.

The simulation was used to emulate the laboratory setup and calculate the incident alpha energy upon the GS20 scintillator. A point alpha source, placed in air 5 mm from the GS20 was collimated to produce an angular divergence of 5.7 deg. and beam spot of $\sim$ 1 mm. An incident alpha energy of 4.27 MeV at the face of the GS20 sheet (Fig. 4.3) was found after an energy loss of 270 keV due to air.

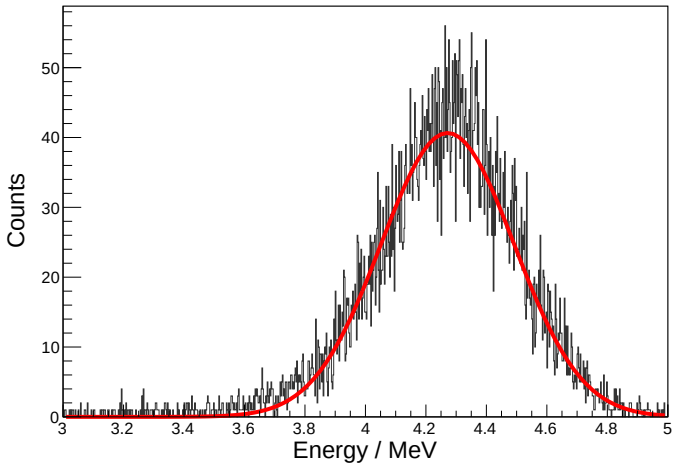

Figure 4.3: Geant4 simulated spectrum of a 1 mm diameter collimated ^{241}Am beam incident upon the surface of the GS20 scintillator (5 mm away), peaking at 4.27 MeV (Gaussian distribution fit in red).

4.3 Individual Pixel Response

The ^{241}Am source was placed in a specially designed 3D-printed plastic collimator with a 1 mm projection hole. A CAD representation can be seen in Fig. 4.4. The collimator was placed at a distance of $\sim$ 4 mm away from the centre of P45. As the scintillation light spreads isotropically from the point of ionisation, the central position of P45 was established by equating the number of counts in each of the four adjacent neighbouring pixels surrounding the target (above, below, left, and right). The response of the SoNDe Test Module is shown in Fig. 4.5. The peak energy recorded by the detector was calculated to the predicted 4.27 MeV.

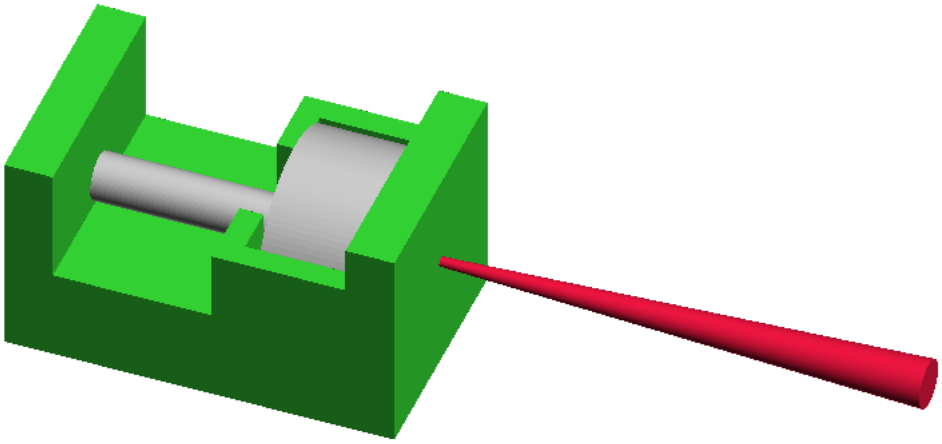

Figure 4.4: CAD drawing of the ^{241}Am alpha source container (silver) located in the collimator. The green collimator features a 0.1 mm circular diameter radiation transmission hole, with a depth of 1 mm. The alpha beam is shown in red.

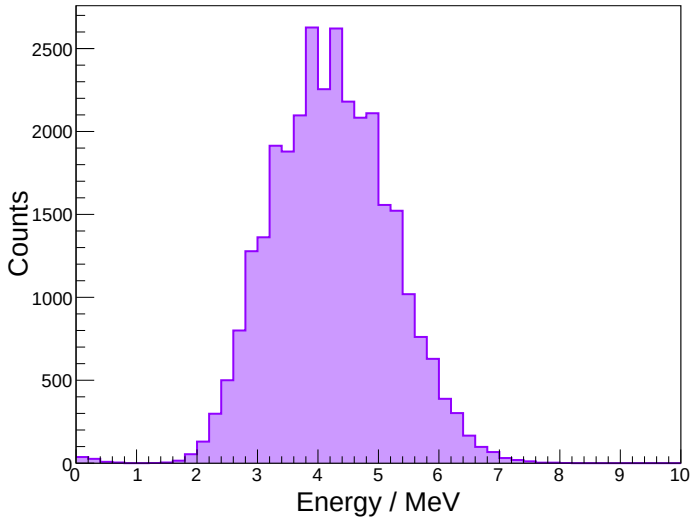

Figure 4.5: Individual P45 response to ^{241}Am alpha source. The mean energy of the source was calculated to be 4.27 MeV (using the Geant4 simulation) and the peak artificially centred at this position. The width of the peak is dominated by the intrinsic resolution of the detector (discussed in Sec. 4.3.4).

4.3.1 Stability Test

The stability of the SoNDe Test Module (minus GS20) was studied previously using a 404 nm laser beam as reported in Sec. 2.2.2. Here it was investigated with the addition of the GS20 scintillation glass and the ^{241}Am source. The test was conducted at -1000 V using the same setup as described above in Sec. 4.3. Similar to the previous stability test, the detector was started from 'cold', meaning the MAPMT was not provided with a 'warm-up' period (30 - 60 minutes recommended by Hamamatsu) before the data acquisition began. The resultant plot is

shown in Fig. 4.6 with 60 minutes marked by a black dashed line and 24 hour periods with blue dashed lines. The alpha spectra were recorded at regular time intervals (78 seconds), fitted with Gaussian distributions, and the peak energy of each plotted against time. A drift of 3.44×10^{-7} MeV/s (2.30×10^{-5} QDC bins/s) was found, equivalent to 2.93×10^{-4} %/hr. By comparison the laser drift test gave 1.15×10^{-4} %/hr. The projected drift in mean alpha energy over a 24 hour period is 30 keV/day. This level of drift is not a concern for the running of the detector over an extended period. However, from examining the data a warm up period of at least 30 - 60 minutes is strongly encouraged.

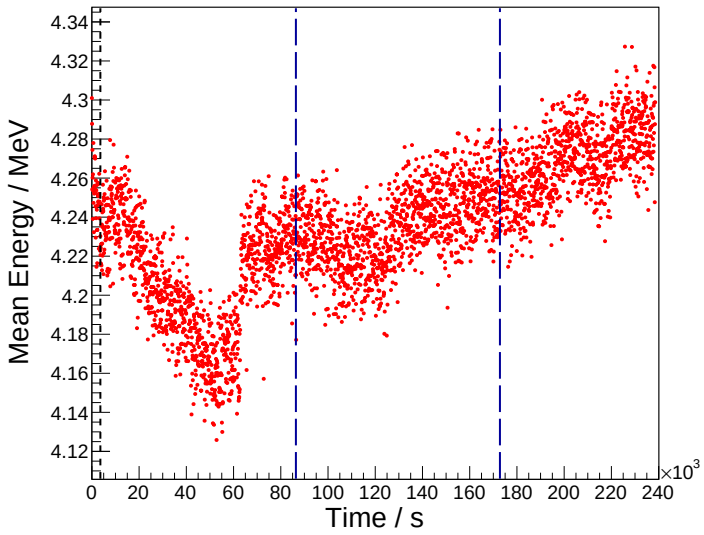

Figure 4.6: SoNDe Test Module stability test conducted using ^{241}Am alpha source directed at P45. The MAPMT was started from 'cold', i.e. no warm-up time. The recommended 60 minute warm-up period is marked with a vertical dashed black line (far left). The test was carried out over a 67 hour period with 24 hour periods marked in vertical dashed blue lines.

4.3.2 High Voltage Gain Variations

For the H12700A MAPMT the recommended high voltage (HV) input is -1000 V [83]. The relationship between HV and pixel gain (from signal amplitude) can be observed by varying the HV input of the detector. Similar to the stability tests, the collimated source was centred on P45. The MAPMT was given 60 minutes warm-up time and the DAQ activated for 300 seconds for each HV setting which ensured adequate statistics ($\sim$ 10,000 events). The signal strength of P45 measured for each HV setting is defined as: alpha peak (QDC bin) - pedestal peak (QDC bin), similar to the measurements in Sec. 2.2.5. The results of these measurements are shown in Fig. 4.7. A non-linear increase in gain (current amplification) is observed as the HV is increased. The relationship between the gain μ and supply voltage V is given by

$$\mu = a^n \left(\frac{V}{n+1} \right)^{kn}, \tag{4.10}$$

where a is a constant, n is the number of dynode stages, and k is determined by the composition/structure of the dynodes [78].

Although a higher gain can be achieved by running at an increased HV it is not necessary for this application. For the expected light intensities of a few hundred photons per event, sufficient amplification is achieved close to the recommended HV setting of -1000 V. Associated disadvantages of running at higher voltages include: performance deterioration "fatigue", short-term death of the signal, decreased longevity of detector, increased running costs for cooling the detectors and power consumption, and increased leakage current between anodes and other electrodes [78].

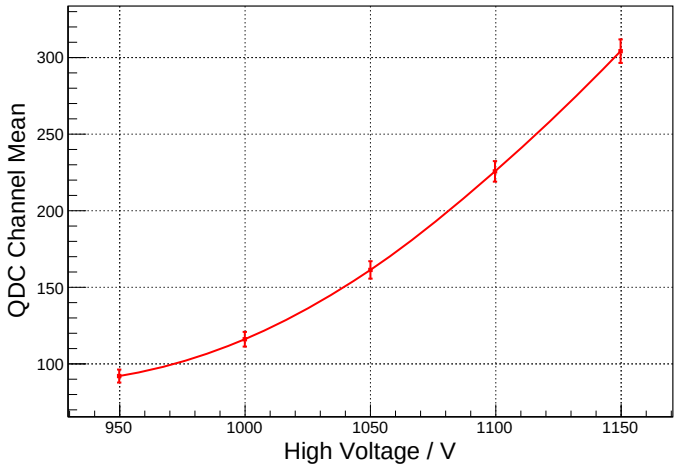

Figure 4.7: Plot of the variation in gain versus the high voltage for SoNDe Test Module P45 (plotted as the magnitude of the negative polarity HV). The HV was increased in steps of 50 V and measurements were taken over a five minute period per step.

4.3.3 Gain Map Comparison

The individual response for all 64 pixels to alpha radiation was used to establish a gain map for the detector that could be compared with the specification provided by the Hamamatsu engineers. The SoNDe Test Module's response to the alpha beam is in short pulses of localised scintillation light, contrasting with the steady-state tungsten lamp illumination utilised by Hamamatsu. Therefore, it is important to understand the relative gain variations of the detector when using different sources of radiation. As described in Sec. 4.3, the source was centred on each individual pixel for a period of 300 seconds and moved on to the next. The gain map provided in the specification document for the detector is shown in Fig. 2.4. The recommended HV for the H12700A MAPMT is -1000 V, and its corresponding gain map is shown in Fig. 4.8. The

MAPMTs used in the SKADI instrument may be operated at different high voltages to iron out gross differences in gain. The effects of increasing the HV (-1150 V) on the detector gain are seen in Fig. 4.9.

At both HV settings the general trend of the Hamamatsu gain map is reproduced, i.e. a high gain region along the 5th column of pixels, lower gain pixels around edges. Both data sets show a spurious result for P10 (labelled as < 50). This was most likely due to a loose electronic connection as this pixel did not present itself as low gain in other measurements. These data sets were therefore analysed out of 63 pixels as opposed to 64. A comparison of the main properties of the gain maps is shown in Table 4.1, where σ represents the standard deviation of all relative gain values.

Table 4.1: Comparison of the four properties used to define the gain variation of the MAPMT for the Hamamatsu specification, 404 nm laser data (spot and diffuse), and data taken with the alpha source at -1000 V and -1150 V.

Measurement	σ	Anode Ratio	Conform to 1.0 : 2.0 Ratio
Hamamatsu at -1000 V	11%	1.0 : 2.0	64/64
Alpha at -1000 V	9%	1.0 : 1.6	63/63
Alpha at -1150 V	11%	1.0 : 1.8	63/63
Laser spot at -1000 V (1 PE)	16%	1.0 : 3.1	58/64
Laser diffuse at -1150 V (120 PE)	12%	1.0 : 1.9	64/64

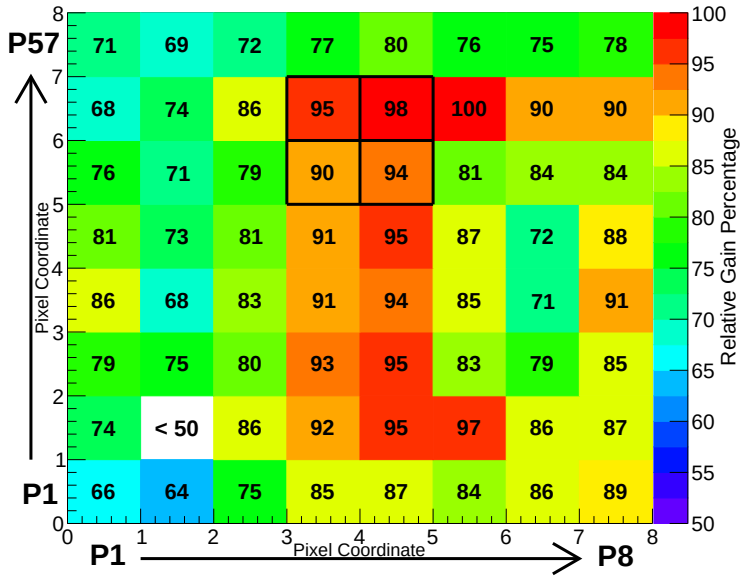

Figure 4.8: Heat map representation of measured alpha particle gain map at -1000 V with standard deviation $\sigma = 9\%$, ratio of anode output 1.0 : 1.6, and 63/63 conforming to the Hamamatsu specification of factor 2 variation in gain. The 2×2 pixels outlined in black are pixels 44, 45, 52, and 53. These pixels were scanned in multiple directions and the results discussed later in the chapter.

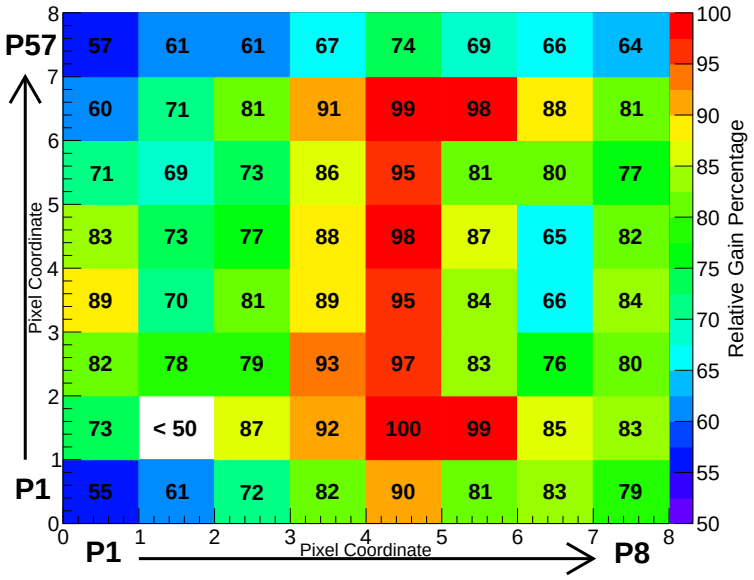

Figure 4.9: Heat map representation of measured alpha particle gain map at -1150 V with standard deviation $\sigma = 11\%$, ratio of anode output 1.0 : 1.8, and 63/63 conforming to the Hamamatsu specification of factor 2 variation in gain.

In order to compare both of the alpha data sets the 'average gain ratio per pixel' (R_{GA}) was calculated using the equation

$$R_{GA} = \sum_{i=1}^{64} \frac{(g_{1000i}/g_{1150i})}{64}, \tag{4.11}$$

where g_{1000i} and g_{1150i} are the relative gains corresponding to pixel i for each data set. R_{GA} = 1.06, meaning the relative pixel gains for both data sets are largely in agreement. The average relative gain over the 64 pixels for the -1000 V data is greater than the -1150 V data, at 82 and 79 respectively. Disregarding the P10 result from both data sets, this method yields slightly improved results to the laser methods. The alpha method includes effects that the laser does not, e.g. non-uniformity in scintillation intensity and light collection efficiency. It was not possible to illuminate all 64 pixels simultaneously with the ^{241}Am source due to the short range of alpha particles in air (< 5 cm) [123]. Alpha scanning offers a possible method of calibrating the detector at ESS.

4.3.4 Pixel Dependence of Pulse Height Resolution

The energy resolution 'R' of a detector is a measure of its ability to distinguish between radiation of different energies. It is defined as $R = \frac{FWHM}{H_0}$, for a Gaussian distribution with standard deviation σ, the FWHM = 2.35σ, and H_0 is the average pulse height [61]. These are represented in Fig. 4.10. The ratios of FWHM to relative pixel gain for the 64 pixels of the SoNDe Test Module are shown in Fig. 4.11. This data was obtained from the -1000 V gain map study. The

raw data signal in units of QDC bins from each channel was fitted with a Gaussian distribution and the FWHM extracted. The data set has an average FWHM / relative pixel gain = 0.7 and a standard deviation $\sigma = 0.07$.

The ability to resolve several energy peaks from the same source is demonstrated by the PIPS detector in Fig. 4.2. Lower energy peaks are visible to the left of the main calibration peaks for the ^{239}Pu, ^{241}Am, and ^{244}Cm sources. The resolution of the PIPS detector based on the ^{241}Am calibration source is R = 0.0047 (0.47%). The PIPS detector shows the intrinsic width of the Glasgow ^{241}Am source, which is measured as R = 0.11 (11%). The 'relative width' of the Glasgow ^{241}Am source for the SoNDe Test Module is R = 0.51 (51%). This value results from convoluting the intrinsic width of the source and the detector resolution of the SoNDe Test Module.

Thus this SoNDe Test Module will struggle to resolve/separate multiple peaks with energies closer than 1.9 MeV. If the energy of the ^{6}Li neutron capture decay products (α + ^{3}H) are similar to the gamma background radiation in the SKADI instrument then it may not be possible to separate the neutron and gamma-ray signals cleanly.

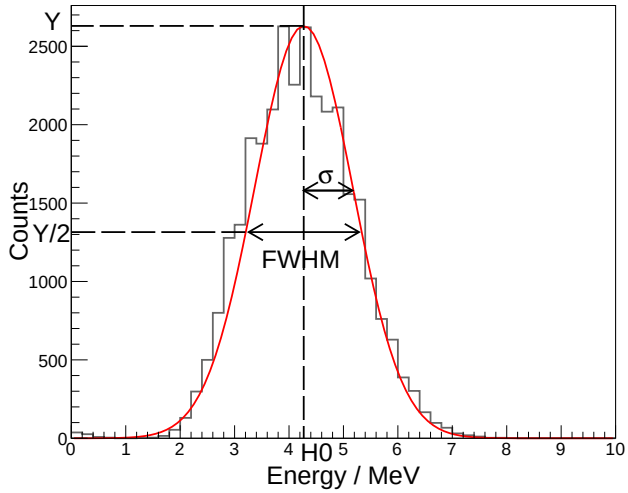

Figure 4.10: A representation of detector energy resolution including the full width at half maximum (FWHM), standard deviation (σ), and the average pulse height (H_0).

4.4 Cross-Pixel Scans

In order to validate the Geant4 based simulation for the alpha particles, millimetre stepped scans across the pixel boundaries in the horizontal, vertical, and diagonal directions were carried out. The number of detected photons, peak mean, and peak width for each scanned position were compared for both measured and simulated data. The definition of a detected photon for the simulated detector is when the photocathode of the sensitive detector receives a hit. The quantum efficiency of the detector at 395 nm ($\sim$ 33% [83]) is used to determine the number of

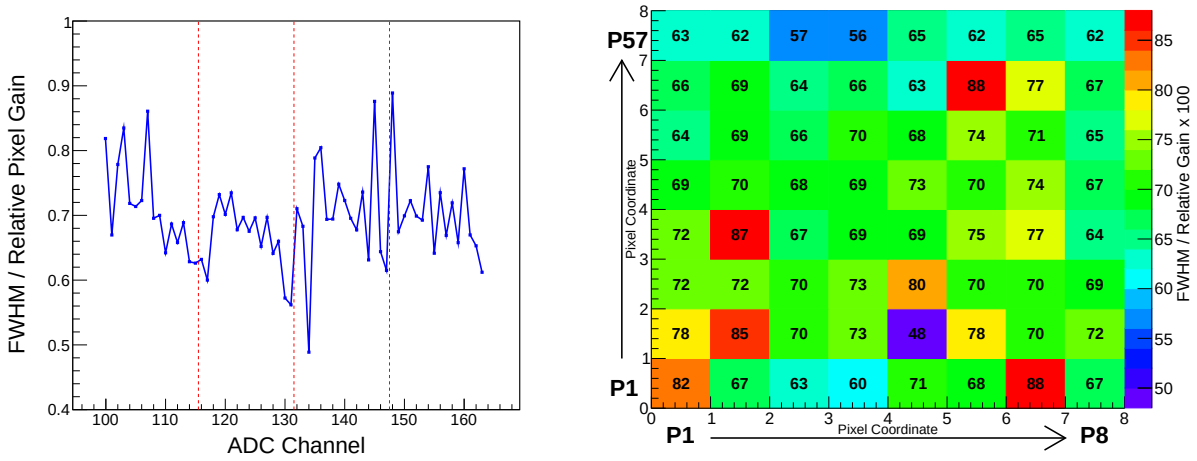

(a) (b)

Figure 4.11: (a) Detector channel FWHM / relative pixel gain variation at -1000 V. (b) The FWHM / relative pixel gain ($\times$ 100) variation across the detector pixels at -1000 V.

photoelectrons produced from this interaction. The fitted mean signal taken at the centre of P45 in QDC bins was equated by a scale factor to the mean number of photons at the same position for the simulation. This scale factor was used to convert all measured signals to a 'Scaled QDC Channel', equivalent to the number of detected photons for a direct comparison.

The electronic setup used to obtain the measured data is displayed in Fig. 4.12. Unlike the laser scans, the alpha measurements are triggered via the dynode 10 (D10 OR of all signals) signal from the MAPMT. This pulse is amplified, inverted, and then discriminated using a voltage threshold to reduce noisy background signals. This discriminated D10 signal is then used to generate the QDC gate. The width of the QDC gate is set to 120 ns and an oscilloscope was used to check that the MAPMT anode signals arrived at the QDC $\sim$ 25 ns after the start of the gate signal to allow the QDC gate circuitry to open fully and capture the complete MAPMT signals. Circuit E at the top is an oscillator circuit used to produce the pedestal signals. Again the VMEbus master (CAEN2718) is connected to a PC via optical link, providing an event-readout "interrupt" to the PC and to reset the trigger busy signal.

4.4.1 Setup and Procedure

The ^{241}Am source was placed in the collimator and positioned 5 mm away from the SoNDe Test Module. The collimator was fixed to the motorised X-Y translator and scanned in 1 mm steps in the horizontal, vertical, and diagonal directions from the centre of P45 to the centre of pixels 44, 52 and 53 (Fig. 4.13). These four pixels were initially chosen due to their high gain (according to the specification sheet provided by Hamamatsu). The starting position '1' was identical for each scan and the spectrum for both scanned pixels (44 and 45 for a horizontal scan) recorded simultaneously at each position. The four pixel intersection (position 4 in the diagonal scan) is

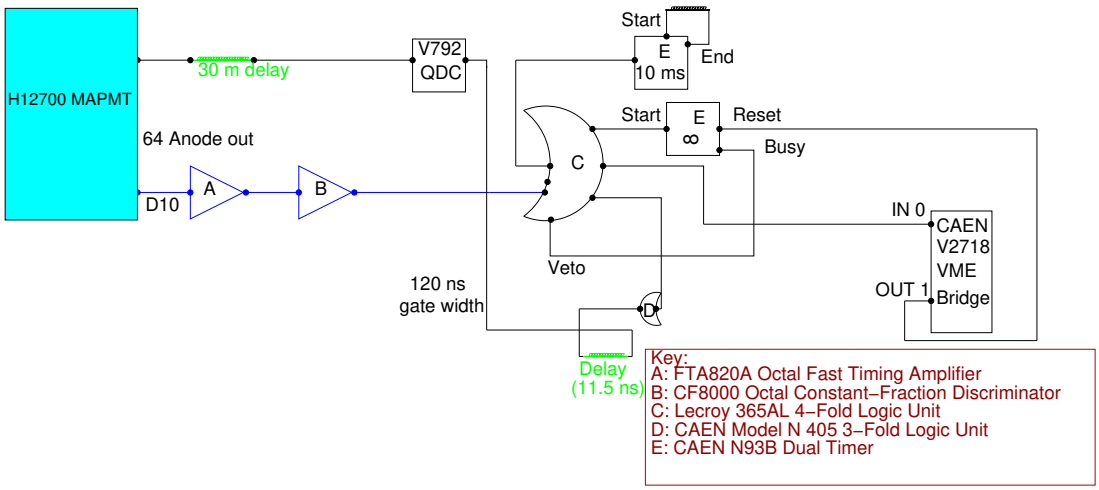

Figure 4.12: Diagram of circuitry used for alpha particle tests.

considered to be the coordinate origin point (0,0).

In parallel a Geant4 based simulation (as described in Sec. 4.2.1) was used to model the measured setup with alignment offsets accounted for. The measured and simulated data for each scan were run for approximately 10,000 events and are compared below in each section.

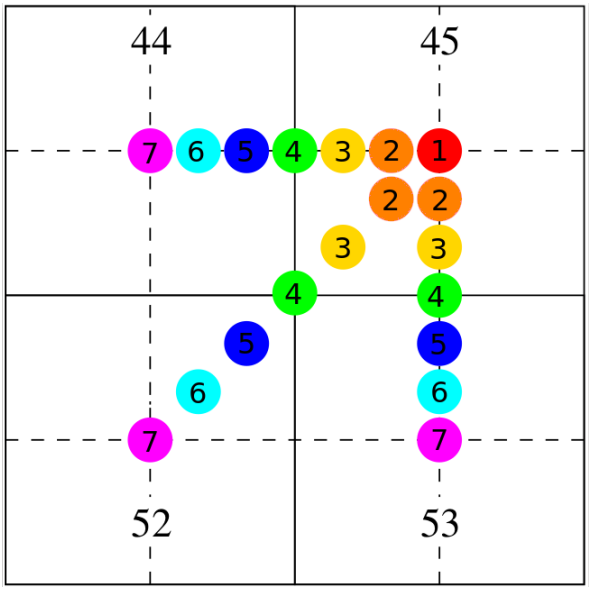

Figure 4.13: A representation of the mm separated scan positions for pixels 44, 45, 52, and 53.

4.4.2 Results

Horizontal Scan Results

The variation in signal amplitudes as the source was scanned horizontally across the face of the scintillator is plotted for pixels 44 and 45, the corresponding simulations shown in Figs. 4.14b and 4.14d. The measurements have been corrected for variations in pixel gains and normalised

to the number of detected photons predicted by the simulation. The mean values of the pulse height spectra, with associated errors, are given in Table 4.2. Fig. 4.15 plots the mean values and widths (standard deviation) of the spectra against the corresponding X-coordinate of the scan position.

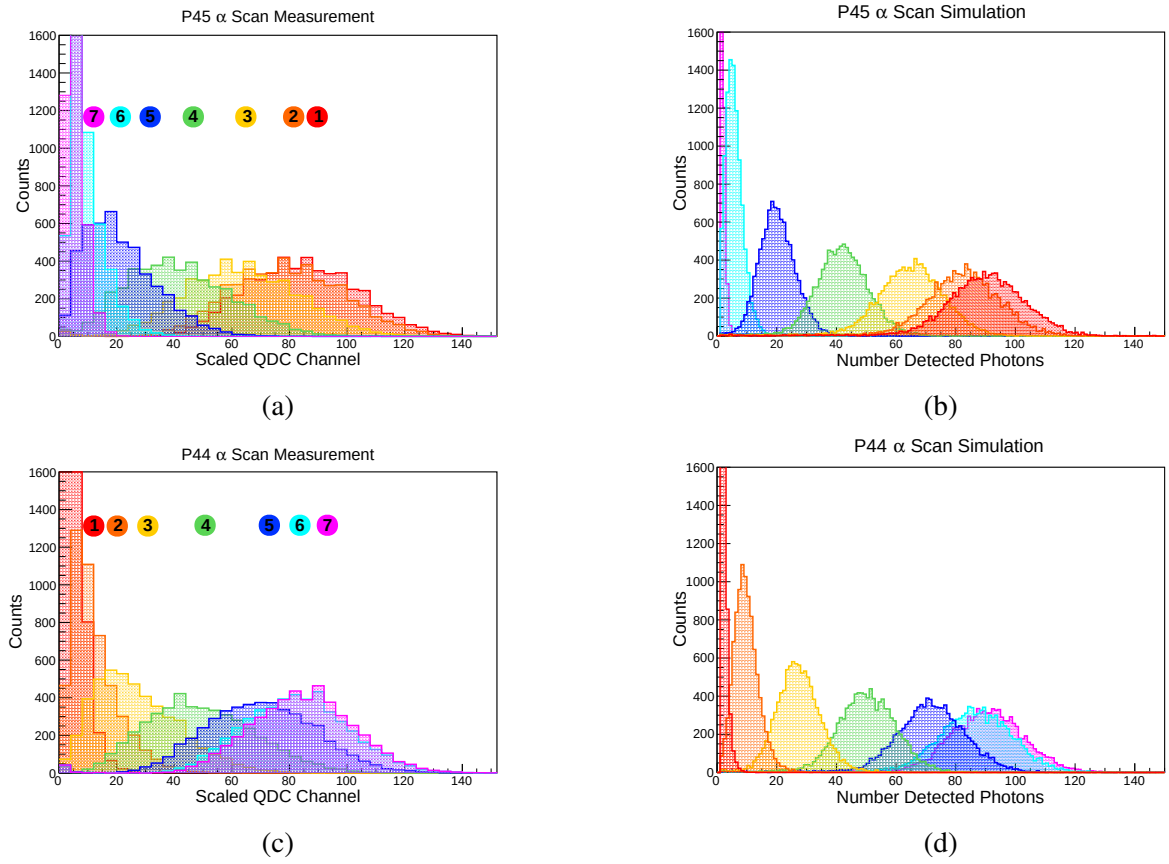

Figure 4.14: Comparison of measured and simulated horizontal scan data. The measured pulse heights are pixel-gain corrected and normalised to the number of detected photons calculated by the simulation. The numbered scan positions shown in (a) and (c) (similar to those in Fig. 4.13) coincide with the relevant spectra below.

Table 4.2: Mean (μ) number of photons with associated errors for positions 1-7 of pixels 45 and 44 for both measured and simulated alpha data.

P45			P44		
Pos	$\mu_{measurement}$	$\mu_{simulation}$	Pos	$\mu_{measurement}$	$\mu_{simulation}$
1	85.2 ± 0.3	89.7 ± 0.2	1	4.7 ± 0.1	1.9 ± 0.01
2	79.8 ± 0.3	86.0 ± 0.2	2	9.4 ± 0.2	5.9 ± 0.03
3	63.8 ± 0.3	71.7 ± 0.1	3	25.8 ± 0.3	20.3 ± 0.06
4	41.0 ± 0.3	50.2 ± 0.1	4	49.3 ± 0.3	42.0 ± 0.1
5	20.0 ± 0.2	27.3 ± 0.1	5	70.5 ± 0.3	64.9 ± 0.1
6	8.3 ± 0.1	9.8 ± 0.04	6	82.6 ± 0.3	82.1 ± 0.2
7	5.3 ± 0.05	2.3 ± 0.01	7	84.8 ± 0.3	90.0 ± 0.2

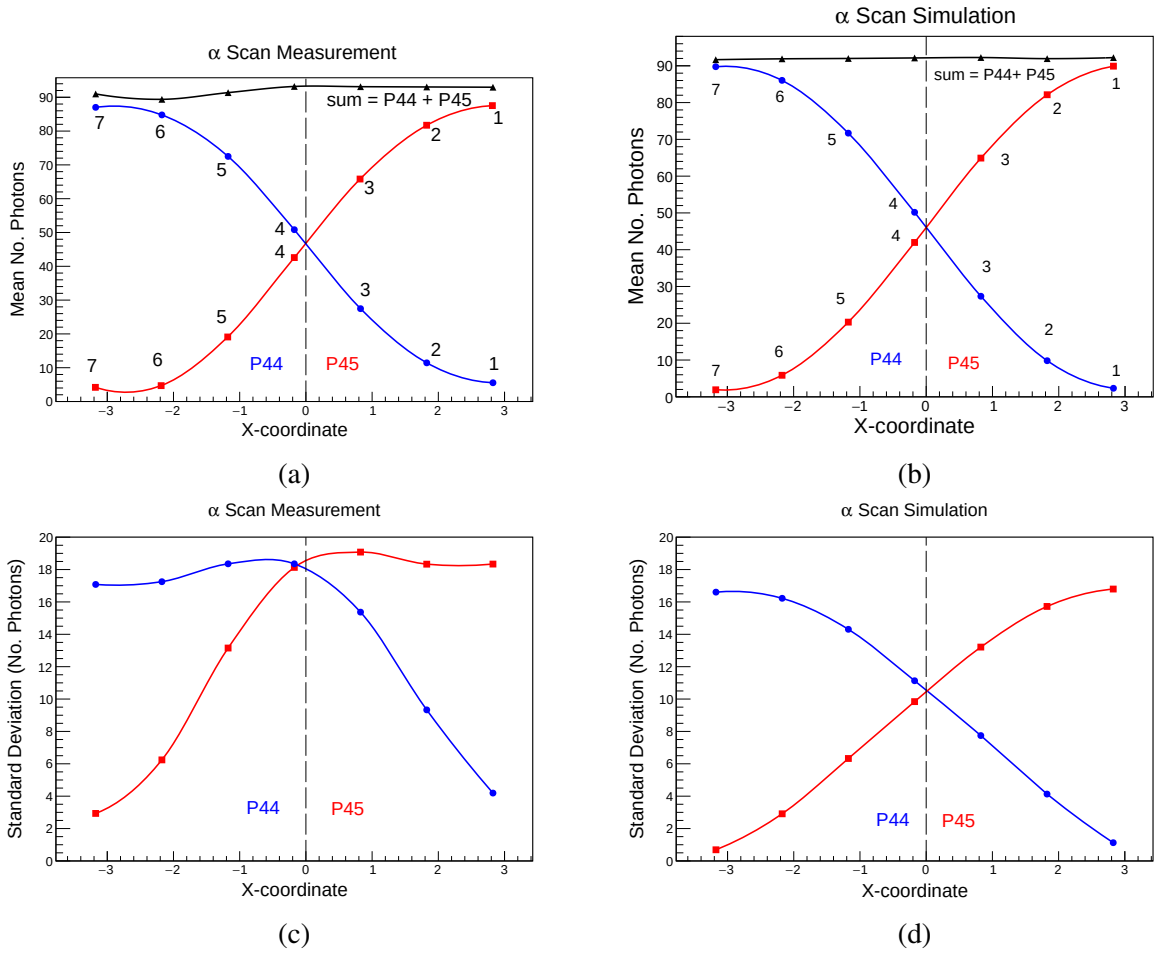

Figure 4.15: Measured and simulated horizontal mm scan data comparing mean number of detected photons and the standard deviation of the peaks. The numbers 1-7 correspond with the position of the scan at which the data were taken.

The signal amplitude drops as the source is moved away from the centre of the pixel, dropping from $\sim$ 85 detected photons at the pixel centre to $\sim$ 5 detected photons when the source is at the centre of the neighbouring pixel. Position '4' (green peak) of Fig. 4.14 was nominally at the inter-pixel boundary between pixels 44 and 45. The vertical black dashed line in Fig. 4.15 indicates the pixel boundary. It is assumed that equal number of photons will be detected in both pixels at the boundary. Therefore the boundary should lie at the intersection point of the spline fits to the distributions of pixels 44 and 45. The offset of position 4 from the pixel border was calculated as -0.175 mm, as shown in Fig. 4.15a.

The simulation assumes both pixels have equivalent gains and was run at scan positions offset by -0.175 mm from the nominal positions of the measurement. The simulation has a distinct similarity to the measured data as shown in Table 4.2, and is best highlighted in the comparison of the mean number of photons in Figs. 4.15a and 4.15b. The standard deviation results for the measured and simulated data differ significantly in Figs. 4.15c and 4.15d. The simulation does not account for electronic crosstalk in the dynode chains (optical crosstalk is

factored in), charge sharing between the anodes, or noise/pickup in the back-end electronics of the detector. Thus the simulation predicts more symmetric pulse height distributions with smaller widths compared to the measurements. The measured data peak towards the centre of the pixels are broader than the simulation peaks. As the source moves into the adjacent pixel there is a steep drop in the width (σ) of the peak due to the decreasing number of photons. The scattering of scintillation light within the GS20 from the point of ionisation may also have a larger effect than the simulation calculates. A small air gap, present between the GS20 scintillator and glass window of the MAPMT has been factored into the simulation. The air gap in fact reduces the spreading of light as it travels between the boundaries, as studied by Boyd *et al.* [110]. The simulation also assumes the polished finish of the GS20 scintillator is perfect, but a non-perfect finish will affect the reflection of light at the GS20 boundary. This is investigated in Sec. 6.3. The simulation also assumes a uniform photocathode sensitivity and homogeneous scintillation material, which if not the case could distort the measurements.

Vertical Scan Results

The vertical scan had an offset of -0.176 mm from the boundary between pixels 45 and 53, determined in the same manner as the horizontal data. The results for the vertical scan (Fig. 4.16) are similar to those of the horizontal (Fig. 4.15), a slight difference can be noted in the sum at the pixel boundary between 45 and 53 in Fig. 4.16a. Previously in Fig. 4.15 the sum of the mean number of photons for pixels 44 and 45 was consistently ~ 92, however when scanning in the vertical direction the sum of pixels 45 and 53 drops slightly as it approaches the boundary. A similar effect was noted for the Hamamatsu H8500 MAPMT model by R. Montgomery using a 635 nm laser at single PE level [104]. Charge sharing was stronger in horizontal directions in these devices due to dynode chain arrangements. This observed trend differs from the blue laser scans, wherein the mean number of photons increased at the vertical pixel boundary (Fig. 2.34). The laser data was taken with a focused laser beam without the presence of the GS20 scintillator, whereas the alpha data were taken with a collimated source and scintillator present. The added complexity of the system and variation in light transport may account for the observed differences. Therefore, the results are not fully comparable.

Diagonal Scan Results

The diagonal scan results (Fig. 4.17) are plotted against the X and Y-coordinates of the scan, and have the same X and Y offsets factored in as above. As the scan approaches the boundary between pixels 45 and 52 a larger dip in the 'summed mean' (black) appears. This effect is due to significant light spreading also to pixels 44 and 53. At the 'four pixel' boundary, one would expect an individual pixel to detect roughly a quarter of the total photons (~ 23), and for diagonally neighbouring pixels to see approximately 46 photons collectively. This is roughly what is observed in both the measured and simulated data (Figs.4.17a and 4.17b). Fig. 4.17c

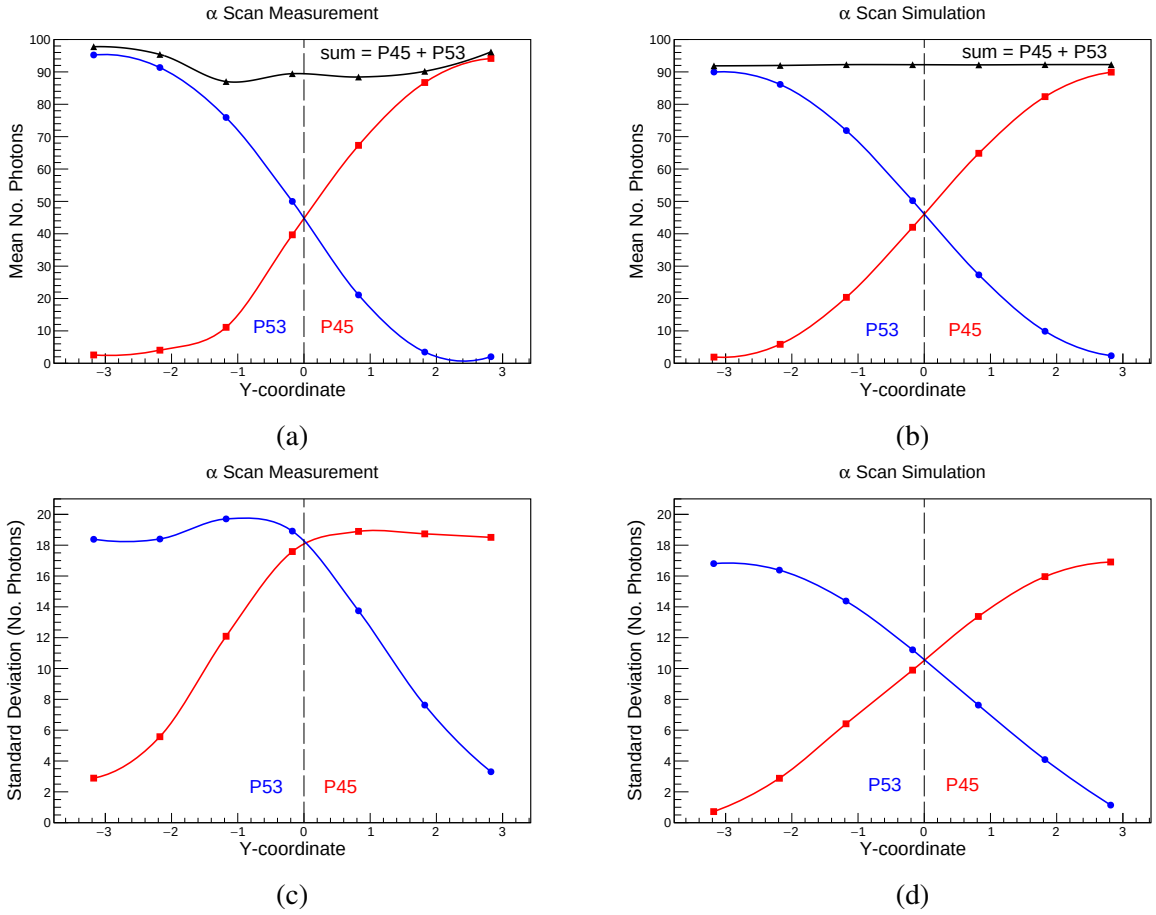

Figure 4.16: Measured and simulated vertical mm scan data comparing the mean number of detected photons and standard deviation.

shows a similar trend to the measured horizontal (Fig. 4.15a) and vertical (Fig. 4.16a) data in that the measured widths of the pulse height distributions are larger than the simulated widths.

Based on the measured data for the SoNDe Test Module, if a neutron capture event occurred at the boundary between two pixels the number of photons would be split approximately evenly between them. The portable IDEAS DAQ has the capability to set individual pixel thresholds to compensate for gain non-uniformities. This should in theory create a 'uniform' pixellated detector. The resolution of the MAPMT is affected by both electronic and optical crosstalk, charge sharing, and noise. The electronic contributions were not factored into the simulation leading it to underpredict the widths of the spectral distributions. However the results for the mean number of photons were generally in agreement.

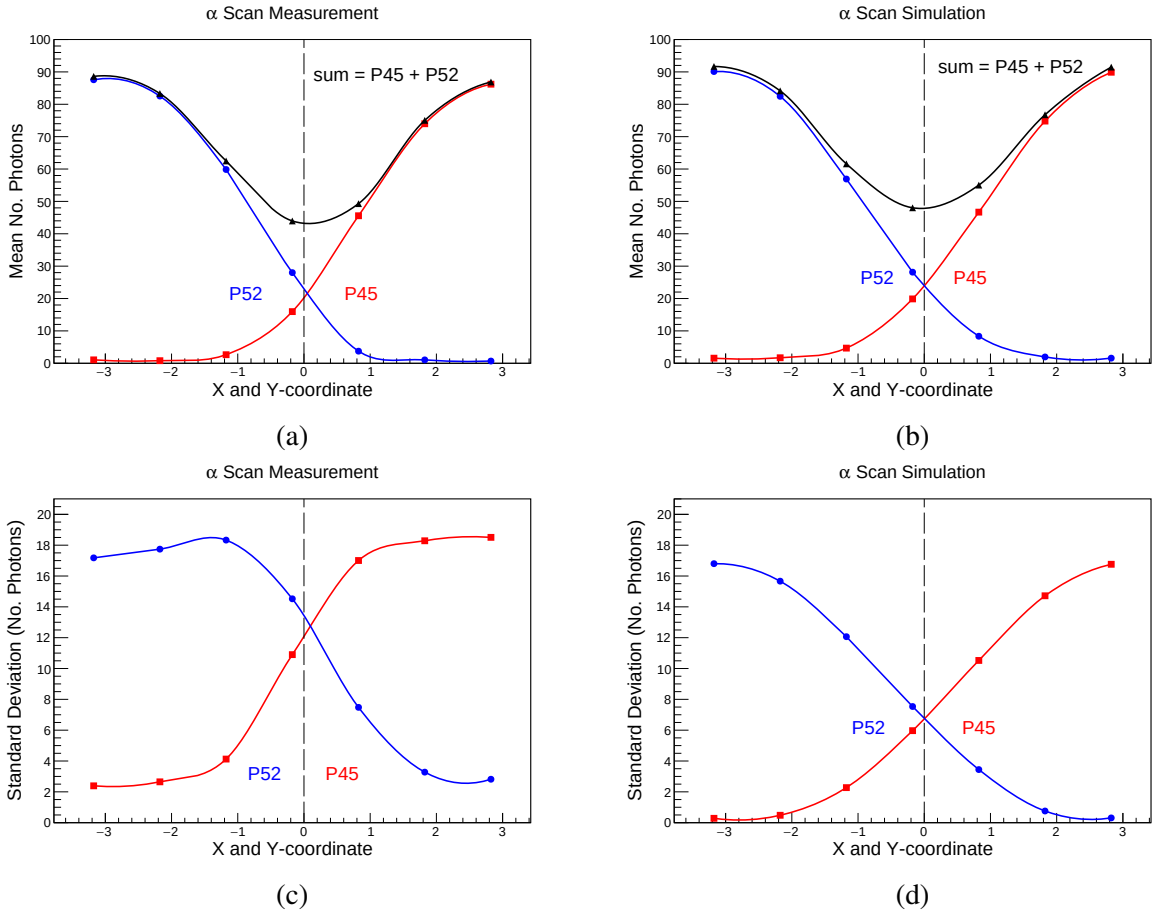

Figure 4.17: Measured and simulated diagonal mm scan data comparing mean number of detected photons and standard deviation.

4.5 Millimetre Stepped Scan of Detector Active Surface

The millimetre scan was extended to the full face of the SoNDe Test Module at -1000 V, using the 1 mm diameter collimated ^{241}Am alpha source with each position illuminated for $\sim$ 10,000 events. The results are shown in Fig. 4.18 with X and Y axes showing the scan coordinate in millimetres with the origin at the outside corner of pixel 1 (bottom left) of the MAPMT, and the Z-scale the pedestal subtracted amplitude in QDC bins. As used before in Sec. 2.2.3, the analysis takes the signal from the pixel which recorded the largest output at each scan position.

In comparison to the laser mm scan in Fig. 2.16, the pixel responses of the alpha scan appear as oblate circles as opposed to the semi-rectangular shapes of the laser scan. This effect is likely due to the spreading of scintillation photons due to the ionisation events caused by the alpha particles. The alpha mm scan gives a clear indication as to where the four-pixel intersection points are located (dark blue). These areas are similar in location to the multiplicity M = 3 regions shown in Fig. 4.19, these regions appear less responsive. The mm scan shows a similar trend in relative pixel gains to both the Hamamatsu relative gain map (Fig. 2.4) and the -1000 V alpha gain map in Fig. 4.8.

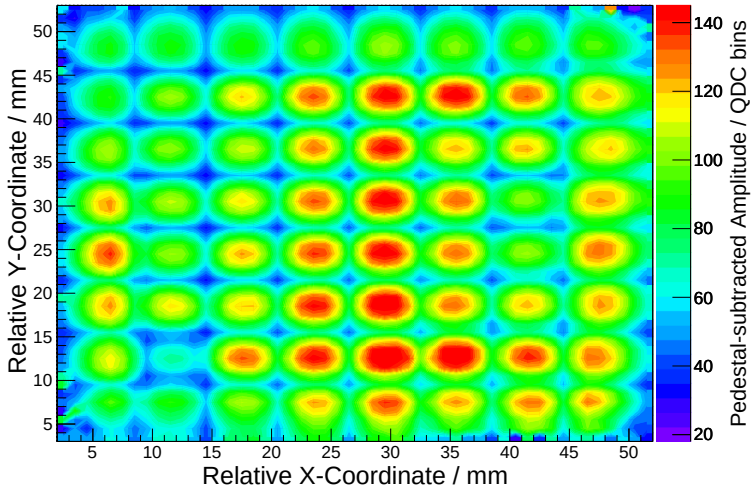

Figure 4.18: Millimetre stepped scan across the detector face of the SoNDe Test Module using a collimated ^{241}Am source. The Z-scale indicates the difference between the alpha signal peak and pedestal peak in QDC bins. Pixel boundaries (dark blue) and 'hot' spots (red) are clearly visible.

4.6 Multiplicity

Multiplicity is defined as the number of pixels which record a signal above a set threshold in the course of a single event. One can choose to allow or disallow the recording of these events.

Two dimensional position maps of multiplicity (M = 1, 2, 3), derived from the alpha-scan data, are displayed in Fig. 4.19 [108] for different threshold settings. The study was performed with a nominally identical SoNDe Test Module with an H12700A MAPMT S/N ZA0250 and a similar sheet of GS20 scintillator. A 10 $\times$ 10 mm^2 area was scanned in mm steps with 2000 events recorded per position. The number-of-multiplicity-events key is represented in (a), while plots (b), (c), (d) display multiplicity maps for thresholds of 100, 235 and 500 QDC channels respectively.

For a low discriminator threshold, multiplicity 2 and 3 events dominate the edges and corners of P37 with M = 1 events confined to the centre. Multiplicity M = 4 and higher only becomes significant at thresholds lower than 100 channels. Multiplicity 3 events do not show up on the results at higher discrimination levels as their pulse heights are much lower due to photon sharing at the four pixel boundary. The M = 2 events are dramatically decreased at the 235 QDC channel threshold and appear predominantly at the horizontal pixel boundaries, consistent with increased electronic crosstalk across horizontal pixel boundaries. Further increasing the threshold to 500 QDC channels limits the user to M = 1 events only and creates 'dead spaces' within the detector (areas where zero hits are registered). Initially it was envisaged that SoNDe data would be analysed to maximise M = 1 contributions (threshold 235 channels). Higher thresholds eliminate M > 1 events at the expense of a large drop in detection efficiency. However

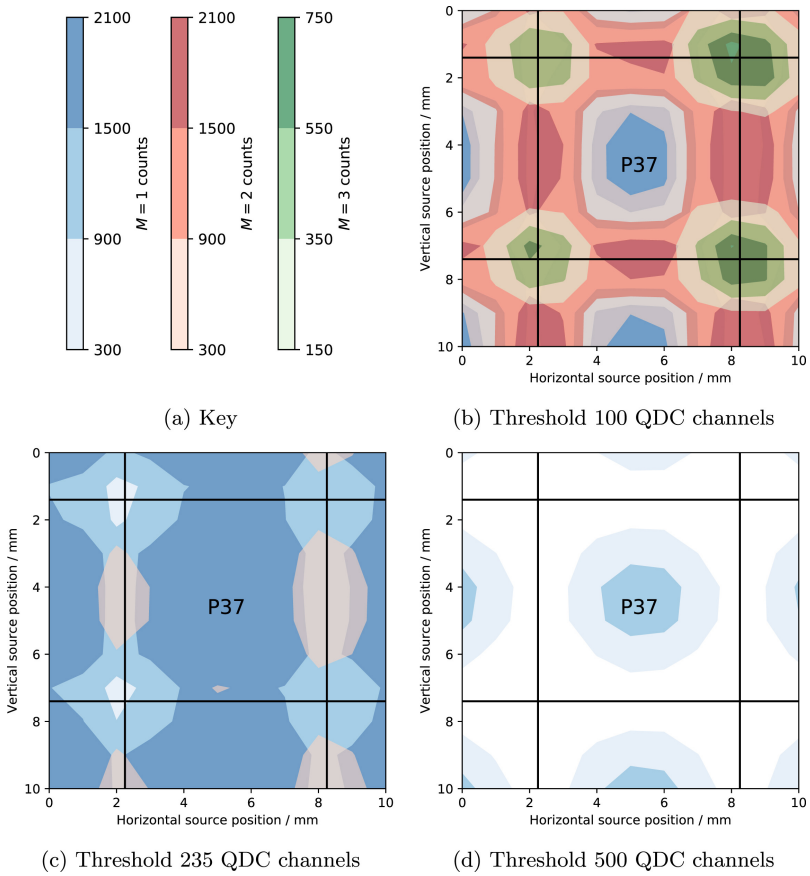

(a) Key

(b) Threshold 100 QDC channels

(c) Threshold 235 QDC channels

(d) Threshold 500 QDC channels

Figure 4.19: Variation in multiplicity with discriminator threshold as a function of position for P37 and adjacent pixels using a collimated alpha source. The key in (a) indicates the multiplicity type, 1 = blue, 2 = red, and 3 = green, with varying numbers of events based on the colour gradient (lighter = fewer events). The horizontal and vertical lines of plots (b) - (d) represent the pixel boundaries surrounding P37 and the QDC threshold values used are labelled beneath each plot. Image taken from [108].

M > 1 events are useful as they provide the means to achieve improved position resolution.

4.7 Crosstalk Measurements

Crosstalk measurements were performed on an unmasked SoNDe Test Module at -1000 V for a 1 mm diameter collimated alpha source centred on P45. The results for the 24 pixels surrounding the target are shown in Fig. 4.20 and were obtained using the same analysis method as described in Sec. 2.2.6 and Fig. 2.27.

The alpha results show crosstalk levels on average a factor $\sim$ 4.6 greater in comparison to the P45 laser crosstalk values at a light level of 60 PEs. Most of this increase is due to the spread of scintillation photons within the GS20 glass. As was explored in Sec. 3.1.2, the use of a pixellated scintillator would increase the efficiency of the detector, however introducing such grooves would compromise the true-to-false ratio and increase the displacement of photons from the generation point. Again, the solution here would be to set an appropriate discriminator

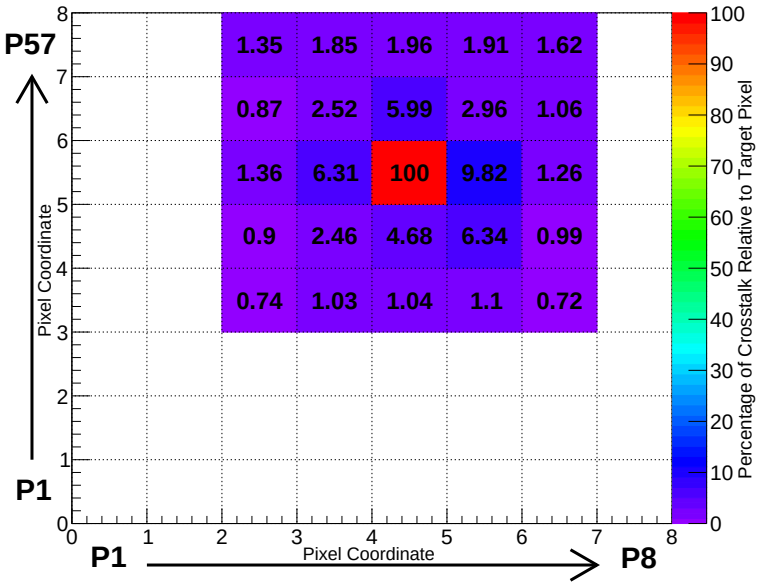

Figure 4.20: Measured crosstalk values for target pixel P45 and the surrounding 24 pixels, measured using a 1 mm diameter collimated alpha source.

threshold and multiplicity analysis cut so as to reduce the effects of optical crosstalk.

4.8 Summary

The energy spectrum from a ^{241}Am alpha source was measured using a PIPS detector in vacuum and calibrated against a triple-nuclide alpha source. The energy loss of alpha particles in air, calculated in the Geant4 simulation to be $\sim$ 270 keV on average, reduced the energy at incidence on the GS20 sheet to $\sim$ 4.27 MeV average.

A system stability test was performed using the collimated alpha source. An overall drift of 2.93×10^{-4} %/hr was recorded (Fig. 4.6). Both the alpha and laser data display a drift of the order 10^{-4} %/hr.

The gain versus high voltage variation (Fig. 4.7) showed a non-linear correlation consistent with Eq. 4.10. However for the present application -1000 V should be a sufficiently high voltage. The relative gain variations per pixel were mapped for the SoNDe Test Module at both -1000 V and -1150 V to test the relative gain variation as the high voltage is increased. Both results proved similar to the data provided by Hamamatsu, and show that any differences in the dependence of individual pixel gain on high voltage are small.

The relative width of the Glasgow ^{241}Am source for the SoNDe Test Module was R = 0.51 (51%), compared to the intrinsic width R = 0.11 (11%) measured by the PIPS detector. The SoNDe module will not be used for spectroscopy, and can therefore operate with a poorer detector resolution. However, the detector may struggle with a broader neutron capture peak as more

background (continuum) can hide under it.

Pulse height was measured as the collimated alpha source was scanned horizontally, vertically and diagonally across a set of 4 detector pixels. The number of photons produced for an event occurring at a pixel boundary was approximately evenly split between both pixels (Figs. 4.15 and 4.16). The same could be said for a four pixel intersection (Fig. 4.17). The trend in mean number of photons for the measured and simulated scanned data was largely in agreement (Table 4.2), verifying the Geant4 based simulation. A discrepancy however in peak widths suggest the need for electronic crosstalk and noise contributions to be factored into the simulation for future studies (see Sec. 6.3).

The pixel multiplicity analysis for different pulse-height thresholds from the study in Ref. [108] was shown to alter the active area of the detector by creating 'dead spaces' and regions of increased multiplicity (Fig. 4.19). The analysis was initially performed to determine the conditions to maximise the M = 1 contributions. This led to a drop in detector efficiency and useful event information (M > 1) used to achieve an improved position resolution was being lost. Setting the correct discriminator threshold for multiplicity will vary from pixel to pixel. The portable IDEAS DAQ software has the ability to set each pixel manually.

The millimetre stepped scan of the SoNDe Test Module detector face indicated that the spread of scintillation photons from their point of origin throughout the GS20 as a result of the alpha ionisation events affected the resolvability of the individual pixels. This effect was seen more clearly in the crosstalk measurements. These were on average a factor of ~ 4.6 greater than those performed with the 404 nm laser. The spread or photons could be used to improve the position resolution of the detector by employing a suitably low discriminator threshold and performing a multiplicity analysis. This method will be used when the SoNDe modules are implemented at the ESS.

With the detector response to ionising alpha radiation understood, it was time to test its response to thermal neutrons and other sources of potential background.

Chapter 5

Neutron Irradiations of Detector

5.1 Motivation and Source Properties

The collimated laser and alpha-particle scans provided precision data which uncovered the detailed response of the detector. The ultimate goal of the SoNDe Module is to detect scattered thermal neutrons and therefore the detector's response to thermal neutrons and ability to clearly resolve a thermal neutron signal must be tested. Close to thermal neutrons can be effectively produced by moderating a fast neutron source with a hydro-carbon material, e.g. polyethylene. However, one cannot achieve a purely mono-energetic source using this method and a range of neutron energies will remain present. The fast neutrons from the source scatter off the hydrogen and carbon atoms within the moderator and lose energy. The interaction can be viewed on both a microscopic and macroscopic level. The microscopic cross-section characterises the probability of a neutron interacting with a target nucleus and is generally expressed in barns (10^{-28} m^2). The macroscopic cross-section represents the probability of an interaction taking place across all the nuclei contained within a volume of material and in this instance is given in units of m^{-1}. Each element within the material has its own macroscopic cross-section. The relationship between the macroscopic (Σ) and microscopic (σ) cross-sections for a mixed material is given by the equation [124]

$$\Sigma = \sum_i \sigma_i N_i, \tag{5.1}$$

where N_i is the nuclei density of the element (nuclei/m^3). The total macroscopic cross-section (Σ_t) for a neutron moderator with neutron absorption is given by

$$\Sigma_t = \Sigma_s + \Sigma_a, \tag{5.2}$$

where Σ_s is the macroscopic scattering cross-section of the medium ($\Sigma_s = \Sigma_{el} + \Sigma_{in}$) composed of the elastic (*el*) and inelastic (*in*) scattering components, and Σ_a is the macroscopic absorption cross-section of the medium. A full analytical derivation of neutron moderation may be found

in Rusov *et al.* [125].

Neutron sources moderated with polyethylene produce thermal neutrons, however a background of fast neutrons and gamma-rays will remain present. It is important to measure fast neutron and gamma response as these will constitute the main background of the SKADI instrument. The Lund Source Testing Facility houses several neutron sources, AmBe, PuBe and ^{252}Cf, as well as an array of gamma sources. The AmBe source was used for all of the neutron measurements, both fast and thermal, and ^{60}Co was used for gamma-ray calibration.

5.1.1 Neutron Source Production

In order to create a neutron emitting source, powdered ^{241}Am is mixed, evaporated and fired with ^{9}Be and then pressed into pellets. These pellets are encased in stainless steel and stored in paraffin wax or other hydro-carbon materials for safe keeping [126]. A concern with α-Be sources is the build-up of pressure caused by helium production. (α,n) sources rely upon the following interaction,

$$^{9}\mathrm{Be} + \alpha \rightarrow ^{12}\mathrm{C} + \mathrm{n} + \gamma \ \ (4.44 \ \ \mathrm{MeV}). \tag{5.3}$$

AmBe has an approximate yield of 5.4 - 6.5 $\times$ 10^4 neutrons/s per GBq of primary alpha yield (actual yield is dependent on source construction and ^{241}Am / ^{9}Be ratio). The Lund AmBe source has an approximate flux into 4π of 1.14 $\times$ 10^6 neutrons/s [127]. According to the ISO 8529-2 standard the average neutron energy is $\sim$ 4.2 MeV with a maximum of 11 MeV as shown in Fig. 5.1, and the Lund AmBe source was expected to have a similar energy spectrum [128]. Photo-neutron sources (γ + ^{9}Be $\rightarrow$ ^{8}Be + n), employing gamma-ray emitters such as ^{24}Na and ^{124}Sb, have the advantage of producing quasi monoenergetic neutrons (800 keV and 24 keV respectively). The emitted gammas are energetic enough to overcome the neutron binding energy of ^{9}Be. The source half-life of both isotopes (15 h and 60 d respectively) [129] is short in comparison to ^{241}Am (432 y) [130], meaning the usable lifetime and strength of these sources will deplete more rapidly than the ^{241}Am source. In order to increase the thermal neutron flux relative to background the AmBe source was placed behind 50 mm of polyethylene moderator and shielded with 20 mm of Pb. The moderated, uncollimated neutron energy spectrum for a similar SoNDe module was compared with a 2.4 Å, 3 mm diameter collimated neutron beam at the IFE (Institute for Energy Technology, Norway) [131]. The results confirmed that a similar energy spectrum was achievable using the moderated AmBe source (Fig. 5.2). The moderated neutron source was uncollimated. Therefore the full detector is irradiated with neutrons.

As discussed in Sec. 3.1.1, the Geant4 based simulation was extended to include gamma radiation, thermal neutrons, and fast neutrons. The response of the detector to these forms of radiation was directly compared with the measured data.

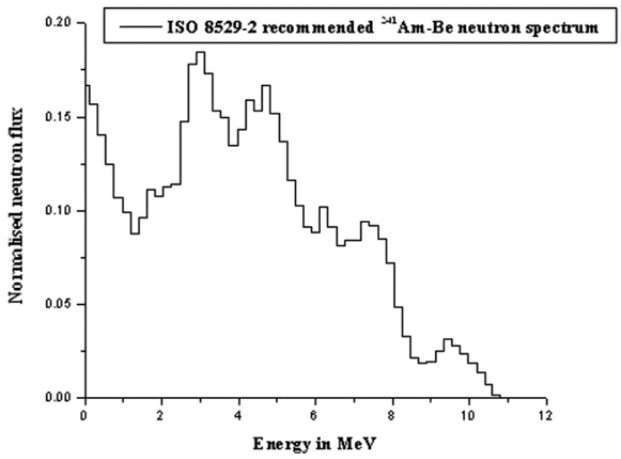

Figure 5.1: AmBe source spectrum according to ISO 8529-2 standard. Image taken from [132]

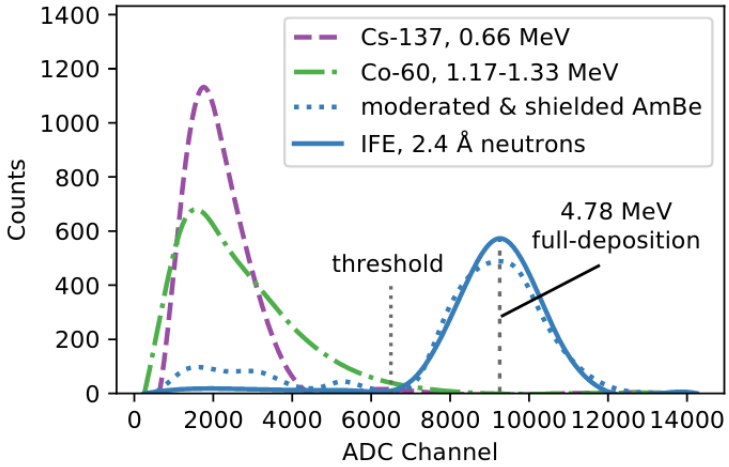

Figure 5.2: The 2.4 Å neutron spectrum (solid blue line) taken with the Lund University SoNDe module (with the IDEAS DAQ). The spectrum has a similar peak shape and width to the moderated and shielded AmBe neutrons (dashed blue line) used at the Lund STF. Image taken from [131].

5.2 Laboratory Setup

The lab setup and data acquisition system at the Lund Source Testing Facility are quite similar to those at the University of Glasgow. The detector was housed in a light-tight black box for all the measurements. The signal cables were fed into a Cerberus splitter board [133] designed to split the signal from the MAPMT, to be read out simultaneously by the VME based DAQ and the IDEAS portable DAQ for a direct comparison. A schematic circuit diagram is shown in Fig. 5.3. The circuit also includes adjustments (red) made for the proton beam studies that are discussed in Sec. 6.1. A screen capture, taken from an oscilloscope, of the SoNDe Test Module's response to a ^{228}Th alpha-source is shown in Fig. 5.4. The yellow represents the amplified and inverted dynode 10 signal (OR of all signals) on a scale of 50 mV/div, the green signal represents the anode signal from P45 at the input to the V792 QDC at 5 mV/div, and the blue signal is taken

from the QUAD coincidence logic unit (used to set the gate width) before it is delayed. The NIM-logic QDC gate signal from the OR module was shaped to be 160 ns long and delayed so that the leading edge came $\sim$ 20 ns before the start of an anode signal at a QDC input. The 20 ns allows the gate circuitry to open fully.

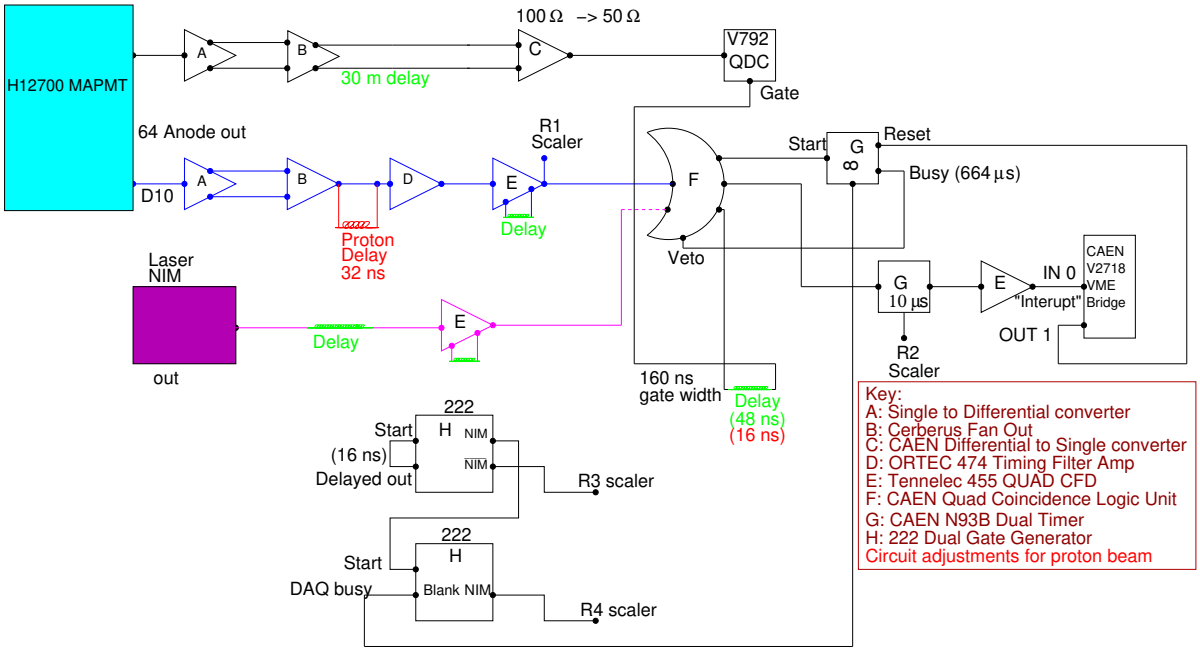

Figure 5.3: Electronic circuit for neutron and gamma-ray measurements. The circuit includes a Cerberus splitter board, a scalar counter and adjustments for proton beam experiments (red).

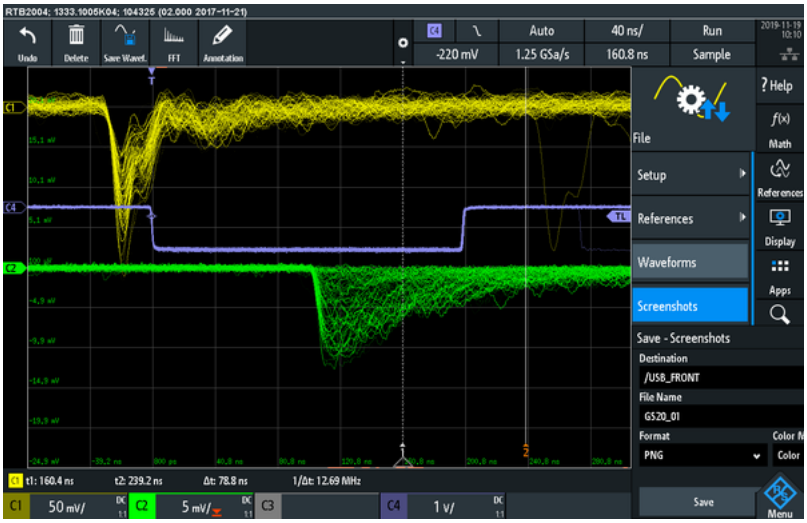

Figure 5.4: A screen shot from the oscilloscope used to measure the QDC gate width before delay (blue, middle). The signal taken from the Quad Coincidence Logic unit measured 160 ns and was required to register the MAPMT signal taken from a single pixel (green, bottom). The inverted dynode 10 signal is shown at the top in yellow. The horizontal time base scale is 40 ns per division.

5.2.1 Energy Calibration of MAPMT Detector with ^{60}Co

The response of the detector[1] was calibrated using a ^{60}Co source. ^{60}Co decays via β^- radiation at two separate energies, β_1 = 0.31 MeV (99.88%) and β_2 = 1.48 MeV (0.12%) leaving ^{60}Ni* isomers. The ^{60}Ni* de-excites by emitting gamma rays of energies γ_1 = 1.1732 MeV and γ_2 = 1.3325 MeV. Examples of ^{60}Co spectra from the NaI(Tl) and HPGe detectors are shown below in Fig. 5.5. The energy resolution of the HPGe solid state detector is superior to the NaI scintillator as indicated by the width of the photopeaks. The distinctive photo peaks of ^{60}Co (as well as its Compton edges and back scatter peaks) are commonly used to calibrate radiation detectors. GS20 scintillation glass is sensitive to gamma radiation, therefore one can use this source to calibrate the detector. The response for P45 shown in blue in Fig. 5.6.

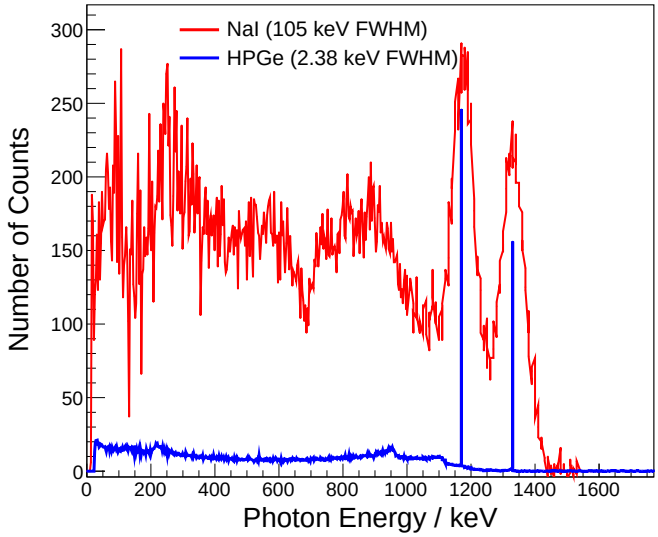

Figure 5.5: Examples of the responses of a NaI detector (red) and a HPGe detector (blue) to ^{60}Co gamma radiation.

The resolution of the SoNDe Test Module to gamma-radiation is much poorer than that of the NaI and HPGe. The SoNDe Test Module is unable to resolve the photopeaks due to the GS20 scintillation glass's low Z-element composition, leaving little to no photoelectric cross-section for gamma rays [61]. The contributions from the Compton electrons would normally leave a single broad shoulder, however in this case only a small number of Compton electrons were recorded. The maximum energy of the Compton edge occurs when the recoil angle approaches 180° and is estimated as

$$E_{Compton} = E\left(1 - \frac{1}{1 + \frac{2E}{m_e c^2}}\right), \tag{5.4}$$

where E is the energy of the incident gamma ray photon, m_e is the mass of the electron, and c is the speed of light. A mean incident gamma energy of $E = \frac{1.17+1.33}{2}$ = 1.25 MeV was used

[1] H12700 MAPMT S/N LA0125

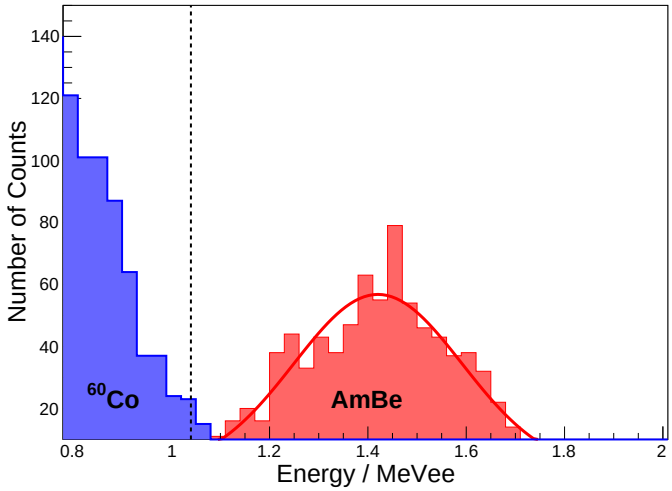

Figure 5.6: The edge of the ^{60}Co spectrum (blue) marked by a black dashed line relative to the AmBe neutron capture peak (red) measured in MeVee.

giving $E_{Compton}$ = 1.04 MeV, indicated by the black dashed line in Fig. 5.6. The edge of the ^{60}Co spectrum is difficult to determine since very few $\sim$ 1 MeV electrons stop in the thin GS20 sheet.

The simulation, which recorded both the actual energy deposit in the scintillator and the resultant number of detected scintillation photons was useful in this respect. This calibration gives the neutron signal energy in units of MeVee, Mega Electron Volts Electron Equivalent (Fig. 5.6 red). 1 MeVee is the equivalent signal that a 1 MeV electron gives if it stops in the scintillator. From this calibration the moderated neutron source energy was estimated as 1.42 ± 0.14 MeVee, compared to a value of 1.60 ± 0.09 MeV determined for thermal neutrons measured with GS20 ($10 \times 10 \times 5$ mm^3) at room temperature [134]. Most of the uncertainty in the present calibration arises from the uncertainty in determining the position of the Compton edge. Plainly the triton and alpha (total energy 4.78 MeV) produce much less light per unit energy deposited than electrons.

5.3 Measured Response of the Detector

The response of the SoNDe Test Module to moderated neutrons was measured as described in Sec. 5.2. The 64 pixel response is shown in Fig. 5.7. The spectra in the pixels around the edge of the detector do not have a distinctive neutron peak in comparison with the central pixels (outlined in blue). This is a result of light loss along the edges of the GS20 scintillator and the analysis cuts used to achieve the neutron peaks. The multiplicity (number of pixels which simultaneously register a signal above a certain threshold per individual event, Sec. 4.6) was set to M = 1 for the data, meaning events where a photon was detected in multiple pixels were

discounted, and only single pixel events were recorded. The edge pixels have five neighbouring pixels (three neighbours for pixels located in the corners) in comparison with the central pixels which have eight neighbours (adjacent and diagonal). This effectively means that the single-pixel condition is less effective at selecting events close to the centre of the pixel, i.e M = 1 events will be less localised (Fig. 4.19) for edge pixels and will produce a 'smudged' pulse height distribution. The central 36 pixels have a well-defined valley between the gamma/fast neutron background and the neutron-capture peak.

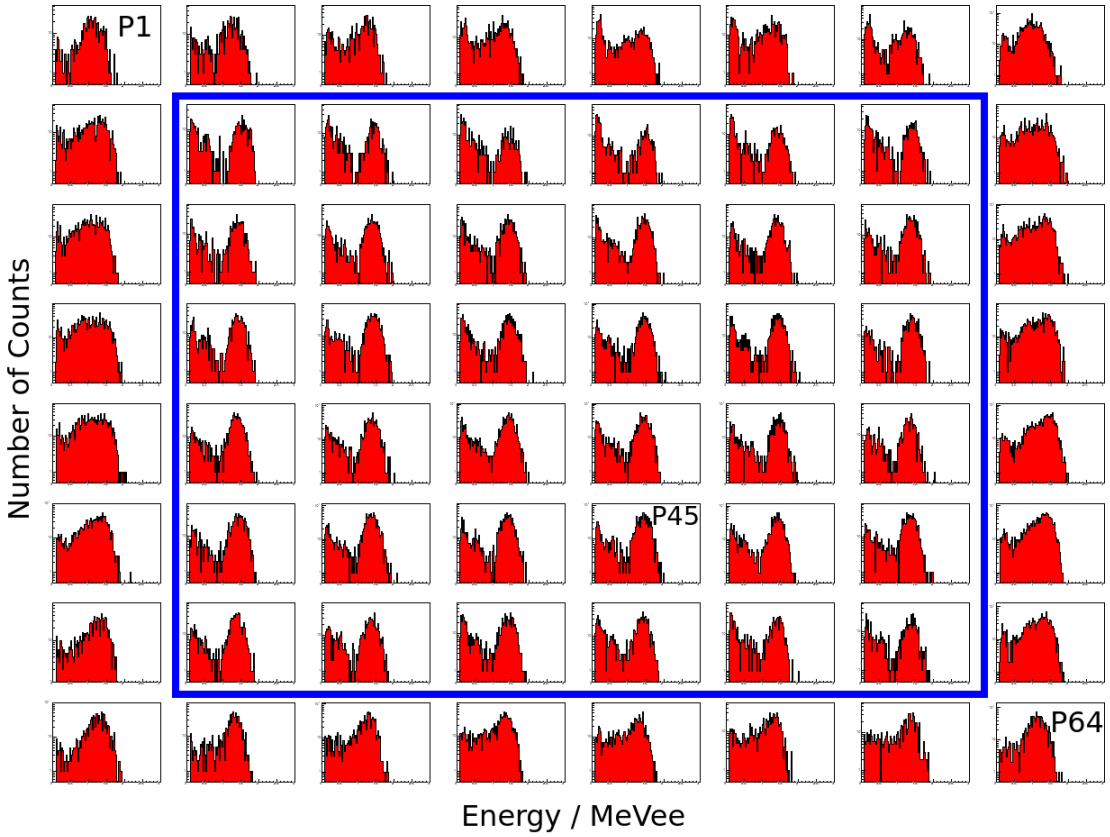

Figure 5.7: Full SoNDe Test Module response to the moderated AmBe source. P1 is located top left, P45 in the central 36 pixels outlined in blue, and P64 bottom right. The X-axes are in MeVee between 0 - 3 and the Y-axes in a log scale for the number of counts.

5.4 Simulated Response of the Detector

The expected neutron background spectrum at ESS will be comprised of low to high energy neutrons. These have been simulated for fast neutrons between 0.1 MeV to 100 MeV and are compared to the thermal (0.025 eV) response of the detector in Fig. 5.8a. The signal is reconstructed from a nine-pixel cluster sum centred on P45 in units of number of detected scintillation photons (signal amplitude). The thermal neutrons were simulated for 5×10^3 events and the fast neutrons for 2×10^6 events since the detection efficiency for thermal neutrons is very much

larger. Low-energy fast neutrons (< 1 MeV) may be captured by the ^{6}Li, but not as readily as the moderated neutrons due to a lower absorption cross-section. Medium energy fast neutrons will deposit their energy via inelastic scattering. High energy fast neutrons (> 10 MeV) can fragment the nuclei within the scintillator glass e.g. (n,p), (n,α), or (n,2n) reactions, which produces a continuum in the energy spectrum.

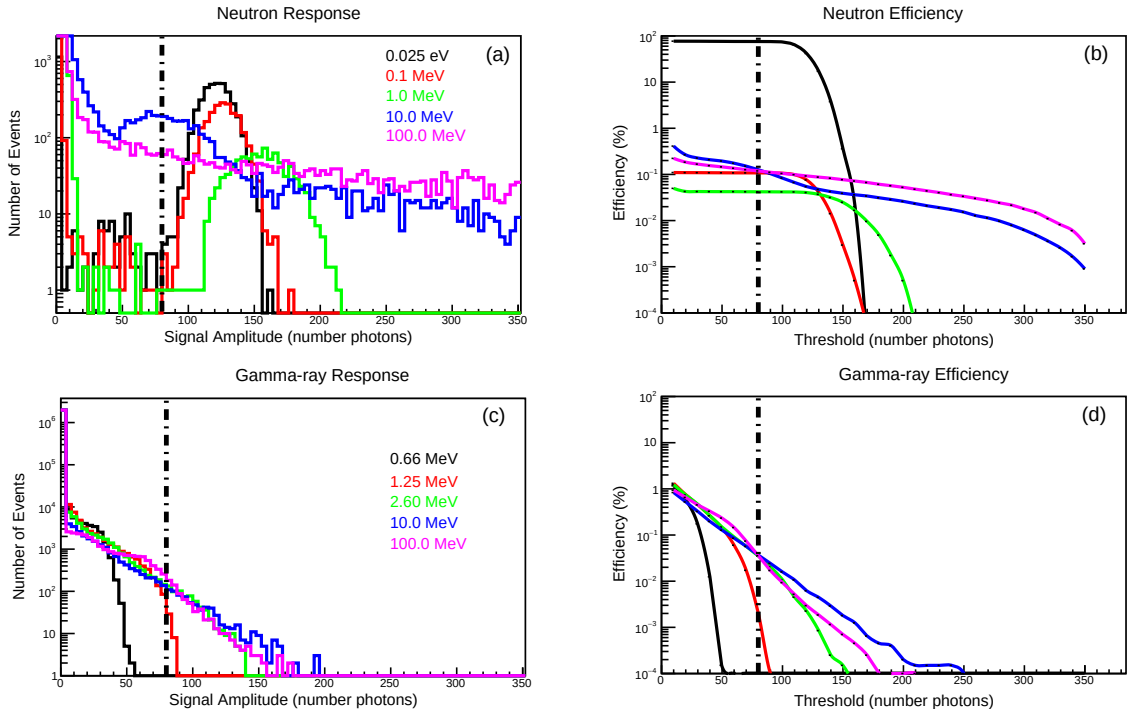

Figure 5.8: Simulated response of the detector to (a) Neutrons of finite energies ranging from 0.025 eV to 100.0 MeV expressed as signal amplitude in the number of detected photons. (b) The efficiency of thermal and fast neutrons as a function of threshold with the same colour coding to plot (a). (c) Gamma radiation ranging from 0.66 MeV to 100.0 MeV expressed as signal amplitude. (d) The gamma-ray efficiency as a function of threshold with the same colour coding to plot (c). The dashed line represents the 80 photon threshold. The thermal neutron results were generated from 5×10^3 incident particles, and the rest from 2×10^6 incident particles. Image taken from [110].

A simulated response of the detector to gamma-ray energies from 0.66 MeV to 100 MeV (representing the potential gamma background of the SKADI instrument) for 2×10^6 incident particle events, is shown in Fig. 5.8c. The signal is obtained via the same nine-pixel cluster sum as the neutron data. The lower energy gammas ($\sim$ 1 MeV) show a diffuse Compton edge, whereas the secondary electrons produced from the higher energy gamma interactions (Compton and pair production) are too energetic and deposit less energy passing through the 'low Z' scintillation glass, producing similar distributions from 2.6 to 100 MeV. The secondary electrons become more focused kinematically along their incident gamma-ray path with increasing energy. This lack of dispersion leads to a decrease in the amount of GS20 traversed, and therefore a reduction in signal amplitude. The 10 MeV gamma-ray spectrum has an increased amplitude

within the 120 - 200 photon range in comparison to the 100 MeV gamma-ray spectrum.

The neutron and gamma detection efficiency (η_d) is displayed as a function of threshold in Figs. 5.8b and 5.8d respectively. The detection efficiency is defined as the ratio of integrated counts above threshold to the total number of incident neutrons/gammas. For neutrons, a threshold of 80-photons provides a thermal neutron detection efficiency $\eta_d \sim 76\%$, with some limited suppression of fast neutrons (> 0.1 MeV). For gamma radiation the 80-photon threshold completely removes the ^{137}Cs (0.66 MeV) signal, whilst almost completely suppressing the ^{60}Co (1.25 MeV) signal, η_d = 0.002%. Highly effective suppression is achieved for gamma energies $\geq$ 2.60 MeV. The detection efficiency results for a range of neutron and gamma energies is shown in Table 5.1.

Table 5.1: Detection efficiency for neutron and gamma-rays at a threshold of 80-photons. Table taken from [110].

Neutron Energy	η_d (%)	Gamma Energy	η_d (%)
0.025 eV	75.8	0.66 MeV	0.0
0.1 MeV	0.108	1.25 MeV	0.002
1.0 MeV	0.042	2.60 MeV	0.035
10.0 MeV	0.127	10.0 MeV	0.037
100.0 MeV	0.119	100.0 MeV	0.036

The simulation results indicate a thermal neutron detection efficiency of almost 80% with a desired low gamma efficiency, as stipulated by the detector requirements.

5.5 Comparison

The response of the detector was directly compared with the simulated data. The simulation produces the neutron response in units of the number of detected photons. The measured data was normalised to the simulation, i.e $\sim$ 1.42 MeVee (from Fig. 5.6) is equivalent to $\sim$ 121.2 (Fig. 5.8a) detected photons for moderated neutrons. The comparison of the nine pixel cluster sums centred on P45 for the measured and simulated data are shown in Fig. 5.9.

When fitted as a Gaussian distribution the measured and simulated data peaks have means equivalent to 121.2 detected photons and standard deviations of $\sigma_{measured}$ = 14.8 Scaled QDC Channels (equivalent to the number of detected photons) and σ_{sim} = 11.1 detected photons. The neutrons used for the measured data were moderated, i.e. not from a mono-energetic source, as was used in the simulation (0.025 eV). However, the similarity of moderated-source and reactor beam measurements in Fig. 5.2 suggests that the increased width of the measured capture peak (Fig. 5.9a compared to simulated Fig. 5.9b) may be due to electronic noise which is not factored into the simulation.

The equivalent number of detected photons of the ^{60}Co Compton edge is found using the MeVee-to-photons conversion factor. Where $E_{Compton}$ = 1.04 MeV, the number of detected pho-

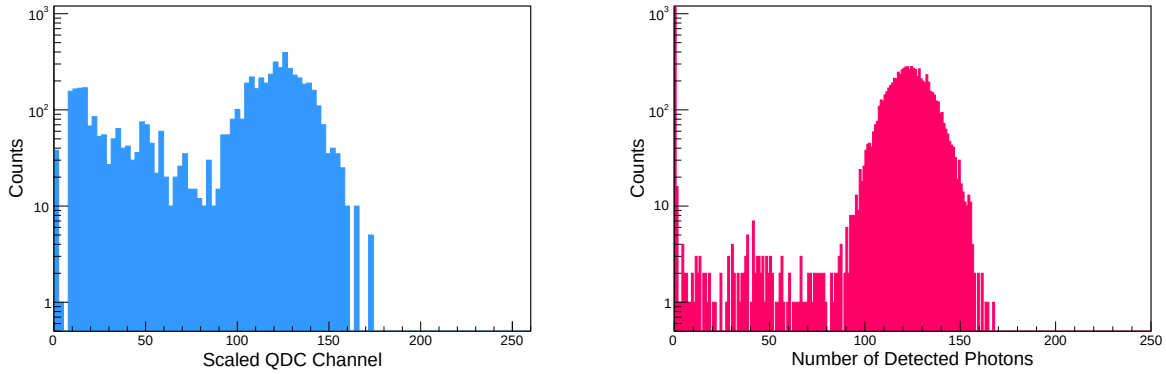

(a) (b)

Figure 5.9: Comparison of measured moderated neutron data normalised to the number of detected photons (left) to the simulated detector response to a thermal neutron (0.025 eV) source (right). The mean of the measured peak has been normalised to lie at 121.2 detected photons, in-line with the simulated results.

tons $\equiv 89 \pm 7$ for the measured data (with respect to the neutron peak mean). The Compton edge of the simulated data (Fig. 5.8c, red) is estimated slightly lower at 85.9. The alpha-triton products of the neutron capture reaction produce less scintillation light per unit energy deposited in comparison to the Compton electrons. This is modelled in the simulation via the Birks formula in Eq. 3.2, which is estimated as $k_B = 0.0025$ g/cm^2/MeV (see Sec. 3.1.1). The ratio of ^{60}Co edge to neutron-capture peak is used to test the Birks estimation. Ratios of: $R_{measured} = 0.73 \pm 0.06$ and $R_{Sim} = 0.71$ are obtained for the proposed Birks factor. This close agreement of Compton edge to n-capture peak indicates that the value of k_B is close to 0.0025 g/cm^2/MeV.

Data were measured and simulated for the SoNDe Test Module with and without the GS20 scintillator for moderated and unmoderated (fast) neutrons. The MAPMT borosilicate glass window has a significant ^{10}B content so that some signal from neutron capture is possible. A flowchart has been included in Fig. 5.10 to display how the data were taken. The results for the measured data and simulated data are shown in Fig. 5.11.

Moderated Neutrons without GS20 Comparison

The absence of the GS20 scintillator means neutron capture events with ^{6}Li are no longer possible. The window of the MAPMT is constructed of borosilicate glass. ^{10}B occurs naturally at an abundance of $\sim 20\%$ [135] and has a thermal neutron (0.025 eV) capture cross-section of $\sigma \sim 3850$ barns [136], therefore it is important to measure the response of the 'bare' MAPMT. The incoming moderated neutrons may get captured by the trace amounts of ^{10}B. Of the products of the capture reaction (^{7}Li*, α and γ) could in principle cause scintillation in the glass, but the scintillation efficiency is poorly known and very likely small. Other possible mechanisms to produce a signal are discussed in the following.

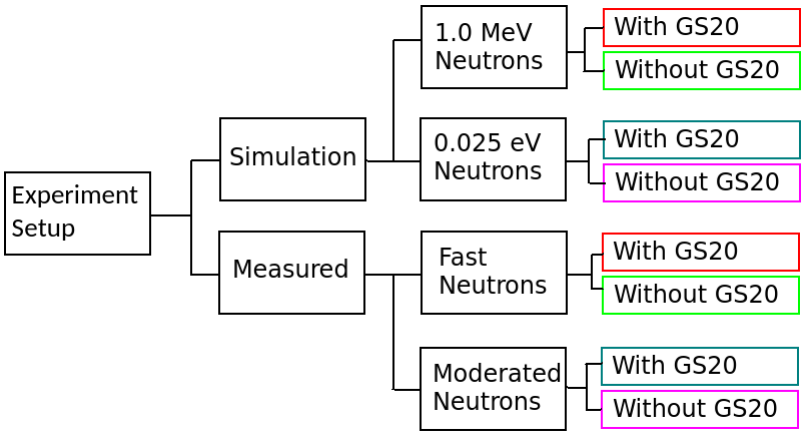

Figure 5.10: A flow chart of the measured and simulated data performed in various combinations in this work.

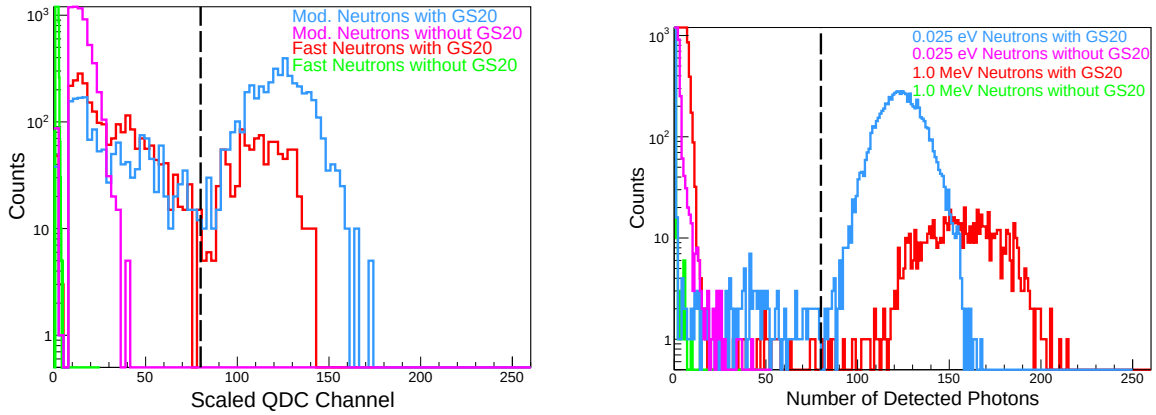

(a) (b)

Figure 5.11: Measured neutron data results (left) displayed as normalised pulse height equivalent to the simulated number of detected photons (right). The plots show data for the detector with/without the GS20 scintillator glass for moderated/unmoderated (fast) neutrons.

The 478 keV [137] gamma-rays produced in the ^{10}B capture reaction can Compton scatter in the glass, thus creating electrons. These electrons are not energetic enough to produce Čerenkov radiation, as the threshold is > 0.614 MeV ($v_{particle} > c/n$, where n = 1.51). However, 4.44 MeV gamma-rays are emitted from the AmBe source (Eq. 5.3). These gamma-rays were shielded using 20 mm of Pb, therefore only $\sim$ 55% of the initial gamma-rays were removed [138]. This means both the Compton electrons produced in the glass from the AmBe gamma-rays and the electrons produced from the gamma interactions within the Pb shielding may cause Čerenkov radiation. To confirm the contributions of these electron events further simulation studies would be required.

Compton electrons may also record a signal if they fall incident upon the first dynode within the electronics chain. The number of multiplication stages required to record the maximum signal size for the H12700 MAPMT is ten. Therefore if a Compton electron were incident upon a

dynode > 1 the signal would be very much smaller [105]. The results for the detector are shown in Fig. 5.11a in magenta. It shows a significant number of photons detected which would be successfully cut-out with a 80 photon threshold (black dashed line). The corresponding simulation results in Fig. 5.11b in magenta for thermal neutrons (0.025 eV) show a more confined spectrum with a smaller number of detected photons. The simulation did not include borosilicate scintillation and possible background from 4.4 MeV gamma-rays and will be extended to investigate these effects.

Fast Neutrons with and without GS20 Comparison

The background radiation field in the SKADI instrument may contain fast neutrons across a range of energies. The results for unmoderated fast neutrons with GS20 are shown in Fig. 5.11a in red. A small peak is distinguishable where low energy fast neutrons may still be captured by the GS20 scintillator. The peak position is lower than that of the simulated spectrum (Fig. 5.11b red). This discrepancy is not understood, but the simulation is being extended to incorporate the ISO 8529-2 evaluation of the AmBe neutron spectrum.

The detector response to fast neutrons without GS20 is similar for both the measured and simulated data, a very small number of detected photons < 10. The medium to low energy fast neutrons will deposit energy in the borosilicate glass face via inelastic scattering. The probability of a capture reaction with ^{10}B occurring is significantly decreased due to the energy of the neutrons.

5.6 Gain Map Comparisons

A moderated neutron gain map was produced for comparison with the laser (Fig. 2.18), alpha (Figs. 4.8 and 4.9) and Hamamatsu (Fig. 2.4) gain maps. A raw QDC spectrum taken with the AmBe source is displayed in Fig. 5.12. The green distribution is a Gaussian fit to the pedestal distribution while the red line is the Gaussian fit on the edge of the spectrum. The gain was defined as

$$G_i = 100 \times \frac{\mu_{sig} - \mu_{ped}}{G_{max}}, \tag{5.5}$$

where i is the ADC channel number from 100 to 163, μ_{sig} is the mean of the Gaussian distribution in QDC bins (red, Fig. 5.12), and μ_{ped} is the mean Gaussian distribution in QDC bins (black, same figure) fitted to the pedestal signal. To find the relative gains for the 64 pixels the individual pixel gains were normalised against the pixel with the highest gain and multiplied by 100. The relative pixel gains have a standard deviation $\sigma = 11\%$ and the pixel map of these gains (Fig. 5.13) shows a similar "hot" region towards the centre and lower gain pixels surrounding the edges, in-line with the previous gain map results (Secs. 2.2.5 and 4.3.3).

The H12700 MAPMT S/N LA0125 was irradiated with a number of sources to test the

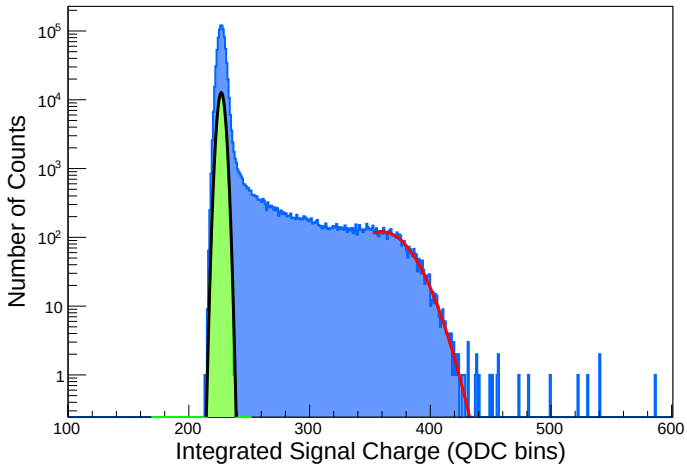

Figure 5.12: Raw QDC pedestal (green) and moderated neutron (blue) signals with fitted Gaussian distributions (black and red respectively) for ADC142 (P45). μ_{ped} = 227 QDC bins and μ_{sig} 362 QDC bins, which was the highest recorded over the 64 pixels, giving P45 a relative gain of 100 for moderated neutrons.

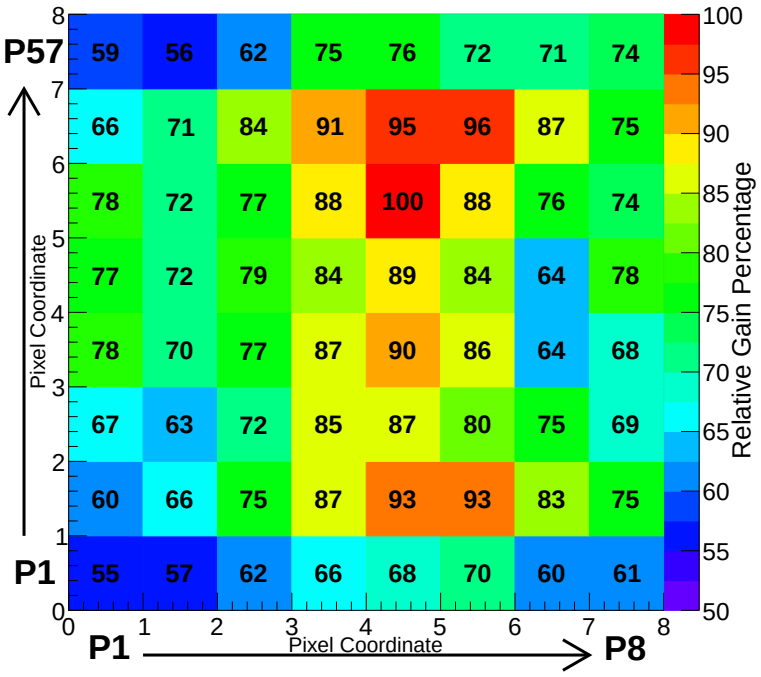

Figure 5.13: 8 × 8 gain map measured with moderated neutrons from an AmBe source. High voltage = -1000 V and the standard deviation across the pixels σ = 11%. The X and Y axes indicate the pixel location and the Z-axis represents the relative gain percentage.

relative gains of each pixel against the specification gains provided by Hamamatsu (Fig. 2.4). The comparison results are shown in Fig. 5.14.

The results for standard deviation (σ), anode ratio, conformity to 1.0 : 2.0 Hamamatsu anode

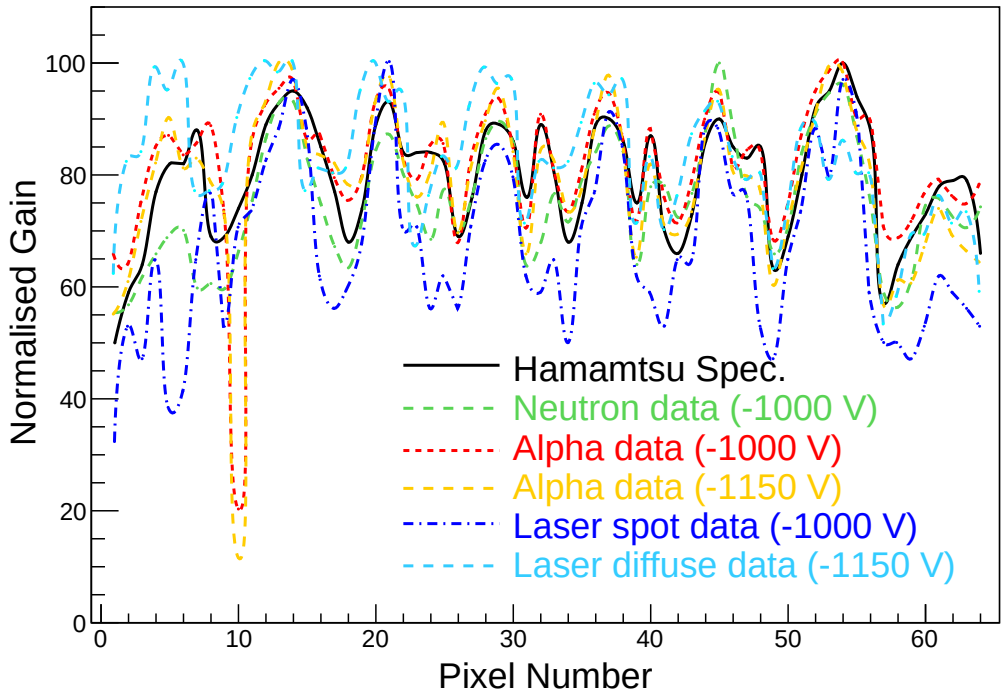

Figure 5.14: Summary of relative gain variations taken from the Hamamatsu specification (black), neutron data at -1000 V (green), alpha data at -1000 V (red), alpha data at -1150 V (gold), the laser spot data at -1000 V (blue), and the diffuse laser data at -1150 V (light blue).

ratio, and average gain ratio per pixel (R_G) are shown in Table 5.2.

To compare the gains collected from the 64 pixels of each measured data set relative to those provided by Hamamatsu, an average gain ratio per pixel (R_G) was calculated with the equation

$$R_G = \sum_{i=1}^{64} \frac{(g_{ri}/g_{hi})}{64}. \tag{5.6}$$

g_{ri} is the gain of the radiation type r for pixel i, g_{hi} is the gain of the Hamamatsu data h for the relative pixel i. The results for each radiation type are shown in column five of Table 5.2.

Table 5.2: Comparison of the gain variation properties of the MAPMT for the Hamamatsu specification data, moderated neutron, alpha source at -1000 V and -1150 V, and 404 nm spot and diffuse laser results.

Measurement	σ	Anode Ratio	1.0 : 2.0 Ratio	R_G
Hamamatsu at -1000 V	11%	1.0 : 2.0	64/64	1.00 ± 0.0
Mod. neutron at -1000 V	11%	1.0 : 1.8	64/64	0.95 ± 0.01
Alpha at -1000 V	9%	1.0 : 1.6	63/63	1.05 ± 0.02
Alpha at -1150 V	11%	1.0 : 1.8	63/63	1.00 ± 0.02
Laser spot at -1000 V (1 PE)	16%	1.0 : 3.1	58/64	0.84 ± 0.02
Laser diffuse at -1150 V (120 PE)	12%	1.0 : 1.9	64/64	1.05 ± 0.02

The alpha (-1000 V) data has the lowest standard deviation value of all measured data sets. Both alpha, neutron, and diffuse laser data sets follow a similar trend to the data provided by Hamamatsu, apart from a few outliers. The 404 nm laser spot data has the largest standard deviation and generally underestimates the pixel gain. The low gain nature of this MAPMT may have made the single PE gain measurements difficult with a larger margin of error.

The laser spot data has the largest deviation from the Hamamatsu specification, with R_G = 0.84 ± 0.02. The other four data sets have relatively similar average gain ratios per pixel, with the alpha data at -1150 V closest to 1. The MAPMT S/N LA0125 used in these measurements was deemed 'low gain' with an absolute gain = 0.84×10^6 as measured by Hamamatsu (compared to a gain = 3.37×10^6 for S/N LA0074 in Fig. A.1), therefore an increased HV may improve the overall pixel output. The outlying results of pixel 10 recorded by both alpha data sets may have been the result of a bad connection to the QDC module. This pixel had not been recorded as faulty during previous or subsequent measurements. Disregarding this anomalous result, the alpha source or the moderated AmBe neutron source provide an instrument realistic and practical method for characterising the 64 pixel relative gains of the SoNDe modules as they age over their lifetime. For rapid testing of individual MAPMT's the higher light level full detector illuminations using the diffuse laser are ideal.

5.7 Summary

The SoNDe Test Modules's response to ^{60}Co gamma radiation shows no photopeaks due to the low-Z composition of the GS20 scintillator and the edge of the Compton scattering continuum is difficult to determine as only very few $\sim$ 1 MeV electrons stop in the scintillator depositing their full energy. The 'Compton edge' was estimated aided by comparison to the simulated spectrum and used to calibrate the energy response of the detector in MeVee (mega electron volts electron equivalent) to a moderated AmBe neutron source. The calibration found a moderated neutron peak at $\sim 1.42 \pm 0.14$ MeVee, very much lower than the 4.78 MeV of the final-state triton and alpha, so that GS20 shows significant quenching of the ion signal compared to electrons.

The Geant4 based simulation handles thermal and fast neutrons, as well as gamma radiation. The response of the detector to a range of mono-energetic neutron energies was calculated. Thermal neutrons (0.025 eV) as well as neutrons of energies 0.1 MeV - 1.0 MeV were seen to undergo capture interactions with the ^{6}Li, however as the energy increased the probability of a capture occurring decreased. The neutrons with energies > 10 MeV can initiate (n,p) and other reactions, where the final-state charged particle(s) create a deposited-energy continuum.

Data were taken with an AmBe source both with and without the addition of the GS20 scintillation glass. The presence of ^{10}B in the glass window of the MAPMT meant that capture interactions may intermittently take place when the GS20 is removed although its unclear if the borosilicate scintillates significantly. However electrons produced by the 4.44 MeV gamma-ray

from AmBe have sufficient energy to generate Čerenkov radiation in the borosilicate glass and this will contribute to the signal. The results of the measured and simulated data were largely in agreement for the SoNDe Test Module and are consistent with a Birks parameter of $k_B = 0.0025$ g/cm^2/MeV for thermal neutron-capture and $\sim$ 1.0 MeV gamma rays.

The individual-pixel gains recorded with moderated neutrons produced a map similar to that of the Hamamatsu specification. The results of the gain mapping were consolidated for all types of radiation used in the measurements. The results are broadly in agreement with the specifications provided by Hamamatsu, although there are differences in detail. They show that alpha or neutron sources provide a practical gain calibration method for SoNDe modules.

Chapter 6

Monoenergetic Proton Beam Study

6.1 Motivation and Setup

A final in-depth investigation into the Geant4 simulation validation was performed with a tightly focused, monoenergetic 2.5 MeV proton beam (used to approximate the 2.73 MeV triton response from the ^{6}Li capture reaction) with diameter $\sim 100\ \mu$m. The beam was scanned across a small area of the detector face in the horizontal and vertical directions. The coordinates were set relative to the origin at the centre of the MAPMT (centre between pixels 28, 29, 36 and 37). The horizontal scan covered the coordinates -3.1 - 6.9 at a constant y = 1.9 mm, in 0.5 mm steps and the vertical scan covered the coordinates -8.1 - 1.9 at a constant x = 2.4 mm, in 0.5 mm steps.

The GS20 scintillator finish in the Geant4 simulation had previously been assumed to be 'perfect', i.e. completely smooth. The polish (P) finish was investigated for varying degrees of smoothness and compared with the measured results.

The H12700A detector used in this investigation belonged to the Nuclear Physics division at Lund University. Its model number is ZA0250, and a corresponding gain map of the detector is shown in Fig. 6.1. The pixel gains of this detector are relatively more uniform than the MAPMT used in the previous investigations. The sheet of GS20 scintillation glass used was nominally identical to that used in Glasgow, with the same dimensions ($52 \times 52 \times 1$ mm^3). It is important to bear in mind that the concentration of ^{6}Li may vary slightly from scintillator to scintillator and it's distribution throughout the glass may not be completely uniform. The variation of ^{6}Li distribution in GS20 scintillation glass is currently being studied at the Lund Ion Beam Analysis Facility (LIBAF) [141].

6.2 Proton Accelerator

The LIBAF at Lund University houses a 3 MeV single-stage Pelletron accelerator. A Pelletron is an electrostatic accelerator that works under the same principle as a Van de Graaff generator, utilising a chain of 'pellets' as opposed to a rubber belt. The pellets are linked with an insulating

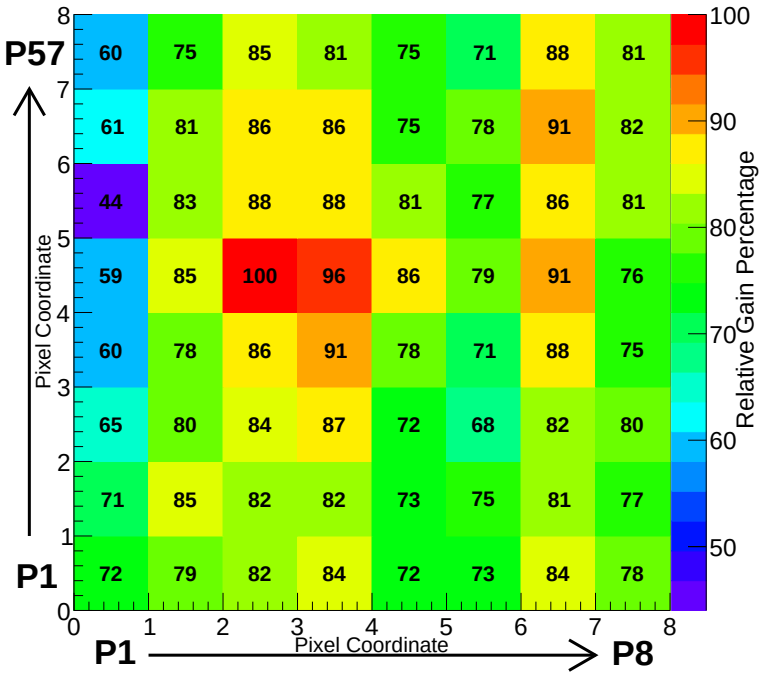

Figure 6.1: The Hamamatsu specification relative gain map of the Lund H12700A MAPMT used for the proton beam studies. The Z-axis represents the normalised gain.

material e.g. nylon, and are charged by induction. The positive charge is delivered to the high voltage terminal in a process known as 'up-charging'. The chain passes through a negatively-biased suppressor electrode and smoothly deposits charge onto the terminal pulley. The chain exits and begins 'down-charging', the reverse procedure of up-charging, which increases the charging current capacity of the chain [139] and the cycle continues. The magnitude of voltage held on the HV terminal determines the particle energy. The LIBAF ion source is capable of producing continuous beams of protons, deuterons or alpha.

The accelerator was used to generate a 2.5 MeV proton beam (current $\sim$ nA range), with an estimated energy loss of 20 keV, originating in the beam line window and air gap between the emergent beam and detector. The proton beam was guided down the high-vacuum beam line using steering magnets, adjusted in intensity with aperture slits, and finely focused using quadrupole magnets [142]. The beam emerged from the evacuated beam line, through a 200 nm thick Si_3N_4 window [143], onto the SoNDe Test Module housed within a room temperature and pressure, light-tight detector chamber. The SoNDe detector was mounted on a motorised X-Y-Z translation stage and placed 0.5 mm from the emergent beam window. The beam diameter was estimated to be $\sim$ 100 μm using a fluorescent glass plate.

A schematic diagram of the proton accelerator is shown in Fig. 6.2. The circuit layout for this experiment was similar to that of the neutron measurements taken at the Source Testing Facility and is shown in Fig. 5.3 with circuit adjustments for the proton beam shown in red.

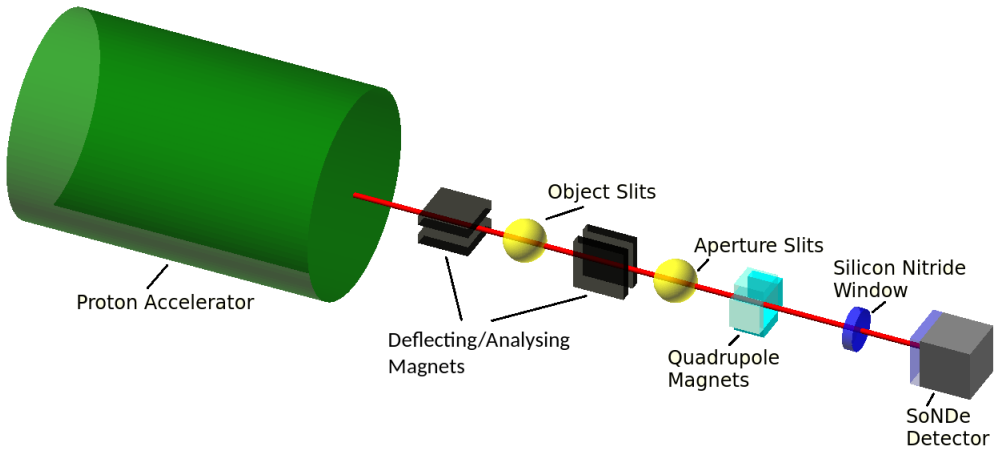

Figure 6.2: A 3D schematic of the proton accelerator located in the Lund Ion Beam Analysis Facility, with beam direction traveling left to right. The accelerator (green) produced a 2.5 MeV proton beam which was steered through the evacuated beam line with deflecting/analysing magnets (black), object and aperture slits (yellow), and quadrupole lenses (cyan). The beam exited into the non-evacuated chamber through a 200 nm Si_3N_4 window (blue) and was incident upon the SoNDe Test Module (grey). Image derived from [141]

6.3 Results

The intention of the Cerberus splitter boards [133] shown in Fig. 5.3 was to provide identical data signals to both the VME based DAQ and portable IDEAS DAQ for a direct comparison. Unfortunately the Cerberus-to-IDEAS link was not operational during the allotted beam time and therefore all results for this section were collected using the VME based DAQ only. For similar results taken with the portable IDEAS DAQ directly attached to the MAPMT see Ref. [109]. The results for the measured proton data (black lines and triangles) for horizontally adjacent pixels 28 and 29 are shown in Fig. 6.3 with the corresponding simulated data. As mentioned, the simulations, used previously, assumed a perfect finish to the scintillator polish (P = 1.0) and these results are shown with red lines and triangles. The polish factor 'P' was then set to P = 0.8 (blue lines and triangles) and P = 0.5 (magenta lines and triangles) for non-perfect scintillator glass sheets. The aforementioned simulation data sets did not take into account electronic noise or crosstalk. A simple model of crosstalk, described below, was used to simulate such electronic smearing and the effect on the simulated data for P = 0.8 is shown as blue dashed lines and triangles.

The amplitudes of the pulse-height spectrum at each position in plots (a) and (c) have been normalised so the highest mean amplitude is equivalent to 1 for each data set. The ratio of the standard deviation to the signal mean for each position is plotted as the relative peak width in (b) and (d).

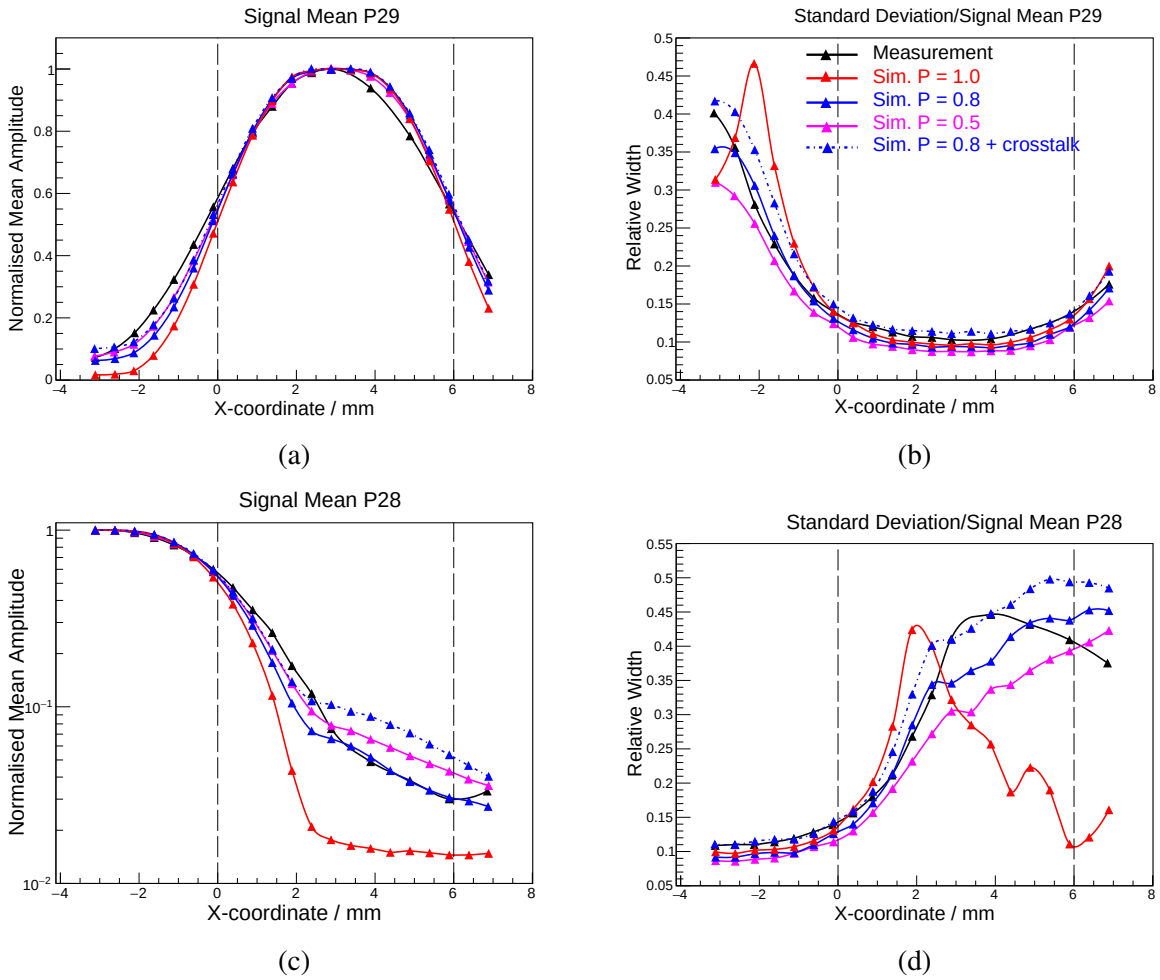

Figure 6.3: Horizontal proton scan with results shown for P29 (plots (a) + (b)) and P28 (plots (c) + (d)). Colour coding is shown in plot (b) and is relevant to all sub-plots. The vertical dashed lines represent the pixel boundaries 28-29 (left) and 29-30 (right).

The simulation previously explored the effects of optical crosstalk within the scintillator and borosilicate glass on the detector. Electronic crosstalk is the effect when signal from one pixel leaks into a neighbouring pixel (horizontally or vertically adjacent). It varies broadly from pixel to pixel and may originate from stray photoelectrons in the dynode chains or pickup effects between the output anodes. The contribution of electronic crosstalk was approximated by sampling from a Gaussian distribution centred at 3% of the signal amplitude (given as number of scintillation photons) with a width (σ) of 3% of the signal amplitude. The previously measured crosstalk values for the H12700A S/N LA0125 (Fig. 2.28) were between $\sim$ 0.14% and 3%, while values obtained for the study in Ref. [105] quoted up to $\sim$ 7% crosstalk. The crosstalk simulation randomly generated a leakage signal (red, Fig. 6.4) from the Gaussian, subtracted this from the target pixel and added it to a neighbour pixel. This was performed for each nearest-neighbour pixel.

Smearing of the signal due to electronic noise was achieved by sampling from a Gaussian distribution fitted to the pedestal signal for the raw QDC data. The widths of the distributions

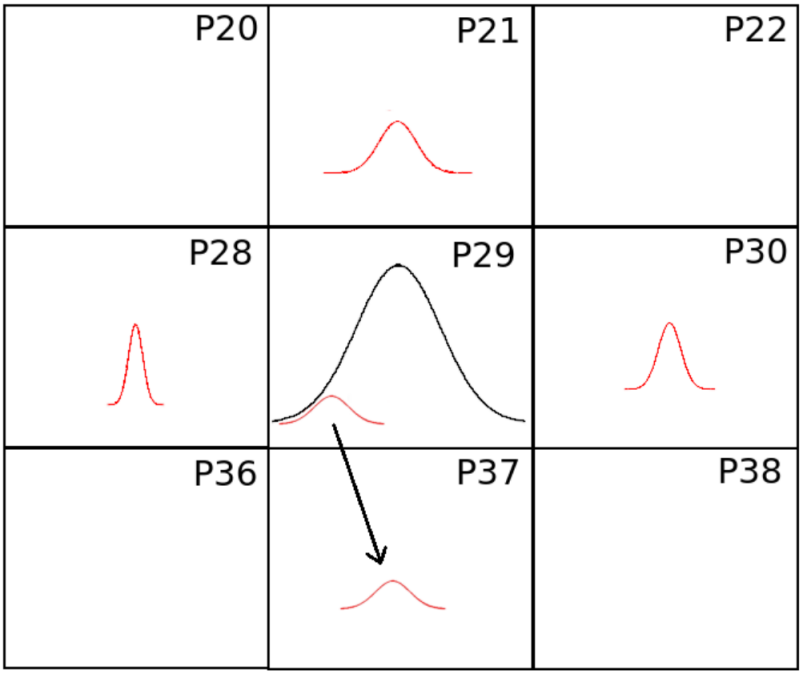

Figure 6.4: A representation of the process used to add electronic crosstalk into the adjacent neighbouring pixels (21, 28, 30, and 37) with separate Gaussian distributions (red) centred on 3% with a width of 3% used to emulate the contributions due to electronic crosstalk.

were equivalent to approximately 2 detected photons. At this level, the effect of noise is small in comparison to the contributions due to crosstalk.

The main results indicate that a 'perfect' polish finish of P = 1.0 for GS20 is not representative of the measured data. It generally under-predicts the amount of scintillation light spreading from the target pixel to its neighbours. The simulated position dependence of the P29 mean signal amplitude (Fig. 6.3a) is too flat close to the centre of the pixel and too steep close to pixel boundaries. The addition of an imperfect scintillator surface increases the spread of scintillation photons. The measured data weaves between both these data sets but tends to lie slightly closer to the P = 0.8 distribution. The addition of 3% crosstalk to the P = 0.8 data again increases the spread of signal amplitude and displays a similar trend to P = 0.5. Therefore, it is difficult to quantify the individual effects of these new features through comparison with the current data.

The proton beam data provided higher resolution results than the previous alpha data shown in Sec. 4.4.2. Both H12700A detector's used in these studies showed similar responses at their pixel centres and boundaries, meaning the effects recorded when scanning radiation across the pixel boundaries can be considered universal to the H12700 detectors. As discussed previously in Sec. 2.2.3 (Fig. 2.13), the non-uniformity of the photocathodes will vary from detector to detector and may cause anomalies in the measured results. The inclusion of a non-uniform cathode based on the unique mapping response of an H12700A MAPMT may provide an insight as to where the largest source of distortion lies as this cannot be concluded with the simulated data at present.

Chapter 7

Conclusions and Outlook

The European Spallation Source intends to begin its user program in 2023 after nine years of construction. It will provide an in-depth view into material structure and function from the microscopic to atomic scale, enabling the development of new materials for industrial and societal needs. As of November 3rd 2020 the ESS has joined a consortium dedicated to the rapid response of the Covid-19 pandemic. They will work in conjunction with other facilities to probe the Sars-Cov-2 virus for "weak spots" and help develop novel drugs for the treatment of Covid-19 patients.

This thesis is concerned with the development and characterisation of a position sensitive thermal neutron detector, which does not require ^{3}He, for implementation in a small angle neutron scattering instrument (SKADI). A number of detector types were considered for the instrument. The detector was required to be devoid of ^{3}He and modular, possessing timing resolution better than the μs level, a thermal neutron detection efficiency > 80%, low gamma-ray efficiency, a position resolution better than 6 mm, and a counting rate capability of $\sim$ 20 MHz over a 1 m^2 detector area. The investigation looked at several aspects of the detector requirements and performed in depth characterisation studies into the response of a proposed detector called the SoNDe module to several forms of radiation.

Requirements Fulfillment

The SoNDe module is comprised of a thin sheet of thermal neutron sensitive GS20 ^{6}Li scintillation glass, a 64 pixellated MAPMT, and a portable data acquisition system. The entire module measures approximately $52 \times 52 \times 85$ mm^3. The module forms part of an array of 400 detectors due for installation in the SKADI instrument.

The SoNDe Test Module (GS20 + MAPMT + VME DAQ) demonstrated a clearly defined moderated neutron peak (Sec. 5.3) and detection efficiency of 75% (Sec. 5.4) [2] [110], close to the required 80% (which may be improved with further studies). The global (1×1 m^2) count rate capability of the GS20 sheet coupled to a H12700 MAPMT is estimated as 37 MHz [86], surpassing the 20 MHz per 1×1 m^2 set out in the initial requirements. The MAPMT has a

time resolution on the order of sub-ns and the scintillation-pulse rise time is of the order 10 ns. However the overall time resolution is largely determined by the portable IDEAS DAQ which shapes the pulses with a time constant of 1.4 μs and has a clock resolution of $\sim$ 10 ns. Thus the SoNDe module ensures a very much better time resolution than the μs scale. The desired 6 mm position resolution is compatible with the 6×6 mm^2 dimensions of the H12700 MAPMT pixels. Better resolution, at the few mm level, can be achieved when the scintillation light is spread over several pixels [131] and could be further improved using an 'Anger Camera' mode where one takes an amplitude-weighted mean pixel position. The IDEAS DAQ is not yet capable of performing such analysis. The Anger camera approach is currently being investigated using fine-scan proton data. Potential future work may include developing this Anger mode for the portable DAQ and a Geant4 simulation investigation.

System Stability Testing and Initial Characterisations

The stability of the SoNDe Test Module setup was measured using two procedures. Firstly, with a 1 mm diameter 404 nm laser spot (without the presence of GS20) for a 34 hour period, and secondly using a 1 mm diameter collimated alpha source for a 67 hour period. The 404 nm laser was used to mimic the mean scintillation photon wavelength λ = 395 nm. An ^{241}Am alpha source with a mean energy of 4.54 MeV (in vacuum) was used to emulate the 4.78 MeV of ionising radiation produced from the capture by-products ($\alpha + {}^3$H). A drift of 1.15×10^{-4} %/hr was determined for the laser data (Fig. 2.11), and 2.93×10^{-4} %/hr for the alpha data (Fig. 4.6). The results indicated that, although the drift was not consistently positive/negative for the radiation types used, the effect was so small for both that the whole setup could be deemed sufficiently stable for use over a prolonged period. The results also indicated the MAPMT would require sufficient 'warm-up' time of at least 30 - 60 minutes prior to operation.

Characterisations to determine the uniformity and relative gain differences of the photocathode were performed using millimetre stepped scans. These measured the detector response to a 1 mm diameter laser beam at single and 60 photoelectron intensity levels, and a 1 mm diameter collimated ^{241}Am alpha source. These scans (Sections 2.2.3 and 4.5, respectively) uncovered dead spaces between pixels, relative pixel gains, and areas of increased crosstalk. Pixel boundaries appeared most pronounced at single PE levels (Fig. 2.13). Areas of the detector which contain support structures became apparent at higher light levels (60 PE, Fig. 2.14). Differences in the apparent pixel shapes were observed between the laser and alpha data sets. The pixels from the laser data appeared semi-rectangular, whereas the alpha data resembled oblate circles. This effect was likely due to the spreading of scintillation photons from the alpha excitation in the GS20.

Relative pixel crosstalk measurements for the eight adjacent pixels surrounding the target pixel were taken. The laser setup included a detector mask with a 1.5×1.5 mm^2 square hole, positioned at the centre of the pixel. The alpha setup used the 1 mm diameter collimator and

was devoid of a mask. Crosstalk, the ratio of the neighbour signal amplitude to the target signal amplitude (in %) was measured to be in the range 0.0 - 3.0 % for the laser data, and 2.5 - 9.8 % for the alpha data. Compared to the crosstalk range of 0.0 - 2.1 % measured by Hamamatsu with an optical fibre flush against the MAPMT, the laser data is in reasonable agreement. The spread of light within the scintillator from the ionisation and excitation events caused by the alpha particles gave rise to the increased magnitude of crosstalk.

Calibration of MAPMT Pixel Gains

Relative gain maps were produced for the SoNDe Test Module using a laser spot centred on each pixel (at -1000 V), a diffuse square laser beam illuminating all pixels simultaneously (at -1150 V), a collimated alpha source centred on each pixel (at -1000V and -1150 V), and a moderated neutron source simultaneously illuminating all pixels (at -1000 V). The results for each method were assessed from the following criteria: the standard deviation of the pixel relative gain values, the ratio of minimum to maximum gain values (and their conformity to the 1.0 : 2.0 worst-case value specified by Hamamatsu), and the average pixel gain ratio with respect to the Hamamatsu measurement (Eq. 5.6). The full results are shown in Table 5.2 and the variation, as a function of pixel number, of normalised relative gains for each method is shown in Fig. 5.14. Alpha, neutron, and diffuse laser results were similar to the Hamamatsu measurement, with all pixels conforming to the 1.0 : 2.0 anode ratio and showing a low standard deviation, σ = 9 - 12 %. The average gain ratio per pixel for these results ranged between R_G = 0.95 - 1.05. The laser spot results were furthest from the Hamamatsu specification. It was concluded for periodic relative gain recalibration of the MAPMTs used in the SKADI detector, a moderated neutron source, collimated alpha source or diffuse laser illumination (at operational HV) would be suitable to map the relative gains of the pixels in the detectors.

The Geant4 Based Simulation

A Geant4 based computer model of the SoNDe module was used to find the optimum configuration of the detector for localised transport of optical photons and then to predict the detector's response to laser beams and various types of ionising radiation. These predictions were tested against equivalent measurements. Optical-photon tracking through the GS20 sheet and MAPMT window of the SoNDe detector tested a number of different configurations including: groove depth and width on a pixellated sheet of scintillator, optical coupling between the GS20 and the MAPMT window, and scintillator reflective coating. The results showed that the simple-to-implement configuration of a non-pixellated scintillator devoid of optical coupling or scintillator reflective coating produced the least spread of photons from their point of origin, as demonstrated in Sec. 3.1.2 by a maximum true-to-false hit ratio R_{TF} of $\sim$ 18 and a minimum mean photon displacement (δr $\sim$ 1.5 mm) from point of origin. However this configuration also resulted in the lowest photon detection efficiency ($\varepsilon_T \sim 2.5\%$). Better efficiency was achieved by

adding optical coupling medium between the glass components and an outer reflective coating to the GS20. However this came at the expense of poorer R_{TF} and δr, which were considered more important parameters since the scintillation intensity of GS20 is quite high.

This optical configuration was then used in the full simulation of the SoNDe response to ionising radiation, where scintillation photons were produced along the charged-particle tracks.

Measured and Simulated Results For Laser Beam

Cross-pixel mm stepped scans in the horizontal, vertical, and diagonal directions were conducted with the SoNDe Test Module. The setup included a mask for the detector with 0.5 mm diameter holes, spaced 1 mm apart. The presence of vertical dynode slits and structural obstructions at the four pixel boundary affected the passage of electrons from the photocathode to the first dynode and thus varied the output amplitude of the detector. The current version of the simulation did not take the presence of these structural apertures/boundaries into account, but the differences between simulated and measured results does offer a means to gauge their importance.

Measured and Simulated Results For Alpha Radiation

The detector's response to laser light was measured thoroughly, but more importantly its response to ionising radiation needed to be fully established. The ranges of the neutron-capture by-products, alpha and triton, are 7 μm and 36 μm respectively. Therefore, one would expect the detection of a captured neutron event to remain localised within the pixel area where the capture took place. However, the spread of scintillation photons cannot be eliminated and the issue of light sharing across pixel boundaries was examined. The collimated alpha source was scanned in the horizontal, vertical, and diagonal directions across a set of 4 pixels, similarly to the laser test. Events which occurred at the boundary between two pixels saw an approximately even split in the number of detected photons (Figs. 4.15 and 4.16). Likewise, at the four pixel intersection, each pixel saw approximately one quarter of the total number of photons (Fig. 4.17). The results of the signal amplitude variation with interaction position for the simulated setup were in close agreement to the measured data as shown in Table 4.2. Discrepancies were apparent between the measured and simulated widths of the pulse-height distributions, suggesting the need for electronic noise contributions from the back-end electronics of the detector to be factored into the simulation.

The alpha source was used to establish the high voltage vs gain (from signal amplitude) variation. The trend (Fig. 4.7) showed a non-linear increase in gain with increasing high voltage up to the recommended absolute maximum of -1150 V, in accordance with the relationship given by Hamamatsu (Eq. 4.10). Above -1150 V the gain curve will flatten, saturate and eventually the MAPMT signal will die. As these MAPMTs are not being used for low light level studies (e.g. single photon level), and the light collected from GS20 per captured neutron is > 100 photons, running them at lower voltages e.g. 900 - 1000 V will provide a decent signal far above

threshold/noise and will decrease the mean anode current, thus increasing the longevity of the detector.

Measured and Simulated Results For Proton Beam Irradiations

The alpha scan measurements showed good agreement with the simulation. However more detailed scanning using a 0.1 mm diameter, 2.5 MeV proton beam offered a more stringent test of the simulation's prediction. This highlighted small but significant discrepancies in the simulated position dependence of the proton pulse height distributions. A polish factor 'P' was introduced to model the effect of surface finish of the GS20 scintillator. The 'perfect' polish finish P = 1.0 under-predicted the degree of light signal spread between pixels, which increases as P departs further (P = 0.8, 0.5) from a perfectly smooth polished surface. Electronic crosstalk and noise contributions were estimated and used to smear the simulation data to see if their effects bore a similarity to the measured data. The crosstalk and noise contributions added to P = 0.8 showed a similarity to P = 0.5 with no additional contributions, so that the full effects of these new features were hard to disentangle. Future work on the simulation will include the non-uniform photocathode response map of the MAPMT. The nuances of the photocathode distribution could reveal a further source of distortion in addition to crosstalk and noise effects.

Measured and Simulated Results For Gamma and Neutron Radiation

The most important test for the SoNDe Test Module was its ability to detect thermal neutrons and produce a neutron capture signal which can be separated cleanly from background processes. The Lund Source Testing Facility is home to a number of neutron sources including; AmBe, PuBe, and ^{252}Cf. In order to obtain 'near thermal' neutrons, polyethylene blocks of thickness 50 mm were used to moderate the neutrons from AmBe. Fast neutrons and gamma radiation will still be present in the incoming radiation flux (and most likely in the background of the SKADI instrument), so it is important to measure the detector's response to a range of neutron and gamma energies. The energy response of the detector was calibrated using the end-point of the Compton distribution of a ^{60}Co source. The energy of the capture peak from moderated neutrons was found to measure 1.42 ± 0.14 MeVee (Mega Electron Volts Electron Equivalent), which is consistent with the gamma equivalent energy for thermal neutrons quoted by the manufacturer Scintacor. A comparison of pulse height spectra from an uncollimated, moderated AmBe source and a collimated beam of 2.4 Å neutrons from a reactor showed very similar peaks (Fig. 5.2). The 64 pixel response of the detector (Fig. 5.7) showed edge effects, after selection of events where only a single pixel is above threshold. This is caused by light loss at the edges of the GS20 scintillator and a lack of outer neighbouring pixels which render the single-pixel condition less effective (Sec. 5.3). The central pixels showed more pronounced neutron-capture peaks.

The response of the SoNDe Test Module to gamma radiation ranging from 0.66 MeV - 100 MeV and neutron radiation ranging from 0.025 eV - 100 Mev was simulated. Diffuse Compton

edges were apparent for low energy gamma radiation (< 1 MeV). Higher energy gamma rays (2.6 MeV - 100 MeV) showed a continuum of energy as the secondary electrons generated through Compton scattering and pair production deposited only small amounts of energy in the low-Z scintillation glass due to the increased electron range in the material. The neutron distributions showed a strong capture peak at 0.025 eV and residual capture peaks made by lower energy fast neutrons (0.1 - 1.0 MeV). The higher energy fast neutrons (10 - 100 MeV) created an energy continuum through the fragmentation of nuclei within the scintillator, resulting from (n,p), (n,α), and (n,2n) interactions.

The measured data were normalised to the equivalent number of detected photons and directly compared to the simulation. This was carried out for a number of different configurations (Fig. 5.10) of moderated(thermal)/fast neutrons for a detector with/without GS20 scintillation glass. The results show some similarities but also some differences arising from the assumption of mono-energetic neutrons and a lack of background radiation in the simulation. The simulated results are consistent with a Birks factor k_B = 0.0025 g/cm^2/MeV (Sec. 3.1.1). Future work on the simulation will include incorporation of the ISO 8529-2 neutron spectrum characteristic of AmBe sources, incorporation of estimated spectra of particle background expected at SKADI, more detailed investigation of MAPMT edge effects and more detailed investigation of light signals originating from neutron and gamma-ray interactions in the MAPMT glass. Background estimations could be guided by measurements at similar facilities, such as SNS at Oakridge.

Evaluation

The SoNDe module conforms to an acceptable level of the detector requirements set out prior to its inception. The SoNDe Test Module was thoroughly characterised using various forms of ionising and non-ionising radiation. The stability of the system over a prolonged period makes it suitable for measurements over extended time periods but does not remove the importance of periodic gain recalibration, methods for which have been clearly outlined in the thesis. Computer simulation of the SoNDe module, validated by comparison to an extended set of measurements, shows that the chosen detector configuration results in the tightest confinement of the scintillation signal to its point of origin. The clean response of the detector to moderated neutrons in the presence of fast neutrons/gamma background is a good indication that the SoNDe module will perform well within the SKADI detector housing, granted appropriate detector thresholds are set.

Outlook

Further work to improve the next generation of SoNDe modules may result in a world leading position sensitive thermal neutron detector system. Research could include increasing the level of understanding on the internal structures of the MAPMT. This could be explored using

μm laser scans to characterise non-uniformities of the position dependence of the effective photocathode efficiency, which largely depends on the ability of photoelectrons to pass from the cathode to dynode 1 in-spite of the aforementioned structures. Different sources of crosstalk such as optical photon spreading, electron leakage, and capacitive coupling of signal lines are often times difficult to disentangle. Developing a method to quantify the electronic crosstalk for each pixel of each detector would help to reduce this ambiguity. SiPM arrays, which don't have dynode structure issues, might offer an alternative to MAPMTs. However they would require a re-design of the front-end electronics to maintain good signal-to-noise-ratio.

The edge effects observed in Fig. 5.7 are the combined result of light loss along the edges of the GS20 scintillation glass and the multiplicity analysis cuts used to achieve the neutron peaks. Investigations into the use of larger scintillation sheets spanning the area of multiple detector faces (2×2, 4×4 etc.) may reduce light loss, and employing multiplicity analysis with pixels from adjacent detectors could improve the output spectra of the edge pixels for each MAPMT.

An extension of the Geant4 simulation which would include an array of detectors, and realistic models of neutron source spectra and particle backgrounds expected at ESS could broaden the understanding of the SKADI detector needs. It may indicate which detectors see a larger share of radiation and therefore suffer from more background pollution in the thermal-neutron spectrum. Such a simulation has been developed by Kanaki *et al.* [86] but does not include the predicted instrument background. The ratio of neutron capture signal to background will depend on the GS20 thickness. A comparison of neutron source measurements to simulations for different GS20 thicknesses, say 0.5 - 3 mm, would be valuable to determine an optimum value for ESS.

Appendix A

Simulated results for the 400 (20 $\times$ 20) SoNDe modules occupying a 1 m^2 area. Results are recorded for three separate configurations outlined in Table A.1. Both tables are relevant to Sec. 1.5.

Table A.1: Geant4 simulated configurations of SKADI detector with SoNDe modules laid out in 20 x 20 formation (1 x 1 m^2). The flux on the sample is time-averaged over the 2.86 ms pulse length. Table taken from [86].

config	collimation length (m)	λ_{min} (Å)	λ_{max} (Å)	source aperture (cm x cm)	sample aperture (cm x cm)	flux on sample (n/cm^2/s)	divergence (cm)
1	3	3.0	11.5	3 x 3	1 x 1	1.00 x 10^9	8.4
2	5	3.0	11.5	2 x 2	1 x 1	2.02 x 10^8	4.4
3	8	3.0	10.0	2 x 2	1 x 1	8.24 x 10^7	3.0

Table A.2: Results from simulated configurations showing estimated incident rates averaged over the 2.86 ms pulse length. Table taken from [86].

config	global average incident rate	local average incident rate/module	local average incident rate/pixel
1	37 MHz	1.1 MHz	21.8 kHz
2	5.1 MHz	167 kHz	3.6 kHz
3	2.9 MHz	99 kHz	2.3 kHz

Rate definitions are as follows:

- Global average incident rate: the number of neutrons per second entering the detector.

- Local average incident rate/module: the number of neutrons per second entering a SoNDe module.

- Local average incident rate/pixel: the number of neutrons per second entering a pixel [86].

The table used to convert the MAPMT ADC channel to the corresponding pixel number. Table relevant to Sec. 2.2.3.

Table A.3: The output ADC channel numbers to relative pixel number conversion table.

ADC	Pixel	ADC	Pixel	ADC	Pixel
100	1	**122**	27	**144**	53
101	2	**123**	28	**145**	54
102	9	**124**	35	**146**	61
103	10	**125**	36	**147**	62
104	17	**126**	43	**148**	7
105	18	**127**	44	**149**	8
106	25	**128**	51	**150**	15
107	26	**129**	52	**151**	16
108	33	**130**	59	**152**	23
109	34	**131**	60	**153**	24
110	41	**132**	5	**154**	31
111	42	**133**	6	**155**	32
112	49	**134**	13	**156**	39
113	50	**135**	14	**157**	40
114	57	**136**	21	**158**	47
115	58	**137**	22	**159**	48
116	3	**138**	29	**160**	55
117	4	**139**	30	**161**	56
118	11	**140**	37	**162**	63
119	12	**141**	38	**163**	64
120	19	**142**	45		
121	20	**143**	46		

Page 1 of 2 of the final test sheet (specification) provided by Hamamatsu for the H12700 MAPMT S/N LA0125 is shown below in Fig. A.1. The specification provides information on the cathode luminous sensitivity, anode luminous sensitivity, anode dark current, cathode blue light sensitivity index, and the absolute gain given on the order of 10^6. The absolute gain of the detector used in the majority of these studies was particularly low (0.84×10^6). This figure is relevant to Sections 2.2.3, 2.2.5, and 5.6.

HAMAMATSU

FINAL TEST SHEET

JNO. 673541
PAGE 1 OF 2

PHOTOMULTIPLIER TUBE ASSEMBLY TYPE: H12700A

HPU/LYNKEOS TECHNOLOGY QUANTITY: 32 pcs.

Serial Number	(1) Cathode Luminous Sens. μA/lm	(2) Anode Luminous Sens. A/lm	(3) Anode Dark Current nA	(4) Cathode Blue Sens. Index	(5) Gain x10^6		
LA0025	90.1	203.0	0.11	10.70	2.25		
LA0026	76.0	112.0	0.24	10.10	1.47		
LA0034	112.0	326.0	4.48	12.30	2.91		
LA0074	92.0	310.0	1.35	12.30	3.37		
LA0077	102.0	220.0	0.58	12.40	2.16		
LA0087	97.9	182.0	0.22	12.00	1.86		
LA0096	93.7	74.9	1.85	12.20	0.79		
LA0101	74.2	164.0	5.27	11.10	2.21		
LA0106	73.4	81.5	0.46	11.10	1.11		
LA0109	75.0	147.0	15.10	11.20	1.96		
LA0110	90.8	249.0	4.41	11.10	2.74		
LA0112	83.3	254.0	5.32	10.80	3.05		
LA0113	73.6	171.0	0.47	10.70	2.32		
LA0114	89.8	320.0	3.15	10.90	3.56		
LA0115	78.1	160.0	0.38	11.10	2.05		
LA0121	93.6	134.0	0.36	11.90	1.43		
LA0122	87.4	195.0	0.54	11.60	2.23		
LA0123	94.5	150.0	7.58	12.10	1.59		
LA0125	86.5	72.7	1.78	11.80	0.84		
LA0128	101.0	193.0	13.24	12.20	1.91		
LA0129	98.0	170.0	0.71	12.20	1.73		
LA0130	68.7	56.0	0.69	10.80	0.81		
LA0137	84.0	130.0	0.52	11.20	1.55		
LA0138	92.8	79.8	0.35	11.90	0.85		
LA0140	89.1	121.0	8.30	11.50	1.36		

NOTES

(1) (2) (4) Light source: Tungsten filament lamp operated at 2856 K.
(2) (3) (5) Overall supply voltage: −1000 V
Voltage distribution:

K	Dy1	Dy2	Dy3	...	Dy9	Dy10	GR	P
2	1	1	1		1	1	1	0.5

Measured as one anode output by bundling multi anode.
(4) Measured with a Corning CS 5-58 blue filter (half stock thickness).
(1) (2) (4) (5) Aperture size: □ 49 mm

Date: June 12, 2017

HAMAMATSU
HAMAMATSU PHOTONICS K.K., Electron Tube Division
314-5, Shimokanzo, Iwata City, Shizuoka Pref., 438-0193, Japan, Telephone : (81)0539-62-5248, Fax : (81)0539-62-2205

Figure A.1: Hamamatsu specification with absolute gain values.

Bibliography

[1] B. Hammouda, (2016). Chapter 13 - Neutron Area Detectors. Available: NIST Center for Neutron Research https://www.ncnr.nist.gov/staff/hammouda/distance_learning/chapter_13.pdf. Last accessed 23/11/20.

[2] S. Jaksch *et al.*, (2018). Recent Developments SoNDe High-Flux Detector Project. Proceedings of the International Conference on Neutron Optics (NOP2017).

[3] J. Allison *et al.*,(2016) Nucl. Instr. and Meth. A 835. 186-225, and references therein

[4] European Commission Website, (2020). European Research Infrastructure Consortium (ERIC). Available: https://ec.europa.eu/info/research-and-innovation/strategy/european-research-infrastructures/eric_en. Last accessed 30/11/20.

[5] ESS, (2020). European Spallation Source. Available: https://europeanspallationsource.se/about. Last accessed 30/11/20.

[6] ESS, (2015). CNRS and ESS Advance a New Standard for Linac Design. Available: https://europeanspallationsource.se/article/cnrs-and-ess-work-together-develop-new-linac-technology. Last accessed 30/11/20.

[7] ESS, (2017). How it works. Available: https://europeanspallationsource.se/accelerator/how-it-works. Last accessed 30/11/20.

[8] M. Eshraqi *et al.*, (2014) The ESS Linac. *Proc. 5th Int. Particle Accelerator Conf. (IPAC'14)*. 3320-3322,

[9] R. Pynn, (2018) Lecture 2: Neutron Scattering Instrumentation and Facilities. Available: NIST Center for Neutron Research. Last accessed 30/11/20. https://www.nist.gov/ncnr/2018-summer-school-fundamentals-neutron-scattering/course-materials

[10] G. S. Bauer, (1998). Physics and Technology of Spallation Neutron Sources. Available: U.S. Department of Energy Office of Scientific and Technical Information. Last accessed 30/11/20. https://www.osti.gov/etdeweb/servlets/purl/20020531

[11] H. Jacobsen *et al.*, (2013). Bi-spectral extraction through elliptic neutron guides. *Nuclear Instruments and Methods in Physics Research Section A: Accelerators, Spectrometers, Detectors and Associated Equipment.* 717, 69-76.

[12] K. H. Andersen *et al.*, (2020). The instrument suite of the European Spallation Source. *Nuclear Instruments and Methods in Physics Research Section A: Accelerators, Spectrometers, Detectors and Associated Equipment.* 957 (163402).

[13] G. S. Bauer, (2010). Overview on spallation target design concepts and related materials issues. *Journal of Nuclear Materials*. 398 (1-3), 19-27

[14] S. A. H. Feghhi *et al.*, (2014). Investigation of the optimal material type and dimension for spallation targets using simulation methods. *Journal of Theoretical and Applied Physics*. 8 (117).

[15] R. Pynn, (2009). Neutron Scattering - A Non-destructive Microscope for Seeing Inside Matter. In: L. Liyuan, R. Rinaldi, H Schober *Neutron Applications in Earth, Energy and Environmental Sciences.* New York: Springer US. 15-36.

[16] I. S. Anderson *et al.*, (2009). Preface. In: I. S. Anderson, R. L. McGreevy, H. Z. Bilheux *Neutron Imaging and Applications: A Reference for the Imaging Community.* New York: Springer US. vii.

[17] M. Strobl, (2016). *What is Neutron Imaging?*. Available: https://www.psi.ch/de/niag/what-is-neutron-imaging. Last accessed 30/11/20.

[18] K. Sköld and D. L. Price, (1986). *Neutron Scattering*. Academic Press. 1-555

[19] M. N. H. Comsan, (2011). Spallation Neutron Sources For Science and Technology. *Proceedings of the eighth Nuclear and Particle Physics Conference (NUPPAC-2011)*. 287.

[20] V. K. Aswal and P. S. Goyal, (2000). Small-angle neutron scattering diffractometer at Dhruva reactor. *Current Science*. 79 (7), 947-953.

[21] V. K. Aswal *et al.*, (2000). Double monochromator with three pairs of crystals for a SANS machine: Monte Carlo simulation studies. *Journal of Applied Crystallography*. 33 (1), 118-125.

[22] S. Jaksch, (2016). Considerations about chopper configuration at a time-of-flight SANS instrument at a spallation source. Nuclear Instruments and Methods in Physics Research Section A: Accelerators, Spectrometers, Detectors and Associated Equipment. 835, 61-65

[23] S. Jaksch, (2020). *SKADI General Purpose SANS*. Available: https://europeanspallation source.se/instruments/skadi#science-case. Last accessed 30/11/20.

[24] S. Jaksch *et al.*, (2014). Concept for a time-of-flight Small Angle Neutron Scattering instrument at the European Spallation Source. *Nuclear Instruments and Methods in Physics Research Section A: Accelerators, Spectrometers, Detectors and Associated Equipment*. 762, 22-30.

[25] C. Carlile *et al.*, (2013). European Spallation Source Technical Design Report. (10.13140/RG.2.1.2040.6483/1).

[26] S. Jaksch, (2020). *SKADI General Purpose SANS*. Available: https://europeanspallation source. se/instruments/skadi#instrument-description

[27] Camelin Intelligent Technologies. (2021). *Helium-3 Filled Proportional Counter*. Available: http://camelin.tech/en/helium-3-filled-proportional-counter/. Last accessed 7/1/21.

[28] W. R. Leo, (1987). In: *Techniques for Nuclear and Particle Physics Experiments*. Berlin and Heidlberg: Springer Verlag.

[29] R. G. Fronk, S. L. Bellinger, L. C. Henson *et al.*, (2015). Dual-sided microstructured semiconductor neutron detectors (DSMSNDs). *Nuclear Instruments and Methods in Physics Research, Section A: Accelerators, Spectrometers, Detectors and Associated Equipment*. 804, 201-206.

[30] K. Saito *et al.*, (2007). Study of scintillation in helium mixed with xenon to develop thermal neutron detectors, *Nuclear Instruments and Methods in Physics Research Section A: Accelerators, Spectrometers, Detectors and Associated Equipment*, 581, (1-2), 119-122

[31] United States Department of Energy, (1999). In: Tennessee Valley Authority *Final environmental impact statement The Production of Tritium in a Commercial Light Water Reactor (TN, AL): Environmental Impact Statement, Volume 1.* Washington DC: United States Department of Energy.

[32] A. Glavic, (2020). ESTIA Focusing Reflectometer. Available: https://europeanspallation source.se/instruments/estia. Last accessed 30/11/20.

[33] G. Mauri *et al.*, (2018) Neutron reflectometry with the Multi-Blade 10B-based detector *Proceedings of the Royal Society A*. 474. (2216)

[34] F. Piscitelli *et al.*, (2017). The Multi-Blade Boron-10-based neutron detector for high intensity neutron reflectometry at ESS. *Journal of Instrumentation*, 12, (3), 3013

[35] P. P. Deen, (2020). CSPEC Cold Chopper Spectrometer. Available: https://european spallationsource.se/instruments/cspec. Last accessed 30/11/20.

[36] N. Violini, (2020). T-REX Bispectral Chopper Spectrometer. Available: https://european spallationsource.se/instruments/t-rex. Last accessed 30/11/20.

[37] P. P. Deen, (2014). ESS Instrument Construction Proposal VOR : Versatile, Optimal Resolution Chopper Spectrometer. Available: https://ess-public-legacy.esss.se/sites/default /files/vor_2014_march.pdf

[38] M. Anastasopoulos *et al.*, (2017). Multi-Grid Detector for Neutron Spectroscopy: Results Obtained on Time-of-Flight Spectrometer CNCS. *Journal of Instrumentation*. 12, (4).

[39] D. S. McGregor *et al.*, (2003). Design considerations for thin film coated semiconductor thermal neutron detectors-I: basics regarding alpha particle emitting neutron reactive films. *Nuclear Instruments and Methods in Physics Research Section A: Accelerators, Spectrometers, Detectors and Associated Equipment*. 500 (1-3), 272-308.

[40] C. Grupen, I. Buva, (2012) . In: *Handbook of Particle Detection and Imaging* . Berlin, New York: Springer.

[41] A. M. Okowita, (2014). Characterization of Lithium-6 as a Commercial Helium-3 Alternative for Nuclear Safeguards and Security. *University of Tennessee, Knoxville TRACE: Tennessee Research and Creative TRACE: Tennessee Research and Creative Exchange Exchange Masters Theses Graduate School*.

[42] P. Rinard. *Neutron Interactions with Matter*. Available: https://www.lanl.gov/org/ddste/ aldgs/sst-training/_assets/docs/PANDA/Neutron%20Interactions%20with%20Matter%20 Ch.%2012%20p.%20357-378.pdf. Last accessed 30/11/20.

[43] G. Leinweber *et al.*, (2006). Neutron Capture and Total Cross-Section Measurements and Resonance Parameters of Gadolinium. *Nuclear Science and Engineering*. 154 (3), 261-279.

[44] J. K. Shultis, D.S. McGregor, (2008). Designs for micro-structured semiconductor neutron detectors. *Hard X-Ray, Gamma-Ray, and Neutron Detector Physics X*. 7079, 41-55.

[45] D. S. McGregor, S.L. Bellinger, J.K. Shultis, (2012). Present status of microstructured semiconductor neutron detectors. *Journal of Crystal Growth*. 379. 99âĂŞ11.

[46] S. L. Bellinger, R.G. Fronk, W.J. McNeil, T.J. Sobering, D.S. McGregor, (2011). Improved high efficiency stacked microstructured neutron detectors backfilled with nanoparticle 6LiF. *IEEE Trans. Nucl. Sci.* 59. 167-173.

[47] R. G. Fronk, S. L. Bellinger, L. C. Henson, D. E. Huddleston, T. R. Ochs, T. J. Sobering, and D. S. McGregor, (2015) High-efficiency microstructured semiconductor neutron detectors for direct He-3 Replacement, *Nucl. Inst. Meth. Phys. Res.* A, 779, 25-32.

[48] S. Bellinger, (2013). *Microstructured Semiconductor Neutron Detector Arrays for Neutron Scattering Measurements*. Available: https://www.sbir.gov/sbirsearch/detail/407707. Last accessed 30/11/20.

[49] R. G. Fronk, S. L. Bellinger, L. C. Henson, T. R. Ochs, C. T. Smith, J. K. Shultis, and D. S. McGregor, (2015) Dual-sided microstructured semiconductor neutron detectors (DSM-SNDs), *Nucl. Inst. Meth. Phys. Res.* A, 804. 201-206.

[50] R. C. Fernow, (1986). In: *Introduction to experimental particle physics.* Cambridge Univ. Press.

[51] A. N. Mabe *et al.*, (2016). Transparent plastic scintillators for neutron detection based on lithium salicylate. *Nuclear Instruments and Methods in Physics Research Section A: Accelerators, Spectrometers, Detectors and Associated Equipment*. 806, 80-86.

[52] G. Ranucci *et al.*, (1994). Scintillation decay time and pulse shape discrimination of binary organic liquid scintillators for the Borexino detector. *Nuclear Instruments and Methods in Physics Research Section A: Accelerators, Spectrometers, Detectors and Associated Equipment*. 350 (1-2), 338-350.

[53] C. Buck *et al.*, (2019). Production and Properties of the Liquid Scintillators used in the Stereo Reactor Neutrino Experiment. *Journal of Instrumentation*. 14.

[54] Reprinted with permission from: N. Zaitseva *et al.*, (2009). Growth and Properties of Lithium Salicylate Single Crystals. *Crystal Growth & design*. 9, (8), 3799-3802. Copyright 2009 American Chemical Society

[55] Saint Gobain, (2018). *Solid Plastic and Liquid Scintillation Materials*. Available: https://www.crystals.saint-gobain.com/products/organic-scintillation-materials. Last accessed 30/11/20.

[56] J. Cerny, Z. Dolezal, M. P. Ivanov *et al.*, (2004). Study of neutron response and n-γ discrimination by charge comparison method for small liquid scintillation detector *Nucl. Instrum. Meth.* A. 527. 512

[57] S. Ait-Boubker *et al.*, (1989). Thermal neutron detection and identification in a large volume with a new lithium-6 loaded liquid scintillator. Nuclear Instruments and Methods in Physics Research Section A: Accelerators, Spectrometers, Detectors and Associated Equipment. 277 (2-3), 461-466.

[58] L. Swiderski *et al*, (2010). Further Study of Boron-10 Loaded Liquid Scintillators for Detection of Fast and Thermal Neutrons. Nuclear Science, IEEE Transactions. 57, 375-380.

[59] C. W. E. van Eijk, (2004) Inorganic scintillators for thermal neutron detection, *Radiation Measurements*, 38,337-342.

[60] Saint-Gobain, (2019). *NaI(Tl+Li)Neutron-Gamma Scintillator*. Available: https:// www.crystals.saint-gobain.com/sites/imdf.crystals.com/files/documents/nail-material-data-sheet.pdf. Last accessed 30/11/20.

[61] G. F. Knoll, (1979). In: Radiation Detection and Measurement. New York: John Wiley & Sons.

[62] P. R. Menge *et al*, (2018). Large Format Li Co-Doped NaI:Tl (NaIL^{TM}) Scintillation Detector for Gamma-Ray and Neutron Dual Detection. *Pacific Rim Conference on Ceramic and Glass Technology: Ceramic Transactions*. 264 (20).

[63] Saint-Gobain, (2019). *NaIL^{TM} Dual Detection Neutron-Gamma Scintillator*. Available: https://www.crystals.saint-gobain.com/products/ nai-sodium-iodide-tl-lithium. Last accessed 30/11/20.

[64] T. Nakamura *et al.*, (2009). Evaluation of the performance of a fibre-coded neutron detector with a ZnS/10B2O3 ceramic scintillator. *Nuclear Instruments and Methods in Physics Research Section A: Accelerators, Spectrometers, Detectors and Associated Equipment*. 600 (1), 164-166.

[65] Y. Wang *et al.*, (2013). New type of neutron image scintillator based on (H3BO3)-B-10/ZnS(Ag). *International Topical Meeting on Neutron Radiography*. 43, 216-222.

[66] C. M Whitney *et al.*, (2015). GammaâĂŞneutron imaging system utilizing pulse shape discrimination with CLYC. *Nuclear Instruments and Methods in Physics Research Section A: Accelerators, Spectrometers, Detectors and Associated Equipment*. 784, 346-351.

[67] F. P. Doty *et al.*, (2012). Elpasolite Scintillators. *Sandia Report, SAND2012-9951*. Access: https://prod-ng.sandia.gov/techlib-noauth/access-control.cgi/2012/129951.pdf

[68] R. S. Woolf *et al.*, (2016). Characterization of the internal background for thermal and fast neutron detection with CLLB. Nuclear Instruments and Methods in Physics Research Section A: Accelerators, Spectrometers, Detectors and Associated Equipment. 838, 147-153.

[69] G. Manzin *et al.*, (2004). A gas proportional scintillator counter for thermal neutrons instrumentation. *Nuclear Instruments and Methods in Physics Research Section A: Accelerators, Spectrometers, Detectors and Associated Equipment*. 535 (1-2), 102-107.

[70] A. Morozov *et al.*, (2012). A 2D gas scintillation detector for thermal neutrons. *IEEE Nuclear Science Symposium and Medical Imaging Conference Record (NSS/MIC)*. 1572-1576.

[71] L. M. Bollinger, G.E. Thomas, R.J. Ginther, (1962). Neutron detection with glass scintillators. Nuclear Instruments and Methods . 17 (1), 97-116.

[72] Scintacor, (2020). *6-lithium glass scintillators for neutron detection*. Available: https://scintacor.com/products/6-lithium-glass/. Last accessed 25/03/20.

[73] S. Guizhen *et al.*, (1986). The preparation and properties of cerium-activated lithium glass scintillators. *Journal of Non-Crystalline Solids*. 80 (1-3), 594-599.

[74] First Sensor. (2015). Introduction to silicon photomultipliers (SiPMs). 1-6. Available: http://www.first-sensor.com/cms/upload/appnotes/AN_SiPM_Introduction_E.pdf

[75] D. Renker, (2006). Geiger-mode avalanche photodiodes, history, properties and problems. *Nuclear Instruments and Methods in Physics Research Section A: Accelerators, Spectrometers, Detectors and Associated Equipment*. 567 (1), 48-56.

[76] A. Stoykov *et al.*, (2015) *Nuclear Instruments and Methods in Physics Research Section A: Accelerators, Spectrometers, Detectors and Associated Equipment.* A787. 361-366

[77] P. Eckert *et al.*, (2010). Characterisation studies of silicon photomultipliers, *Nuclear Instruments and Methods in Physics Research Section A: Accelerators, Spectrometers, Detectors and Associated Equipment*. 620 (2-3), 217-226.

[78] Hamamatsu Photonics K. K. Editorial Committee, (2007). *Photomultiplier Tubes: Basics and Applications*. 3rd ed. Hamamatsu, Japan: Hamamatsu Photonics K. K. Electron Tube Division. 1-305.

[79] Hamamatsu, (2020). *Microchannel Plate Photomultiplier Tube R10754-07-M16*. Available: https://www.hamamatsu.com/resources/pdf/etd/R10754-07-M16_TPMH1364E.pdf. Last accessed 1/12/20.

[80] K. Matsuoka *et al.*, (2016). *Extension of the MCP-PMT lifetime*. Available: https://indico.cern.ch/event/393078/contributions/2195231/attachments/1332045/2002282/RICH2016_matsuoka.pdf. Last accessed 1/12/20.

[81] D. A. Orlov *et al.*, (2019). High-detection efficiency MCP-PMTs with single photon counting capability for LIDAR applications. In: Zoran Sodnik and Nikos Karafolas and Bruno Cugny *International Conference on Space Optics - ICSO 2018*. USA : SPIE. 1148-1155.

[82] Hamamatsu, (2020). *Microchannel plate photomultiplier tube R10754-07-M16*. Available: https://www.hamamatsu.com/resources/pdf/etd/R10754_TPMH1364E.pdf. Last accessed 21/1/21.

[83] Hamamatsu, (2019). *Flat Panel Type Multianode PMT Assembly H12700 Series / H14220 Series*. Available: https://www.hamamatsu.com/resources/pdf/etd/H12700_H14220_TPMH1379E.pdf. Last accessed 1/12/20.

[84] H. O. Anger, (1958). Scintillation Camera. *Review of Scientific Instruments*. 29 (1), 27-33.

[85] R. A. Riedel, C. Donahue, T. Visscher, C. Montcalm, (2015). Design and performance of a large area neutron sensitive anger camera. *Nuclear Instruments and Methods in Physics Research Section A: Accelerators, Spectrometers, Detectors and Associated Equipment*. 794, 224-233.

[86] K. Kanaki *et al.*, (2018). Detector rates for the Small Angle Neutron Scattering Instruments at the European Spallation Source. *Journal of Instrumentation*. 13 (7), 7016.

[87] IDEAS Integrated Detector Electronics AS. (2020). *ROSMAP-MP*. Available: https://ideas.no/products/rosmap-mp/. Last accessed 25/03/20.

[88] M. J. Christensen *et al.*, (2018). Software-based data acquisition and processing for neutron detectors at European Spallation Source - Early experience from four detector designs. *Journal of Instrumentation*. 13 (11), T11002.

[89] J. R. M. Annand, (2007). *Data Analysis within an AcquRoot Framework*. Available: http://www.nuclear.gla.ac.uk/∼acqusys/doc/AcquRoot.08.07.pdf. Last accessed 1/12/20.

[90] K. H. Berkurts, K. Wirtz, (1964). *Neutron Physics*. Berlin and Heidlberg GmbH: Springer-Verlag. Appendix I.

[91] G. Ban, G. Bison, K. Bodek *et al.*, (2016). Ultracold neutron detection with 6Li-doped glass scintillators. *Eur. Phys. J.* A 52, 326.

[92] Saint-Gobain Ceramics & Plastics, Inc.. (2020). *Lithium Glass Scintillators*. Available: https://www.crystals.saint-gobain.com/products/lithium-glass-scintillators. Last accessed 9/12/20.

[93] J. Choe. jusong.choe@ideas.no. IDEAS, private communication 2020.

[94] INMOS, (1985). *VMEbus Specification Manual*. Available: http://www.transputer.net/mtw/imsb016/doc/vme/vmebus.pdf. Last accessed 1/12/20.

[95] R. Brun and F. Rademakers, (1997). ROOT - An Object Oriented Data Analysis Framework. *Proceedings AIHENP'96 Workshop, Lausanne, Sep. 1996, Nucl. Inst. & Meth. in Phys. Res*. A 389, 81-86.

[96] Go Photonics. (2017). *PiL040X*. Available: https://www.gophotonics.com/products/lasers/advanced-laser-diode-systems-gmbh/29-283-pil040x. Last accessed 24/03/20.

[97] B. Khoury. boris.khoury@alsgmbh.de. Manual for laser controller EIG2000DX. 11/03/2019.

[98] Hamamatsu. (2005). *Board-Level Camera for OEM SolutionC9260-901, -902, -904, -905*. Available: http://www.alacron.com/clientuploads/directory/Cameras/HAMAMATSU/c9260-901-Datasheet.pdf. Last accessed 1/12/20.

[99] R. Jebali Ramsey.AlJebali@ess.eu. 60 PE level justification, private communication 2020.

[100] E. H. Bellamy *et al.*, (1994). Absolute calibration and monitoring of spectrometric channel using a photomultiplier. *Nuclear Instruments and Methods*. A 339. 468

[101] M. Mirazita, (2011). Test of the CLAS12 RICH detector. Talk presented at CLAS Collaboration meeting, Jefferson Lab.

[102] Burle Technologies Inc.. (2003). *8854 Photomultiplier 129-mm (5-inch) Diameter, 14-stage QUANTACON^{TM} Type Having a Bialkali Photocathode and High-Gain Gallium-Phosphide Dynodes*. Available: https://hallcweb.jlab.org/DocDB/0009/000965/001/Burle_8854_PMT_specs.pdf. Last accessed 7/12/20.

[103] R. Perrino *et al.*, (2001). Performances of the aerogel threshold Čerenkov counter for the Jefferson Lab Hall A spectrometers in the 1 - 4 GeV/c momentum range. *Nuclear Instruments and Methods in Physics Research* A , 457, 571-580.

[104] R. Montgomery, (2013). *A position sensitive photon detector for the CLAS12 ring imaging Čerenkov application*. PhD thesis, University of Glasgow, Glasgow.

[105] M. Calvi *et al.*, (2015). Characterization of the Hamamatsu H12700A-03 and R12699-03 multi-anode photomultiplier tubes. *Journal of Instrumentation*. 10 (9), 9021.

[106] M. P. Hehlen *et al.*, (2018). Light propagation in a neutron detector based on 6Li glass scintillator particles in an organic matrix. *Journal of Applied Physics*. 124 124502.

[107] M. Contalbrigo *et al.*, (2014). The large-area hybrid-optics CLAS12 RICH detector: Tests of innovative components. *Nuclear Instruments and Methods in Physics Research Section A: Accelerators, Spectrometers, Detectors and Associated Equipment*. 766, 22-27

[108] E. Rofors *et al.*, (2019). Response of a Li-glass/multi-anode photomultiplier detector to α-particles from ^{241}Am. *Nucl. Instr. and Meth*. A. 929, 90-96.

[109] E. Rofors *et al.*, (2020). Response of a Li-glass/multi-anode photomultiplier detector to focused proton and deuteron beams. *Nucl. Instr. and Meth.* A. 984, 164604.

[110] L. Boyd *et al.*, (2021). Simulation of the Response of the Solid State Neutron Detector for the European Spallation Source. *Nucl. Instr. and Meth.* A. 998, 165174.

[111] Eljen Technology, (2016). *Silicone Rubber Optical Interface EJ-560*. Available: https://eljentechnology.com/products/accessories/ej-560. Last accessed 1/12/20.

[112] Eljen Technology, (2016). *Optical Cement EJ-500*. Available: https://eljentechnology .com/products/accessories/ej-500. Last accessed 1/12/20.

[113] Eljen Technology, (2016). *Reflective Paint EJ-510, EJ-520*. Available: https://eljen technology.com/products/accessories/ej-510-ej-520. Last accessed 1/12/20.

[114] Laser Beam Products, (2014). *Laser Beam Products - Precision Optics - Mirrors for Lasers, Science, Industry*. Available: https://laserbeamproducts.wordpress.com/2014/ 06/19/reflectivity-of-aluminium-uv-visible-and-infrared/. Last accessed 1/12/20.

[115] G. Hass and J. Waylonis, (1961). Optical Constants and Reflectance and Transmittance of Evaporated Aluminum in the Visible and Ultraviolet. *J. Opt. Soc. Am.* 51, 719-722.

[116] C. Ayieko *et al*., (2015). Controlled Texturing of Aluminum Sheet for Solar Energy Applications. *Advances in Materials Physics and Chemistry*. 05. 458-466.

[117] P. Gumplinger, (2002). *Optical Photon Processes in GEANT4*. Available: https://geant4.web.cern.ch/sites/geant4.web.cern.ch/files/geant4/collaboration/workshops/ users2002/talks/lectures/OpticalPhoton.pdf. Last accessed 1/12/20.

[118] J. B. Birks, (1964). *The Theory and Practice of Scintillation Counting*. Oxford U.K.: Pergamon Press.

[119] V. I. Tretyak, (2010). Semi-empirical calculation of quenching factors for ions in scintillators. *Astroparticle Physics*. 33 (1) 40-53.

[120] M. F. L'Annunziata. (2016). Chapter 4 - Alpha Radiation. In: Michael F. L'Annunziata Radioactivity . 2nd ed. Amsterdam: Elsevier. 123-134.

[121] Geant4 Collaboration, (2019). *A Simulation Toolkit, Physics Reference Manual, Release 10.6*. 4th Revision.

[122] M. J. Berger *et al.*, (2016) Report 49. *Journal of the International Commission on Radiation Units and Measurements*. os25(2):

[123] J. W. Poston. (2003). Dosimetry. In: R.A. Meyers *Encyclopedia of Physical Science and Technology*. Cambridge, Mass: Academic Press. 603-650

[124] University of Cambridge. (2020). *Cross-Sections*. Available: https://www.doitpoms.ac.uk/tlplib/nuclear_materials/cross_section.php. Last accessed 1/12/20.

[125] V. D. Rusov *et al.*, (2016). Neutron Moderation Theory Taking into Account the Thermal Motion of Moderating Medium Nuclei. arXiv:1612.06838v1

[126] J. E. Strain, G. W. Leddicotte, (1962). The preparation, properties , and uses of Americium-241, Alpha, Gamma, and Neutron Sources. United States. https://www.osti.gov/servlets/purl/4777909

[127] Exactly $(1.143 \pm 0.015) \times 10^6$ neutrons per second. Testing certified at National Physical Laboratory, Teddington, Middlesex, UK TW11 0LW on 24 July 2015.

[128] J. Scherzinger *et al.*, (2017). A comparison of untagged gamma-ray and tagged-neutron yields from 241AmBe and 238PuBe sources. *Applied Radiation and Isotopes*. 127, 98-102.

[129] K. S. Krane (1987). *Introductory Nuclear Physics*. 3rd ed. USA: John Wiley & Sons. .K. S Krane, Introductory Nuclear Physics

[130] Nuclear Data. (1998). Table of Radioactive Isotopes. Available: http://nucleardata.nuclear.lu.se/toi/nuclide.asp?iZA=950241. Last accessed 1/12/20.

[131] E. Rofors *et al.*, (2021). Response of a Li-glass/multi-anode photomultiplier detector to collimated thermal-neutron beams.*Nucl. Instr. and Meth.* A. 165170.

[132] H. Kluge, (1998). Irradiation facility with radioactive reference neutron sources: basic principles (PTB-N–34). Germany

[133] Francesco Messi Cerberus Board. Email: francesco.messi@nuclear.lu.se

[134] Y. Oshima *et al.*, (2011). Temperature Dependence of Li-Glass Scintillator Response to Neutrons, *Nuclear Science and Technology*. 1, 296-299.

[135] P. Bentley, A. Hamer, (1958). Boron-10 Abundance in Nature. *Nature*. 182, 1156.

[136] Hooker Electrochemical Company. (1957). *Boron and its Isotopes*. Available: https://www.osti.gov/biblio/4364833/. Last accessed 1/12/20.

[137] A. Valda *et al.*, (2005). Development of a tomographic system for online dose measurements in BNCT (Boron Neutron Capture Therapy). *Brazilian Journal of Physics*. 35 (3b).

[138] D. R. McAlister, (2018). *Gamma Ray Attenuation Properties of Common Shielding Materials*. PhD Thesis. University Lane Lisle, Chicago.

[139] National Electrostatics Corps.. (2020). *Pelletron Charging System*. Available: https://www.pelletron.com/products/pelletron-charging-chains/. Last accessed 1/12/20.

[140] R. J. W. Frost *et al.* (2020). Internal report, Division of Nuclear Physics, Lund University, 12th Oct. 2020 (unpublished).

[141] P. Kristiansson. (2018). *Lund Ion Beam Analysis Facility (LIBAF)*. Available: http://www.nuclear.lu.se/forskning/tillaempad-kaernfysik/libaf/. Last accessed 1/12/20.

[142] P. Kristiansson. (2017). *Technique*. Available: http://www.nuclear.lu.se/english/research/applied-nuclear-physics/libaf/tekniken/. Last accessed 1/12/20.

[143] Silson. *Ultra Thin Membranes*. Available: https://www.silson.com/. Last accessed 1/12/20.